

Imperial College
London

Imperial College London
Department of Materials

Hybrid Materials for Meniscus Replacement in the Knee

Yu Chien Lin



Submitted for the degree of Doctor of Philosophy

Abstract

The meniscus is cartilage that not only prevents the bones in knee joints to grind together but acts as a joint stabiliser. Many athletes and older people suffer from meniscus tears and degeneration. Meniscal tear treatments have been through meniscal suture or by partial meniscectomy (removal). These treatments may cause changes in loading or decreased contact area and increased contact stress. Consequently, the ultimate result is a total meniscectomy that potentially leads to osteoarthritis (OA). These current surgical strategies have lower success rates in younger patients. There are no successful artificial meniscus replacement devices for young patients, therefore, new materials for meniscus replacement are required. Here, the aim was to develop a novel biomimetic meniscus device made of a silica/polytetrahydrofuran ($\text{SiO}_2/\text{polyTHF}$) inorganic/organic hybrid material. The device is biomimetic in terms of its structural design, mechanical properties, and integration with the host tissue. The device should delay onset of OA. The hybrid has unique properties in that is a bouncy material which has comparable mechanical properties to knee cartilage. Two pot hybrid synthesis was used to synthesise the $\text{SiO}_2/\text{polyTHF}$ hybrid and casting mould was developed based on the shrinkage factor of the hybrid. The hybrid synthesis modifications were conducted by controlling compositions and drying processes. Biological fixation of the hybrid meniscus was achieved by titanium anchors with gyroid porous architecture which can provide initial mechanical fixation and secondary biological fixation on the tibia. The architecture was designed using Solidworks and Rhinoceros software and printed by the Additive Manufacturing technique of selective laser melting (SLM). Mechanical testing of the device included compression, cyclic loading, shear strength and long-term 90 days *in-vitro* mechanical testing, tribology against living bovine

cartilage, and cell studies. The results suggest that combination of hybrid and Ti gyroid has potential to be meniscus implant due to comparable mechanical properties, low friction coefficient, and non-cytotoxicity.

Declarations

Declaration of originality

I hereby certify that the work presented in this thesis is the result of my own investigations, which were carried out at Imperial College London from November 2018 to November 2021, except where otherwise stated. Other contributions have been truly and properly acknowledged.

Copyright declaration

The copyright of this thesis rests with the author and is made available under a Creative Commons Attribution Non-Commercial No Derivatives licence. Researchers are free to copy, distribute or transmit the thesis on the condition that they attribute it, that they do not use it for commercial purposes and that they do not alter, transform or build upon it. For any reuse or redistribution, Researchers must make clear to others the licence terms of this work.

Yu Chien Lin

November 2021

Acknowledgements

First of all, I would like to thank my parents Mr. Ming-Kun, Lin (林明坤) and Ms. Li-Hong, Lin-Song (林宋麗紅) and family Jun-Ze (君澤), Yu-Chen (妤蓁), Yu-Jhe (宇哲), and Ling-Ling (玲玲). Without your support, I cannot award this degree.

Special thank you for my brilliant supervisor, Professor Julian R. Jones, for your careful and patient guidance so that I can successfully complete my Ph.D. degree and my co-supervisor Professor Jonathan Jeffers for giving me lots of important advice and help in experimental design.

Thank you for Dr. Stefano Angioletti-Uberti and Dr. Richard Jan van Arkel as my Ph.D. early-stage and late-stage examiners. Their input was invaluable.

Thank you to those listed here (all in Materials, unless stated) for their important help in experimental work: Dr. Francesca Tallia and Dr. Gloria Young for hybrid synthesis training and supervision; Haffsah Iqbal assisted for NMR testing; Dr. Jeff Clark worked together for DIC work; Dr. Siwei Li and Fadi Barrak worked together cell studies; Achintha Kondarage and Sharad Patel (Mechanical Engineering) assisted and trained for μ CT imaging; Dr. Reece N. Oosterbeek (Mechanical Engineering) did SLM gyroid scaffold manufacturing; Dr. Nupur Kohli (Mechanical Engineering) did bovine knee cartilage dissection; Dr. Marc Masen (Mechanical Engineering) for supervising the tribology tests; Dr. Mahmoud Ardakani for SEM training; Mr. Ben Chan for ICP training; Mr. Pawel Orzlowski, Murali Manoj, and Russell Stracey for emould preparation and Professor Ren-Jei Chung (Taipei Tech, Taiwan) for invaluable advice.

Thank you to everyone in JRJ group. Francesca, Gloria, Jeff, ZhenLun, Tian, Xiaomeng, Taneisha, Haffsah, XingChen, Agathe, Achintha, Siwei, Fadi, Alessandra, YuLin (William), DeYuan (Robin), ZhiJun, Xiuyuan, JingHan, Susiana, Anna, XinYu, BoWen, TianYuan, ZongHua, Meryem, Aryan, and JaeJun for all happy memories, supports, friendships.

Thanks to everyone who helped me especially Mrs. Darakshan Khan and Manjula Dilkushi Silva and people who I don't know but maintain our environment and equipment. I am sincerely grateful.

Yu Chien

November 2021

Table of Contents

Abstract.....	1
Table of Contents	6
List of Figures & Tables	10
List of Abbreviations.....	18
1. Aims.....	22
1.1. Motivation.....	22
1.2 Hypothesis	22
1.3 Fixation innovation.....	23
1.4 Aim of this project	24
2. Literature review.....	27
2.1 Meniscus.....	27
2.1.1 Introduction.....	27
2.1.2 The properties and structure of human meniscus	28
2.2 Meniscus repair and replacement	34
2.2.1 Meniscus lesions	34
2.2.2 Meniscus repair and fixation.....	36
2.2.3 Current meniscus replacement options	38
2.3 Hybrid materials.....	39
2.3.1 Definition of hybrid materials	39
2.3.2 Classification of hybrid materials.....	40
2.3.3 SiO ₂ /polyTHF based hybrids	42
2.4 Chemistry/structure/property relationships of hybrids	44
2.4.1 Silica based hybrid applications	44
2.4.2 SiO ₂ /polyTHF/PCL hybrid application	45
2.4.3 Non-degradable SiO ₂ /polyTHF hybrids.....	47
2.5 Additive manufacturing	47
2.5.1 3D printing technique	47
2.5.2 Selective laser melting technique	48
2.6 Gyroid structure	50

2.6.1	<i>Introduction of gyroid structure</i>	50
2.6.2	<i>Application of gyroid structure</i>	52
2.7	<i>Summary and objectives</i>	56
3.	Characterisation techniques	58
3.1	<i>Composition characterisation</i>	58
3.1.1	<i>TGA/DSC</i>	58
3.1.2	<i>FTIR</i>	58
3.1.3	<i>Solution state NMR</i>	59
3.1.4	<i>Degradation test (PBS degradation study) and ICP studies</i>	59
3.2	<i>Mechanical property testing</i>	60
3.2.1	<i>Compression testing</i>	60
3.2.2	<i>Shear testing</i>	61
3.2.3	<i>Cyclic testing in dry and wet conditions</i>	62
3.2.4	<i>Digital image correlation (DIC)</i>	62
3.3	<i>Material observations</i>	63
3.3.1	<i>Scanning electron microscopy (SEM)</i>	63
3.3.2	<i>X-ray micro-computer tomography (μCT)</i>	64
3.4	<i>In-vitro testing</i>	64
3.4.1	<i>MTT assay for cytotoxicity</i>	64
3.4.2	<i>Cell attachment</i>	66
4.	Mould and gyroid design	68
4.1.	<i>Introduction of mould design</i>	68
4.1.1.	<i>Mould design and challenge</i>	68
4.2.	<i>Methods</i>	69
4.2.1.	<i>Hybrid synthesis</i>	69
4.2.2.	<i>Mould casting</i>	70
4.2.3.	<i>Compression testing</i>	71
4.2.4.	<i>Digital Image Correlation (DIC) measurement</i>	72
4.2.5.	<i>μCT and shrinkage measurement</i>	73
4.3.	<i>Results and discussion</i>	74

4.3.1.	<i>μCT and shrinkage characterisation</i>	74
4.3.2.	<i>Shrinkage factor of C-shaped meniscus hybrid</i>	77
4.3.3.	<i>Optimisation of meniscus mould</i>	78
4.3.4.	<i>Mechanical properties of hybrid meniscus</i>	81
4.3.5.	<i>Conclusions</i>	85
4.4.	<i>Introduction of gyroid scaffold design</i>	85
4.5.	<i>Methods</i>	86
4.5.1.	<i>Solidworks gyroid scaffold design</i>	86
4.5.2.	<i>Rhinoceros gyroid design</i>	87
4.6.	<i>Results and discussion</i>	90
4.1.1.	<i>Solidworks gyroid scaffold</i>	90
4.1.2.	<i>Rhinoceros gyroid scaffold</i>	91
4.1.3.	<i>Selective laser melting manufacturing</i>	91
4.7.	<i>Conclusions</i>	92
5.	A comprehensive study of hybrid material and optimisation	95
5.1.	<i>Introduction</i>	95
5.2.	<i>Materials and methods</i>	96
5.2.1.	<i>Materials</i>	96
5.2.2.	<i>Hybrid synthesis</i>	96
5.2.3.	<i>Solution state NMR</i>	98
5.2.4.	<i>μCT and shrinkage factor determination</i>	99
5.2.5.	<i>Characterisation techniques</i>	99
5.2.6.	<i>Dissolution study and ICP</i>	100
5.3.	<i>Results and discussion</i>	101
5.3.1.	<i>Systematic optimisation of hybrid synthesis</i>	101
5.3.2.	<i>Hybrid chemical and thermal analysis</i>	107
5.3.3.	<i>Hybrid characterisation</i>	109
5.3.4.	<i>Hybrid dissolution and long-term use study</i>	116
5.4.	<i>Conclusions</i>	123
6.	Hybrid and gyroid scaffold for meniscus replacement	125

6.1.	<i>Introduction</i>	125
6.2.	<i>Materials and Methods</i>	126
6.2.1.	<i>Fabrication of Ti gyroids</i>	126
6.2.2.	<i>Hybrid and gyroid scaffold preparation</i>	127
6.2.3.	<i>Micro computed tomography for inner gyroid scaffold measurement</i> 128	
6.2.4.	<i>Scanning electron microscopy (SEM)</i>	129
6.2.5.	<i>Mechanical properties</i>	130
6.2.6.	<i>Tribology test</i>	132
6.2.7.	<i>Cell studies</i>	135
6.3.	<i>Results and discussion</i>	136
6.3.1.	<i>The hybrid and gyroid scaffold optimisation</i>	136
6.3.2.	<i>μCT for hybrid and gyroid structure observation</i>	138
6.3.3.	<i>SEM for hybrid and gyroid scaffold interface observation</i>	141
6.3.4.	<i>Mechanical properties of hybrid and gyroid scaffold</i>	143
6.3.5.	<i>Tribology test of hybrid and gyroid scaffold against cartilage</i>	146
6.3.6.	<i>Surface morphologies and roughness of samples</i>	149
6.3.7.	<i>Cytotoxicity of hybrid and gyroid scaffold</i>	152
6.3.8.	<i>Cell attachment of hybrid and gyroid scaffold</i>	153
6.3.9.	<i>ALP activity of hybrid and gyroid scaffold</i>	155
6.4.	<i>Conclusions</i>	156
7.	<i>Thesis conclusions and future work</i>	159
7.1.	<i>Thesis conclusions</i>	159
7.2.	<i>Future work</i>	160
8.	<i>References</i>	162
S1.	<i>Appendix</i>	182

List of Figures & Tables

- Figure 1.1 An optical image of a cross section of a meniscus: (a) Zone 1 is fully vascularized; Zone 2 is at the border of the vascular area; and Zone 3 is within the avascular area of the meniscus, adapted from [10]; F: femur; T: tibia; PCP: perimeniscal capillary plexus. (b) 3D design of two biological anchors (grey) to fix the hybrid (brown) meniscus device to the tibia bone via the location of anterior and posterior horns.24
- Figure 2.1 (a) Anatomy of knee joint; (b) illustration of how the force is transduced throughout the knee meniscus. The meniscus will transduce compressive loads to circumferential tensile loads during movements. Adapted from [12].....28
- Figure 2.2 Schematic diagram of human meniscus showing regional variations in vascularization and cell populations of the meniscus. Left: the top view of meniscus which consists of three regions from outer to inner zone which are zone 1, zone 2, and zone 3. Right: Zone 1 is a vascularized section, zone 2 is in middle section which has more fibroblast-like in appearance, and zone 3 region is located in inner section which consists smaller and rounder chondrocyte like cells. Adapted from [12].....30
- Figure 2.3 Photograph of human knee dissection made in Prof Andrew Amis’ group. The lateral meniscus is attached on the tibia, whereas anterior and posterior ends attach on anterior and posterior intercondyloid fossae of the tibia. The peripheral area is attached by tibial collateral ligament.31
- Figure 2.4 Schematic diagram of internal structure of human meniscus. There are three layers of collagen fibres with certain patterns which are random orientation collagen on surface layer, lamellar orientation collagen in lamellar layer, and parallel oriented collagen fibre bundles in central main layer. Adapted from [26, 29].33
- Figure 2.5 Typical fibrillation of a degenerative meniscal lesion (a); complex tear combining flap and horizontal tear (b); MRI lateral view of longitudinal medial meniscus tear (red arrow) (c); final look after meniscectomy reducing the volume of meniscal tissue (d). adapted from [37].35
- Figure 2.6(A) Illustration of normal meniscus, and common types of meniscus tears: (B) radial tear, (C) longitudinal tear, (D) horizontal flap, (E) vertical flap, (F) bucket handle tear, (G) oblique/parrot beak lesion, (H) complex degenerative, (I) horizontal tear, (J) root tears. Adapted from [37].36
- Figure 2.7 Schematic diagrams of (a) surgical repair on a vertical longitudinal meniscal tear using an inside-out repair with knots tied over the capsule, (b) all-inside

anchor-based construct, (c) all-inside knot-tying technique, and (d) a horizontal cleavage meniscal tear using multiple all-inside circumferential compression sutures placed with a self-retrieving suture-passing device followed by arthroscopic knot tying. The images are adapted from [50] and the original images from Mayo Foundation for Medical Education and Research.....38

Figure 2.8 Schematic of the sol-gel process that includes the hydrolysis tetraalkyl orthosilicates and their subsequent condensation to produce 3D SiO₂ networks as gels. Adapted from [61].40

Figure 2.9 Schematic of the chemical structure of silica/polymer hybrid material. Adapted from [63].....42

Figure 2.10 The schematic diagram the CROP reaction of THF, using GPTMS as an initiator, adapted from [8].44

Figure 2.11 (a) Optical microscope images of SiO₂/polyTHF/PCL hybrids of the five hybrid compositions from Si0-CL530 to Si90-CL530 before creation of a defect (top) and after self-healing at RT (bottom). Images for Si0-CL530, Si60-CL530 and Si70-CL530 were taken after 5 s from defect creation; images for Si80-CL530 and Si90-CL530 (Si(wt%)-CL530 refers to TEOS (Si)/PCL-diCOOH (CL (Mn = 530 Da)), when 0% Si-100% CL is present (Si0-CL) and 60% Si-40% CL is present (Si60-CL)) were taken after 24 h from defect creation. Scale bar = 500 μm and (b–d) SEM images of a defect created on a Si0-CL sample. From b-d images show the bridging effect along the fractured surfaces during the self-healing process. The margins of the defects are visible in (b) and a magnification of the bridging is reported in (c); this behaviour was confirmed also on other areas of the sample (d). Scale bars: 50 μm in (b); 10 μm in (c and d) images adapted from [8].46

Figure 2.12 SLM process (a) is shown laser impinging on the centre powder bed where the power is melted together. The left powder bed (b) is supplying new powder and covered new layer of powder by a scraper coming from the left bed to the centre bed for next laser scanning.49

Figure 2.13 The gyroid structure designed by CAD software. (a) the unit surface of gyroid design, (b) the rendered gyroid unit surface, (c) assembly gyroid unit cell by patterning gyroid unit surface and stack with adjusting symmetry axis and (d) the gyroid unit cell. The infinite interconnected gyroid can be built by mirroring the gyroid unit cell in (d).52

Figure 3.1 Universal shear testing rig designed by Solidworks. (a) top component is designed as a one-sided cutting blade with 1 mm of blade width and (b) bottom component is designed suitable for 10-18mm diameter of cylinder sample and the screw size is M4*20mm. Both top and bottom components have pin hold for the

fixation on the machine. (c) is computer numerical control (CNC) manufactured universal shear testing rig.	61
Figure 4.1 The experimental flow chart of in situ cationic ring opening polymerisation (CROP) synthesised SiO ₂ /PolyTHF monolithic hybrid with different compositions and different drying processes.	70
Figure 4.2 The images of PTFE mould for meniscus casting are (a) bottom and (b) top sections. (c) The moulds parts are tightened by 3 G-clamps. (Diameter of mould is 9cm).....	71
Figure 4.3 The images of (a) side view of curved steel platen, (b) side view of platen with synthetic meniscus, and (c, d) top view of platen and sample. Courtesy of S.A. Naghavi thesis [107].	72
Figure 4.4 Schematic diagrams of compression rig setup (a) before applying force, (b) after applying force, and (c) side view with LED light for image quality improvement. Adapted from S.A. Naghavi unpublished research in our group [107].	73
Figure 4.5 Photograph of synthesised hybrid cylinders after drying.	75
Figure 4.6 μ CT scans that illustrate the shape of (a) 25OD, (b)25FD, (c) 50OD, (d) 50FD, (e)75OD, (f)75FD, (g) 100OD, and (h) 100FD.	77
Figure 4.7 A schematic diagram of meniscus showing dimensions measured A to E (a) top view and (b) side view.	78
Figure 4.8 The optimised meniscus mould design (a) top view and (b) side view (units in mm).....	79
Figure 4.9 (a) Two types of hybrid meniscus moulds, (b) hybrid meniscus cast using the left mould, and (c) is hybrid meniscus cast with an improved (right) mould.	80
Figure 4.10 Compression testing (a) photograph of the hybrid meniscus cast in the original mould after compression testing and (b) compression test graph; compression test on (c) photograph of the hybrid meniscus cast in the improved mould after compression testing and (d) the compression test graph.	82
Figure 4.11 DIC results were captured in optical photographs using a canon 750D camera with EF-S 60 mm macro lens and 34 mm extension tubes which demonstrate hybrid meniscus deformation by the time as shown in (a) 0s, (b) 10s, (c) 30s, (d) 40s, (e) 50s, and (f) 55s. (An ink pattern was drawn by hand on the surface of the hybrid using a blue marker to create a speckle pattern to emphasise the contrast between the surface and the pattern.)	83
Figure 4.12 Dynamic mechanical test results were analysed using digital image correlation (DIC) technique which demonstrate hybrid meniscus deformation by the time as shown (a) 0s, (b) 10s, (c) 20s, and (d) 30s.....	84

- Figure 4.13 Gyroid structure designed by Solidworks software: (a) a single unit of gyroid structure which is stacked by eight star repeating units by certain angle rotation joined at specific angles; (b) demonstrates different wall thickness which can be used for controlling density and pore size; (c) patterning gyroid to build up 3D scaffold, and (d) cylindrical gyroid.87
- Figure 4.14 Rhinoceros is a software to design gyroid which is based on mathematic function.89
- Figure 4.15 Optical images of Solidworks-designed gyroid stainless steel scaffold manufactured using SLM technique in different orientations.90
- Figure 4.16 Rhinoceros-designed gyroid scaffolds printed using SLM technique using titanium material which demonstrate a great structure integration without any visible mismatch at joints. (Size of scaffold is 16 mm)91
- Figure 4.17 The post-treatment of printed scaffolds (a) after SLM printing samples are covered by metal powder; (b) the metal powder was removed; (c) a wire electrical discharge machine, and (d) sample and sample stage fixed on the wire electrical discharge machine for cutting along the sample substrate.....92
- Figure 5.1 Solution ^1H NMR data of (a) mixing THF and GPTMS for 15 minutes without added $\text{BF}_3 \cdot \text{OEt}_2$ catalyst with the GPTMS chemical structure labelled the representative proton resonance sites to the NMR peaks (inset); (b) is the result of mixed THF and GPTMS after adding the $\text{BF}_3 \cdot \text{OEt}_2$ catalyst for 3 minutes and 45 seconds. The molecular weight calculations were calculated using integration of the area under the GPTMS characteristic peak at 0.58 ppm and PolyTHF characteristic peak at 1.54 ppm.....101
- Figure 5.2 Molecular weight determination of organic moiety by recording time points for adding $\text{BF}_3 \cdot \text{OEt}_2$ catalyst to initiate the in-situ CROP for (a) 0:00, (b) 2:20, (c) 2:45, (d) 3:10, (e) 3:30, (f) 3:45, and (g) 5:00 (minutes: seconds). The solution was too viscous to do the test after 5 minutes mixing. The Mw data against time points is shown in (h).104
- Figure 5.3 The polymer optimisation recorded for 16 batches of hybrid synthesis for different THF:GPTMS ratios, the two-pot mixing time point (mm:ss), and representative photographs of samples. The black circle represents homogeneous cylindrical shape hybrid; the black triangle irregular semi-cylindrical shape; and the black X represents formation of hollow cylinders which formed when no bubble formation occurred after added $\text{BF}_3 \cdot \text{OEt}_2$ catalyst in organic pot and mixed two-pot after 60 minutes. (Hybrid diameter is 1.2 cm and NA is not applicable).....106
- Figure 5.4 TGA analysis for quantitative analysis of the inorganic and organic compositions in SiO_2 -PolyTHF hybrids by comparing oven drying (OD) and

freeze drying (FD) samples. The samples named by the molecular ratio of THF:GPTMS (as 1) and the drying methods which are 25OD, 25FD, 50OD, 50FD, 75OD, 75FD, 100OD, and 100FD.	108
Figure 5.5 FTIR spectra of SiO ₂ -PolyTHF hybrids with different compositions and oven drying (OD) and freeze drying (FD) methods. The samples named by the molecular ratio of THF:GPTMS (as 1) and the drying methods which are 25OD, 25FD, 50OD, 50FD, 75OD, 75FD, 100OD, and 100FD.	109
Figure 5.6 Representative curves for stress-strain behaviour of the hybrid cylinders following; (a) oven drying (OD); (b) freeze drying (FD). The samples named by the molecular ratio of THF:GPTMS (as 1) and the drying methods which are 25OD, 25FD, 50OD, 50FD, 75OD, 75FD, 100OD, and 100FD.	110
Figure 5.7 (a) Stress and (b) strain at fracture for hybrids the same THF:GPTMS ratio but different drying methods. The samples named by the molecular ratio of THF:GPTMS (as 1) and the drying methods (Oven drying (OD) and freeze drying (FD)) which are 25OD, 25FD, 50OD, 50FD, 75OD, 75FD, 100OD, and 100FD.	111
Figure 5.8 SEM images of SiO ₂ -PolyTHF hybrid surface morphology: (a) 25OD, (b) is 25FD; (c) 50OD; (d) 50FD; (e) 75OD; (f) 75FD; (g) 100OD; (h) 100FD.	112
Figure 5.9 SEM images of SiO ₂ -PolyTHF hybrid fracture surface after compression test to failure: (a) 25OD; (b) 25FD; (c) 50OD; (d) 50FD; (e) 75OD; (f) 75FD; (g) 100OD; (h) 100FD.	114
Figure 5.10 (a) SEM image of the surface of 50OD sample and (b) EDS with spectrum 1 focused on the flat surface and the spectrum 2 focused on precipitation; (c) SEM image of 50FD sample and (d) EDS (d) analysis with spectra 1 and 4 focused on the flat surface and spectra 2 and 3 focused on the precipitations.	116
Figure 5.11 The degradation study recorded the weight loss before and after soaking SiO ₂ -PolyTHF hybrids in PBS in an incubating orbital shaker held at 37°C, agitated at 120 rpm for 1, 7, 14, 30, 60, and 90 days. The samples named by the molecular ratio of THF:GPTMS (as 1) and the drying methods (Oven drying (OD) and freeze drying (FD)) which are 25OD, 25FD, 50OD, 50FD, 75OD, 75FD, 100OD, and 100FD.	117
Figure 5.12 The dissolution study of SiO ₂ -PolyTHF hybrids soaked in PBS and placed in an incubating orbital shaker held at 37°C, agitated at 120 rpm for 1, 7, 14, 30, 90 and 90 days.	119
Figure 5.13 Cyclic compression testing of SiO ₂ -PolyTHF hybrids before and after soaking in PBS for 90 days: (a) 25OD, (b) 50OD, (c) 75OD, and (d) 100OD samples. Every 10 cycles of 10 ⁴ are shown. The samples named by the molecular ratio of THF:GPTMS (as 1) and the drying method (Oven drying (OD)) which	

are 25OD, 50OD, 75OD, and 100OD.....	121
Figure 5.14 Cyclic compression tests of SiO ₂ -PolyTHF hybrids before and after soaking in PBS for 90 days: (a) 25FD, (b) 50FD, (c) 75FD, and (d) 100FD samples. Every 10 cycles of 10 ⁴ are shown. The samples named by the molecular ratio of THF:GPTMS (as 1) and the drying method (freeze drying (FD)) which are 25FD, 50FD, 75FD, and 100FD.	122
Figure 5.15 The representative compression curves for hybrids after 90 immersion in PBS (a) oven drying (OD) (b) freeze drying (FD). The samples named by the molecular ratio of THF:GPTMS (as 1) and the drying methods which are 25OD, 25FD, 50OD, 50FD, 75OD, 75FD, 100OD, and 100FD.....	123
Figure 6.1 (a) Rhinoceros-designed gyroid scaffold; (b) Ti scaffolds printed using SLM (c) child volume of a SLM printed gyroid scaffold imaged using μ CT. (Gyroid scaffold is 16 mm)	127
Figure 6.2 Hybrid and gyroid constructs were sectioned using an IsoMet® 5000 Linear Precision Saw. (a) sample clamped on the sample stage and (b) applied cooling water, (c) cutting, and (d) cut sample with flat sample.....	130
Figure 6.3 Shear test apparatus using our bespoke universal shear test rig: (a) before shear test and (b) after shear test.....	131
Figure 6.4 Cartilage dissection: (a) the bovine cartilage was removed surrounding tissues; (b) cutting cartilage from the femoral condyle; (c) using biopsy punch to remove 8 mm of cartilage disc; and (d) harvested knee cartilage and ready for tribology test.	133
Figure 6.5 The purpose built Bio-Tribology Machine (BTM) was used to conduct tribology test for hybrid to against bovine cartilage, the linear motion was controlled by linear variable displacement transducers (LVDT) and motor. The friction force was recorded and the friction coefficient calculated.....	134
Figure 6.6 The optimisation of hybrid and gyroid scaffold integration. The (a-h) in left are the synthesis results and the (a-h) in right table are corresponding to the left image results. Red X means failure synthesis and red O is success synthesis. (Gyroid scaffold diameter is 16 mm).....	137
Figure 6.7 The optimisation of hybrid and gyroid scaffold based on the thickness and THF:GPTMS ratio.	138
Figure 6.8 μ CT images of hybrid and gyroid scaffold using Ilastik software to distinguish hybrid, gyroid, and empty spaces which are (a) Z, (b) Y, (c) X views of μ CT images, and (d) 3D reconstructed hybrid and gyroid scaffold. (Pink area is defined as hybrid, blue area as gyroid, and yellow area is empty space) (Scale bar is 1.5 mm)	140
Figure 6.9 μ CT image analysis: (a) optimised scaffold thresholding using Ilastik	

software, (b) using ImageJ script to calculate porosity of scaffold based on the μ CT images, and (c) channel width distribution calculated using ImageJ to calculate 300 pores. (Scale bar is 1.5 mm)	141
Figure 6.10 SEM images of hybrid and gyroid scaffold join surfaces (a) gyroid Ti scaffold only; (b) location of SEM images (SEM specimen stub with 12.5 mm diameter.); (c) inner region of hybrid integration into the Ti scaffold; (d) outer region of hybrid integration into the Ti scaffold.	142
Figure 6.11 Compression tests of hybrid and gyroid scaffold with 9 N preload and 1 mm/min compressive rate.	144
Figure 6.12 Shear test of hybrid and gyroid scaffold interface with 9 N preload and 1 mm/min shear rate.....	145
Figure 6.13 Cyclic test of hybrid scaffold for 90 days in-vitro stability evaluation. Every 100 cycles of 10^4 are shown.....	146
Figure 6.14 Friction coefficients of different materials sliding against knee cartilage versus time of sliding (a) cartilage against cartilage, (b) hybrid against cartilage, and (c) UHMWPE against cartilage using PBS as lubrication.	148
Figure 6.15 Average friction coefficients of tribology test results at 5 cycles and 600 cycles using PBS as lubrication: (a) cartilage against cartilage, (b) hybrid against cartilage, and (c) UHMWPE against cartilage.....	149
Figure 6.16 Surface roughness observations performed using confocal microscope. (a) cartilage surface before testing; (b) cartilage surface after tribology testing cartilage against cartilage; (c) hybrid surface before testing; (d) hybrid surfaces after tribology test hybrid against cartilage; (e) UHMWPE surface before testing; (f) UHMWPE surface after tribology test by UHMWPE against cartilage.....	150
Figure 6.17 Surface roughness of tribology samples (a) before and after cartilage against cartilage in tribology test, (b) surface roughness changed by hybrids against cartilages, and (c) surface roughness changed by UHMWPE against cartilage in tribology test.	152
Figure 6.18 Cell viability test for all samples were performed using MTT cell viability assay. Saos-2 human osteosarcoma cells were co-cultured with sample media for 24 hours and measured cell viability. (B/C is blank and control, PU is used for non-toxic negative control, PU is used for toxic positive control, Ti is used titanium gyroid scaffold, Hyb is used hybrid scaffold, and Ti-Hyb is used hybrid and gyroid scaffold).	153
Figure 6.19 SEM images of Saos-2 cell attachment (a) and (b) are cell attached on the titanium surface and (c) and (d) are cell attached on the hybrid surface.	155
Figure 6.20 ALP activity test of titanium gyroid scaffold and hybrid for 21 days.	156

Figure S 1. Solidworks 2D drawing views of shear testing moulds (a) bottom component, (b) sample holder mechanism, and (c) top cutting component. (Unit is mm)	184
Figure S 2. Solidworks 2D drawing views of tribology testing rig design (a) top sample holder and (b) bottom cartilage holder. (Unit is mm)	186
Table 2-1. The tensile moduli were evaluated between circumferential and radial direction and varies between different locations in the meniscus.....	34
Table 2-2 Comparison of compressive strengths and moduli of porous CP-Ti and Ti alloy made by different fabrication methods compared to trabecular bone and cortical bone.....	55
Table 4-1 The volume shrinkage and dimension of shrinkage as measured by calipers and from μ CT imaging (computational).....	76
Table 4-2 The shrinkage factors of hybrid materials (1-5) in different dimension from A to E as shown in Figure 4.7.....	78
Table 5-1 Hybrid synthesis reagent quantities where A refers to the moles of GPTMS and B refers to the moles of TEOS. The organic ratios was controlled by the THF/GPTMS ratio which are from 25:1 to 100:1.	97
Table 5-2 The shrinkage behaviours of hybrid monoliths were evaluated and compared using μ CT and Vernier calliper measurement. The dimensional shrinkages were measured by Vernier callipers.	107
Table 5-3 The full data of weight loss of hybrids for 90 days <i>in-vitro</i> test. The samples named by the molecular ratio of THF:GPTMS (as 1) and the drying methods (Oven drying (OD) and freeze drying (FD)) which are 25OD, 25FD, 50OD, 50FD, 75OD, 75FD, 100OD, and 100FD.	118
Table 5-4 The full data of ICP of hybrids for 90 days <i>in-vitro</i> test.....	119

List of Abbreviations

OA	Osteoarthritis
THF	Tetrahydrofuran
PolyTHF	Polytetrahydrofuran
SLM	Selective laser melting
GPTMS	3-glycidoxypropyltrimethoxysilane
ACL	Anterior cruciate ligament
ECM	Extracellular matrix
GAG	Glycosaminoglycan
CMI	Collagen meniscus implant
PU	Polyurethane
PCU	Polycarbonate-urethane
MPMA	3-trimethoxysilyl propyl methacrylate
CROP	In situ cationic ring-opening polymerization
PCL	Poly(ϵ -caprolactone)
TSD	N-[3-(trimethoxysilyl)propyl]ethylenediamine
MTMS	Organosilane methyltrimethoxysilane
APTMS	3-aminopropyltrimethoxysilane
ICPTS	3- isocyanatopropyl)triethoxysilane
APTES	3-aminopropyl)triethoxysilane
MPTMS	3-mercaptopropyl)trimethoxysilane
2D	Two dimensional
3D	Three dimensional
CAD	Computer-aided design
AM	Additive manufacturing

TGA	Thermogravimetric analysis
DSC	Differential scanning calorimetry
FTIR	Fourier Transform Infrared Spectroscopy
PBS	Phosphate buffered saline
SEM	Scanning electron microscopy
NMR	Nuclear magnetic resonance
ICP-OES/ICP	Inductively coupled plasma-optical emission spectrometer
FIB-SEM	Focused ion beam-SEM
EDS	Energy-dispersive X-ray spectroscopy
μ CT	X-ray micro-computer tomography
ISO	International organization for standardization
Saos-2	Sarcoma osteogenic
MTT	3-[4,5-dimethylthiazol-2-yl]-2,5-diphenyl tetrazolium bromide
α -MEM	Alpha-minimum essential media
FBS	Foetal bovine serum
DMSO	Dimethyl sulfoxide
BF ₃ EtO ₂	Boron trifluoride diethyl etherate
PFA	Perfluoroalkoxy
FD	Freeze drying
OD	Oven drying
CNC	Computer numerical control
PTFE	Polytetrafluoroethylene
DIC	Digital image correlation
PMP	Poly(methyl pentene)
Mw	Molecular weight
TKR	Total knee replacement

UHMWPE	Ultra-high molecular weight polyethylene
CP-Ti	Commercial product titanium
ALP	Alakaline phosphatase assay
pNPP	P-nitrophenyl phosphate

Chapter 1

Objectives

1. Aims

1.1. Motivation

Joints serve many important functions, such as supporting movement, and the knee is a combination of many components such as bone, ligaments, cartilage and fluid. The articular cartilage and meniscus protect the bone surfaces between the femur and tibia. There was an estimated 850,000 people in USA suffering from meniscus related surgeries about two decades ago [1], but this number increased to approximately one million just five years later, partly because sporting activities have become an indispensable part of life [2]. Approximately 40% of sporting injuries are related to knee injuries [3]. Common repair strategies try to preserve the meniscal tissue such as sutures, staples, and anchors, which do not work well for degenerative tears. Fifty percent of meniscal injury patients develop osteoarthritis (OA) within 10-20 years of surgery [4, 5]. OA is degeneration of the articular cartilage after which bone contacts bone, causing intense pain and loss of mobility. Irreparable meniscal lesions are usually treated by partial or total meniscectomy. In these circumstances further treatment with a meniscal substitute is necessary. Allograft (deceased donor) transplantation is the currently best solution available for meniscal substitute, but the problems are related to graft availability, size matching and secondary surgery. Moreover, meniscal allografts are observed to shrink [6] and the initial condition of the allograft may deteriorate over time [7]. Therefore, a promising material for meniscus replacement is an urgent unmet need.

1.2 Hypothesis

Our hypothesis is that a new inorganic/ organic hybrid material moulded to a

precise shape can be a revolutionary meniscus replacement device. The inorganic part provides stiffness and strength, and the organic part provides elasticity. Hybrid materials are based on the biomimetic concept of inorganic and organic networks interacting at molecular scale [8]. The SiO₂-poly(tetrahydrofluran) ["polyTHF"] hybrid material is synthesized by a combination of sol-gel process and polymerization of THF using 3-glycidoxypropyltrimethoxysilane (GPTMS) as a coupling agent [8], which provides critical covalent bonding between the organic and inorganic networks. The SiO₂ matrix provides stiffness and the SiO₂-polyTHF hybrid material is expected to demonstrate good mechanical properties for meniscus replacement application. The hybrid is a bouncy material and previous work showed it was possible to make low friction coefficient surfaces that can minimise the damage caused by artificial material to natural knee cartilage to preserve natural knee cartilage [9].

1.3 Fixation innovation

The meniscus has unusual anatomy for cartilage as it has a vascular region at the external periphery and is avascular in the inner regions. The vascular region contributes to the stabilization of menisci in knee joints as shown in Figure 1.1 [10]. The vascular region is attached medially to the medial collateral ligament, laterally to the menisofemoral ligament and to the transverse ligaments and joint capsule (Figure 1.1 (a)). The transverse ligament connects both menisci, which are anchored to tibia bone via the anterior and posterior horns[11]. Thus, an idea is to prepare two anchors to fix hybrid meniscus to tibia bone via the similar location of anterior and posterior horns as shown in Figure 1.1 (b). Furthermore, meniscus replacement material should be designed to mimic the vascular and avascular regions in the structure.

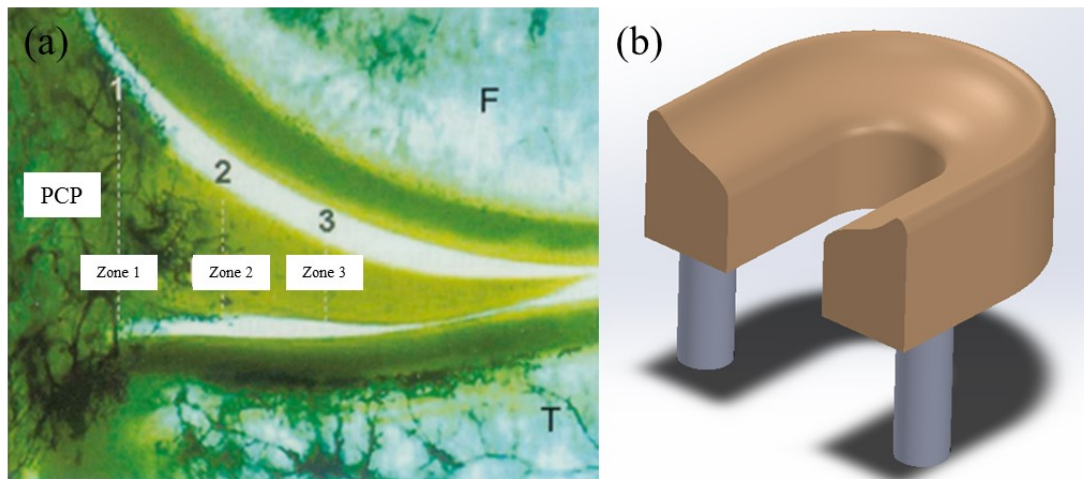


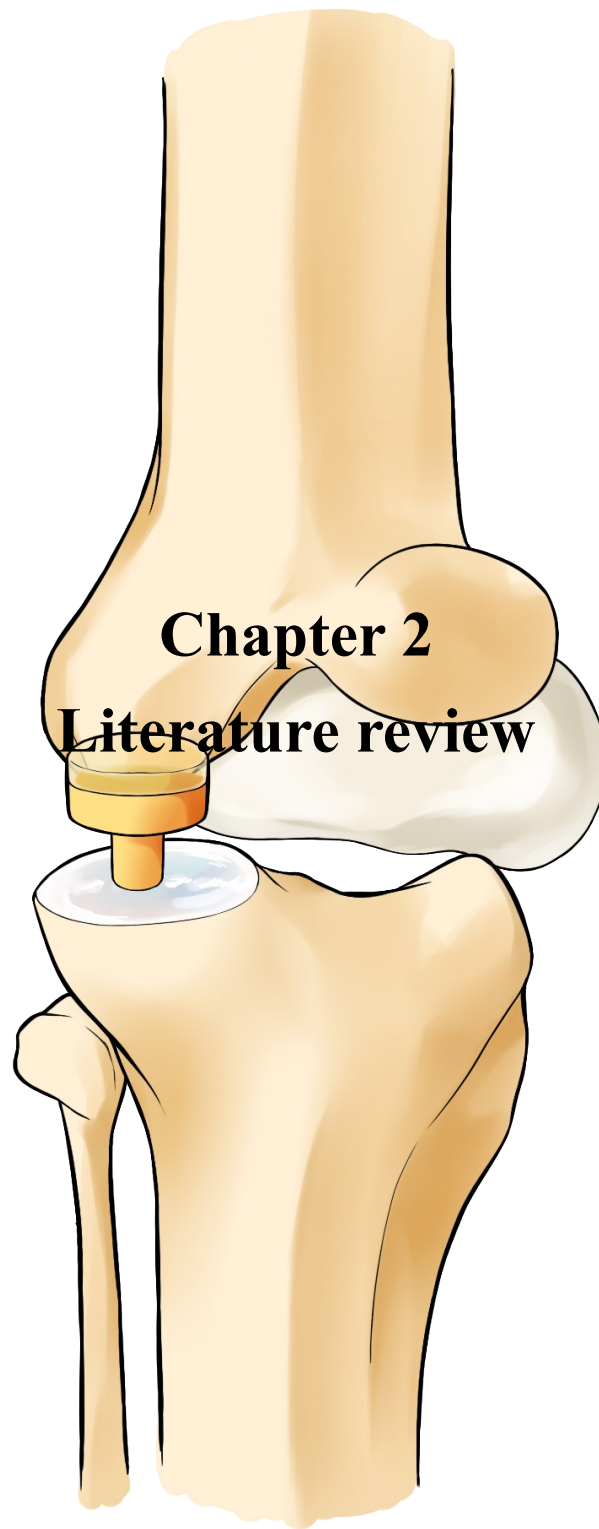
Figure 1.1 An optical image of a cross section of a meniscus: (a) Zone 1 is fully vascularized; Zone 2 is at the border of the vascular area; and Zone 3 is within the avascular area of the meniscus, adapted from [10]; F: femur; T: tibia; PCP: perimeniscal capillary plexus. (b) 3D design of two biological anchors (grey) to fix the hybrid (brown) meniscus device to the tibia bone via the location of anterior and posterior horns.

1.4 Aim of this project

The aim of this project was focused on the development of new hybrid synthetic meniscus for knee cartilage replacement. There are several research objectives:

- 1.1. Synthesis of hybrid cylinders with suitable mechanical properties: Investigating the effect of ratio of THF and GPTMS compositions (100:1 to 25:1 molar ratio) and different drying methods (oven drying and freeze drying) on mechanical properties; in compression cyclic loading, in dry and wet conditions.
- 1.2. Mould design based on the material properties and meniscus biomimetic structure.
- 1.3. Use of Rhinoceros and Solidworks software to design a gyroid structure for Additive Manufacturing of the bone anchors, and 3D printing by selective laser melting technique with design optimisation.

- 1.4. Hybrid synthesis and process optimisation for integration with the titanium anchors.
- 1.5. Matching the tribological properties of the meniscus device with living knee cartilage to test the friction coefficient between hybrid and knee cartilage.
- 1.6. To understand cell response on hybrid and gyroid scaffolds.



2. Literature review

2.1 Meniscus

2.1.1 Introduction

The meniscus is a cushion structure made of cartilage that fits within the knee joint between the tibia and the femur. The anatomy of the knee joint is shown in Figure 2.1 (a) [12]. There are two menisci inside each knee joint which are medial meniscus and lateral meniscus. With the medial meniscus, the anterior and posterior “horns” are separated from each other and from the anterior cruciate ligament (ACL). The medial meniscus is crescent-shaped which covers 50% of the medial tibial plateau and transmits approximately 50% of the total joint load of the knee medial compartment thus protecting the articular cartilage from the excessive force [13]. The lateral meniscus is more circular and covers 70% of the lateral tibial plateau and transmits 100% of lateral knee compartment [13]. They are providing joint congruity, stabilisation, and lubrication for joint preservation. During weight-bearing activities, the menisci dissipate axial loads and contain hoop stresses. The forces are transduced throughout the knee meniscus as shown in Figure 2.1 (b). Although the lateral meniscus transmits 100% of the lateral knee compartment, the medial meniscus is more commonly injured because it is firmly attached to the tibia by the medial collateral ligament and the joint capsule [14]. According to a medial meniscus tear report by Smith and Barrett [15], more than 75% of medial meniscal tears by rupture of the ACL occur in the peripheral posterior horn and are usually chronic tears. However, the total axial loads applied in the joint were strongly dependent on bending degree and knee flexion and health. Contact area between the articular cartilage of the femoral condyles and the tibial plateau decreased 4% for each 30° of flexion and 85% more axial load is applied in the joint while the knee is bent at 90° [12].

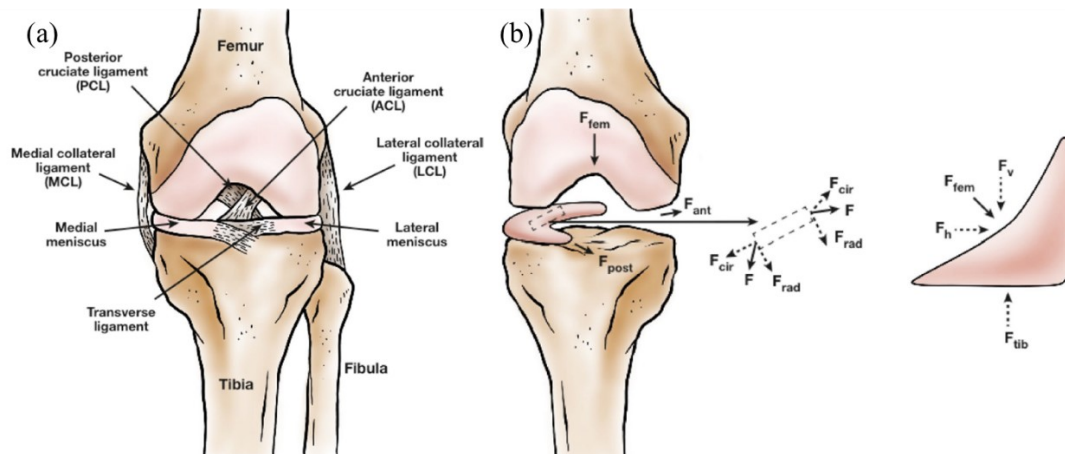


Figure 2.1 (a) Anatomy of knee joint; (b) illustration of how the force is transduced throughout the knee meniscus. The meniscus will transduce compressive loads to circumferential tensile loads during movements. Adapted from [12].

Meniscus injury commonly occurs in human knee due to abnormal mechanical force by exercise or degeneration by ageing. Historically, medial meniscal root tears have been treated conservatively with nonsurgical treatment, suture, and partial meniscectomy or meniscectomy [16, 17]. Moreover, meniscus deficiency and meniscectomy have been shown significant cartilage degeneration to lead to osteoarthritis (OA) [17, 18]. The biomechanical effects of total removal of the lateral meniscus, with 50% decrease in the total contact area, result in a 235-335% increase in peak local contact load [19]. Therefore, promising new biomaterials for meniscus replacement are required.

2.1.2 The properties and structure of human meniscus

Human meniscus is highly hydrated, containing 72 wt% of water, 0.12 wt% of DNA, 22 wt% of collagen (extracellular matrix, ECM), 0.8 wt% of glycosaminoglycan

(GAG) and cells such as chondrocytes, microvascular endothelial cells, fibrochondrocytes and so on [20, 21]. The above compositions vary depending on age, injuries, and other pathological conditions [21]. In the dry weight of the meniscus, collagen makes up the majority 75% organic matter and acts as the main fibrillar component (99.4% of collagen and 0.6% of elastin [21]). Collagen types I, II, III, V, and VI have been found within the meniscus with varying quantities in each region and regional variation as shown in Figure 2.2 [12]. Collagen type I is the most predominant for >90% within the whole tissue [21] and in zone 1 collagen type I is approximately 80% with other collagen types present at less than 1% by dry weight. In zone 3, collagen makes up 70% of the tissue and 60% belongs to collagen type II and 40% belongs to collagen type I by dry weight [12]. Furthermore, zone 1 is a vascularized section and has the intrinsic ability to heal itself as well as being surrounded circumferentially by large nerve bundles and smaller nerves running radially [22]. Zone 2 is the mid-section which has cells more fibroblast-like in appearance. Zone 3 region is located in the inner section, which consists of smaller and rounder chondrocyte-like cells. Zone 2 and 3 are avascular, have no innervation and most innervation are the horns of the menisci, which are attached to bone through insertional ligaments. Normally all meniscus cells present the same cellular morphology in terms of both size and shape with no regional variations. However, the cells are modified themselves to adapt the certain environment and functionalization. Zone 1 presents fibroblast-like cells with long cell extensions, which facilitate communication with other cells and the ECM [23]. Zone 2 and 3 present round fibrochondrocytes and chondrocyte-like cells, meanwhile, relative abundance of collagen type II and aggrecan present in the inner region [24]. Cells present in superficial zone of the meniscus have been shown to have a flattened, fusiform morphology without cell extensions. These cells are possibly specific progenitor cells with therapeutic and regenerative capabilities [25]. In summary, cells modify their

phenotype and incorporate with ECM to adapt certain applications and environments in terms of cell morphology, functionalization, and patterns of ECM.

The meniscus is attached to the tibia via coronary ligaments (Figure 2.3). The meniscus attachment can be divided into three parts: the anterior end, posterior end, and peripheral area. The anterior end is attached to the anterior intercondyloid fossa of the tibia, in front of the ACL; the posterior end is fixed to the posterior intercondyloid fossa of the tibia, between the attachments of the lateral meniscus and the posterior cruciate ligament. The peripheral part is fused with the tibial collateral ligament in zone 1 (Figure 2.2). The points of attachment are widely separated at two endpoints and peripheral areas which make the meniscus stable and less mobile on the tibia. Therefore, the design of meniscus fixation is referred to as natural attachment. The artificial meniscus is attached at two endpoints for structural stability and creates surface tunnels on the peripheral area which allow peripheral tissues ingrowth to firm it on the tibia plateau.

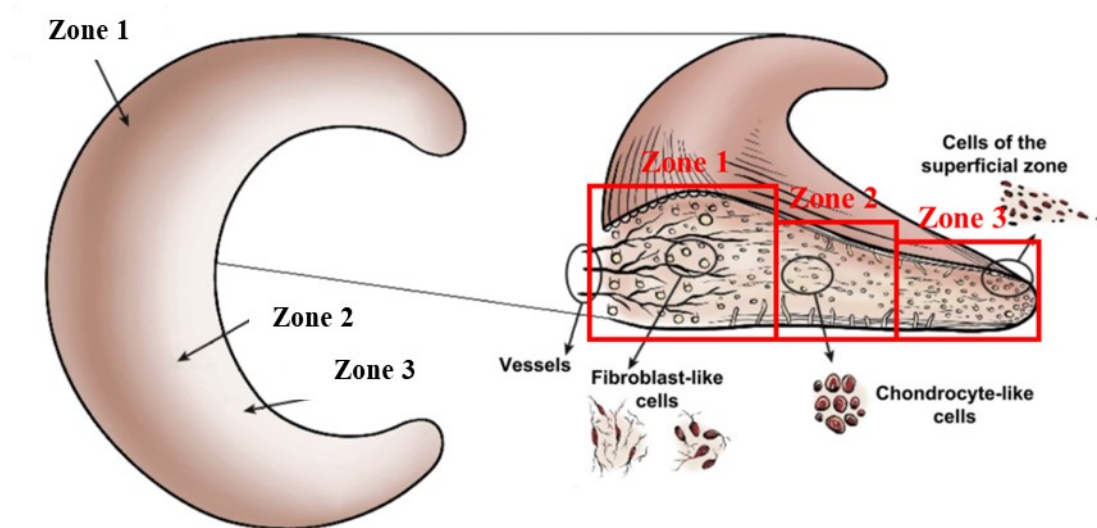


Figure 2.2 Schematic diagram of human meniscus showing regional variations in vascularization and cell populations of the meniscus. Left: the top view of meniscus

which consists of three regions from outer to inner zone which are zone 1, zone 2, and zone 3. Right: Zone 1 is a vascularized section, zone 2 is in middle section which has more fibroblast-like in appearance, and zone 3 region is located in inner section which consists smaller and rounder chondrocyte like cells. Adapted from [12].

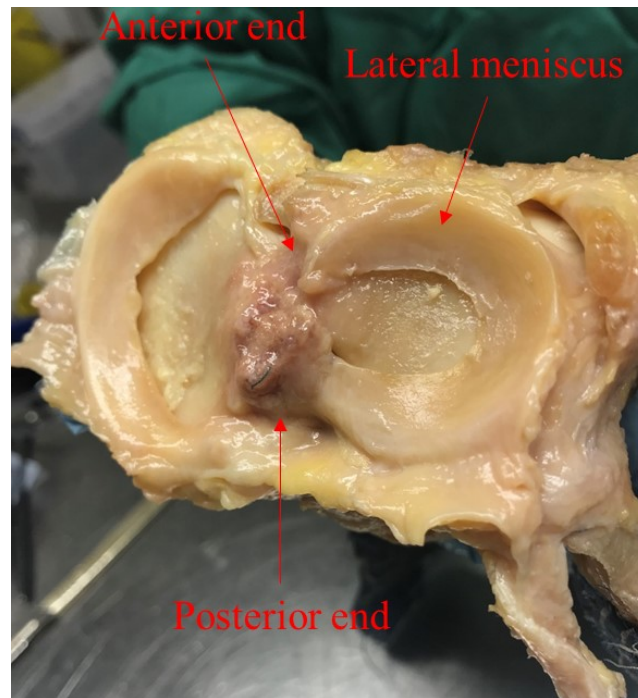


Figure 2.3 Photograph of human knee dissection made in Prof Andrew Amis' group. The lateral meniscus is attached on the tibia, whereas anterior and posterior ends attach on anterior and posterior intercondyloid fossae of the tibia. The peripheral area is attached by tibial collateral ligament.

The meniscus acts as a load distributor for knee preservation by converting vertical compressive loads into horizontal hoop or circumferential stresses. The inner structure of the natural meniscus is complex. Collagen exists at the nanoscale as fibres and arranges in parallel to form collagen bundles of varying diameters in different directions [26]. A schematic diagram of the internal structure of the human meniscus is shown in

Figure 2.4. The surface is formed by random orientation collagen fibres approximately 10 μm in thickness 35 nm in diameter. The lamellar layer is formed by collagen fibril bundles approximately 150-200 μm in thickness which have radial direction in the external circumference of the anterior and posterior segments and intersect at various angles as a rhomboid in other segments. The central part is formed by circular collagen fibre bundles with a diameter of 20-50 μm which perform a circumferential direction in all segments of the meniscus. Furthermore, there are loosely arranged collagen fibrils running in a centripetal direction between the circular fibre bundles in central part [26]. Meniscal load distribution is time dependent due to the exudation of water out from the ECM. A small amount of GAG and or chains of proteoglycan aggregates in ECM these hydrophilic proteoglycan macromolecules contribute water-retention and electrostatic-repulsion properties. The exudation of water from GAGs improves compressive stiffness and joint lubrication as water is forced into the ECM space [27]. The mechanical properties of menisci are strongly dependent on their structure. For instance, fibre-reinforced meniscus scaffolds were found to share axial compressive loads via generation of circumferential tensile loads within the scaffold [28]. The meniscus resists axial compression with an aggregate modulus of 100-150 kPa on either femoral or tibial side at different locations of the human meniscus by cube shaped specimens [21]. The tensile moduli were evaluated between circumferential and radial direction with whole menisci, as shown in table 2.1. The circumferential tensile modulus is significantly larger than the radial tensile modulus. Meanwhile, the surface of the meniscus is constituted by random orientation and lamellar collagen, and those porous ingrowth by the surrounding tissues to improve fixation of the meniscus. Thus, the structure of the meniscus (collagen arrangement) is a crucial point in research of mechanical properties and meniscus fixation for new material on meniscus replacement application. In this study, the aim was to develop a synthetic meniscus with improved mechanical

properties which match the way it deforms under load.

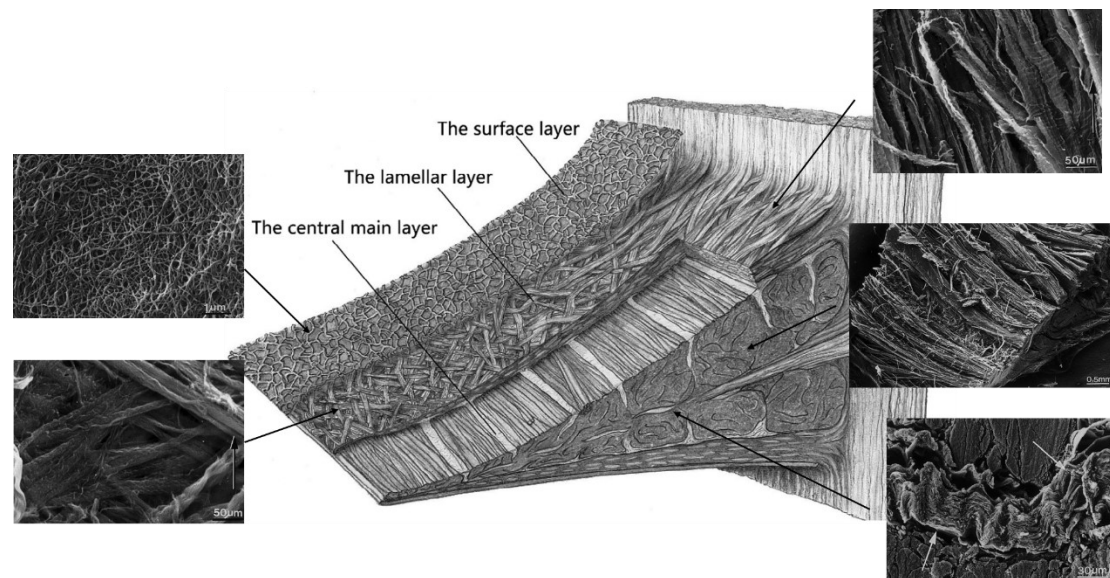


Figure 2.4 Schematic diagram of internal structure of human meniscus. There are three layers of collagen fibres with certain patterns which are random orientation collagen on surface layer, lamellar orientation collagen in lamellar layer, and parallel oriented collagen fibre bundles in central main layer. Adapted from [26, 29].

Table 2-1. The tensile moduli were evaluated between circumferential and radial direction and varies between different locations in the meniscus.

Location	Tensile modulus (MPa)			
	Tangential direction		Radial direction	
Medial meniscus:				
Anterior	159.62±26.2	141.2±56.7	106.21±77.95	48.31±24.35
Central	228.8±51.4	116.4±47.5	77.95±25.09	46.20±27.56
Posterior	294.1±90.4	108.4±42.9	82.36±22.23	32.55±11.27
Lateral meniscus:				
Anterior	159.1±47.4		124.58±39.51	48.47±25.67
Central	228.8±51.4		91.37±23.04	45.86±24.20
Posterior	294.1±90.4		143.73±38.91	29.85±12.77
Reference	[30]	[31]	[32]	

2.2 Meniscus repair and replacement

2.2.1 Meniscus lesions

For the mature meniscus, only a certain portion of the tissue receives blood supply which is segmental and regional surrounding the peripheral tissues. The vessels penetrate around 10 to 25 % of the width of the lateral meniscus and 10 to 30% of the width of the medial meniscus as shown in Zone 1 in Figure 2.2 [12]. These vessel distributions greatly determine the self-healing ability of the meniscus. Meniscus lesions can be divided into two groups: degenerative and traumatic lesions. The degenerative lesion is typical in older people, although this kind of lesion can occur in all age groups [33]. A meniscus lesion is a common incidental finding on magnetic resonance imaging (MRI) in both symptomatic and asymptomatic knees [34]. The

degeneration of the meniscus can occur by repetition of micro-trauma, osteoarthritis, diminished and vascularization [35, 36]. The characteristics of meniscus tissue vary according to age, tear pattern, and pathological conditions. These include the water content, cells, extracellular matrix, collagen, and adhesion glycoproteins [21]. The MRI demonstrated degenerative meniscus including cavitation, softened tissue, fibrillation, or complex tear patterns as shown in Figure 2.5.

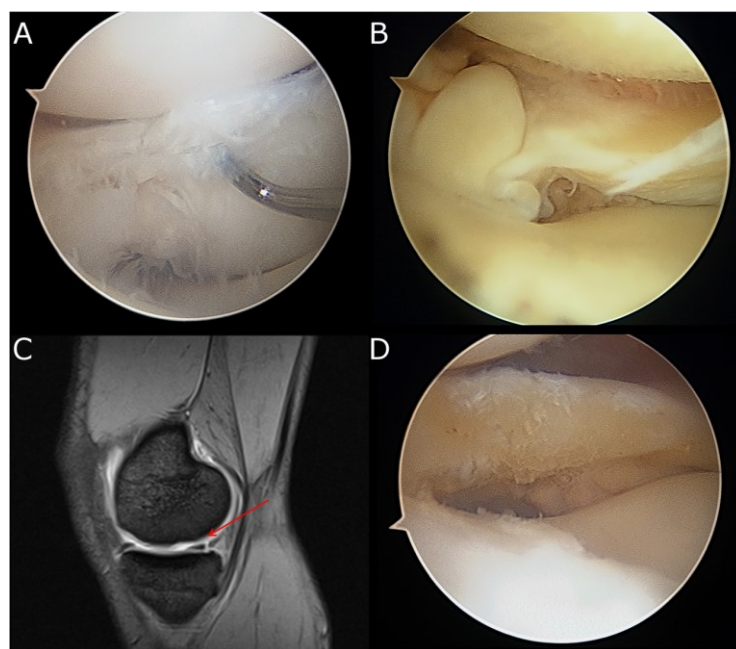


Figure 2.5 Typical fibrillation of a degenerative meniscal lesion (a); complex tear combining flap and horizontal tear (b); MRI lateral view of longitudinal medial meniscus tear (red arrow) (c); final look after meniscectomy reducing the volume of meniscal tissue (d). adapted from [37].

On the other hand, a traumatic meniscus tear is typically associated with an acute event; from high energy impact to rupture of the meniscus tissue. The schematic diagram of types of meniscus tears are shown in Figure 2.6. The most representative patterns for traumatic tears are longitudinal, bucket-handle, flap tear, and radial tears.

On the contrary, the most representative type of tear for the degenerative lesion is the horizontal tear [38]. The meniscal root injuries are widely reported to be degenerative, traumatic and frequently combined with acute anterior cruciate ligament rupture [39]. Untreated meniscal injuries can lead to the rapid development of osteoarthritis due to meniscal extrusion and the loss of resistance to hoop stress [40].

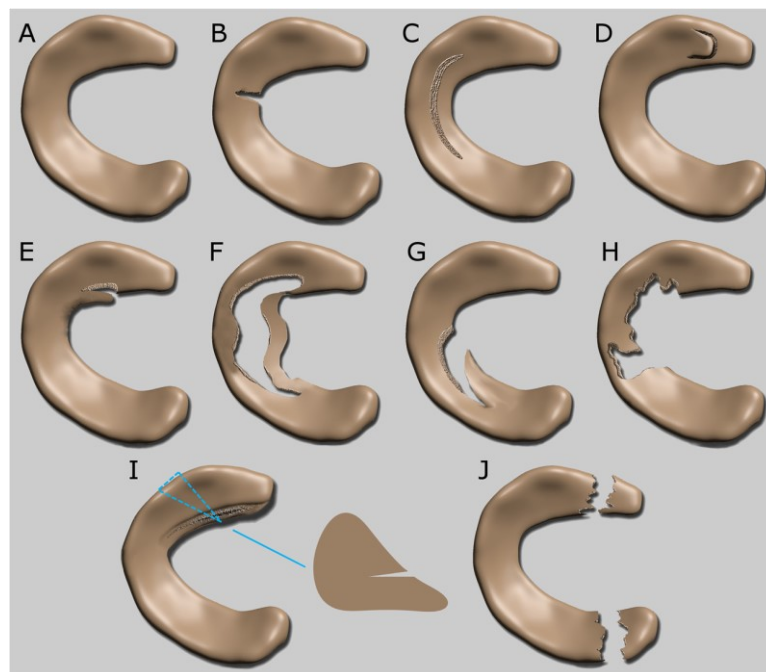


Figure 2.6(A) Illustration of normal meniscus, and common types of meniscus tears: (B) radial tear, (C) longitudinal tear, (D) horizontal flap, (E) vertical flap, (F) bucket handle tear, (G) oblique/parrot beak lesion, (H) complex degenerative, (I) horizontal tear, (J) root tears. Adapted from [37].

2.2.2 *Meniscus repair and fixation*

According to the limitation of meniscus self-healing ability, surgical and medical advice are intended to preserve the original meniscus and extend implement medical treatment. The International Society of Arthroscopy, Knee Surgery and Orthopaedic

Sports Medicine (ISAKOS) reported a comprehensive classification of meniscal tears that provides sufficient interobserver reliability for pooling of data from international clinical trials designed to evaluate the outcomes of treatment for meniscal tears. The classification is based on tear depth, rim width, radial location, central to the popliteal hiatus, tear pattern and length, quality of the tissue, and existing meniscus tissues [41]. This classification index can suggest a proper treatment in clinical practice. As aforementioned, the periphery is filled of blood supply and has self-healing potential. Therefore, several biologic augmentation techniques have been developed, including mechanical stimulation [42], marrow venting procedures [43], fibrin clots, platelet rich plasma [44], and stem cell therapies [45]. These methods are applied on the high vascular zones to promote neovascularisation. Although, these methods have some excellent results clinically, they depend on the patient's condition and are more suitable for young patients. Meniscal repair is most often performed using arthroscopy. The arthroscopic surgery is to investigate tear pattern and location and is useful for larger tears where multiple sutures may be needed. The suture techniques include inside-out, outside-in, and all-inside techniques (Figure 2.7). These suture techniques are utilized in different types of tear for example the outside-in technique is often applied on the anterior horn midportion tears and inside-out and all-inside techniques are often used for posterior meniscal tears or larger tears [46, 47]. Outcomes of meniscal repair are based on a number of factors and these suture treatments have an excellent capacity for healing and setting of an acute peripheral tear, based on a recent study evaluating 80 patients (age range 18-49 years) with vertical longitudinal meniscal tears reported an 85% of healing rate at a mean of 51.2 months post-repair [48]. In a revision meniscus repair study, 79% of patients had no pain and no mechanical symptoms six years post-operation [49]. Again, these repair techniques are favourable for the high vascular zone and even younger patients maybe facing a higher risk of failure of the revision meniscus

repair [49]. Consequently, meniscal injuries judged to be irreparable should undergo partial or total meniscectomy in an attempt to save as much meniscal tissue as possible.

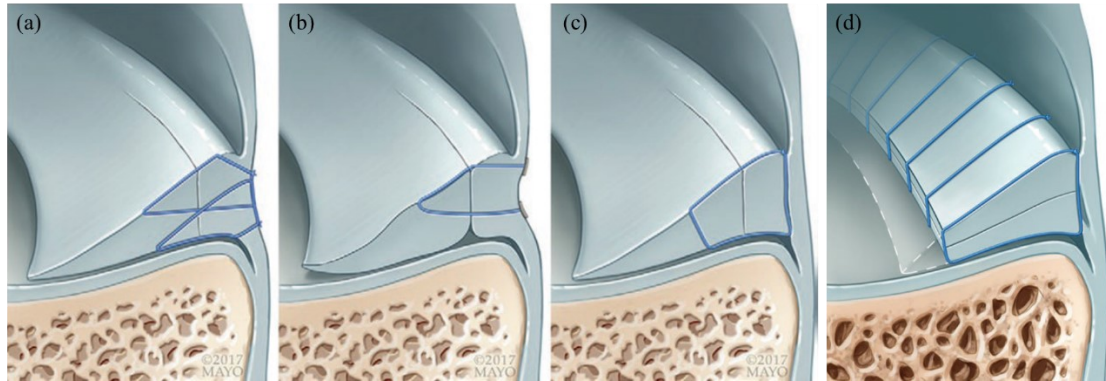


Figure 2.7 Schematic diagrams of (a) surgical repair on a vertical longitudinal meniscal tear using an inside-out repair with knots tied over the capsule, (b) all-inside anchor-based construct, (c) all-inside knot-tying technique, and (d) a horizontal cleavage meniscal tear using multiple all-inside circumferential compression sutures placed with a self-retrieving suture-passing device followed by arthroscopic knot tying. The images are adapted from [50] and the original images from Mayo Foundation for Medical Education and Research.

2.2.3 *Current meniscus replacement options*

Current meniscus replacement materials are limited [51]. Some commercial products have received the CE mark for use in Europe, such as the collagen meniscus implant (CMI[®], Stryker, USA), a polyurethane (PU) implant (Actifit[®], Orteq Sports Medicine Ltd., UK), and polycarbonate-urethane (PCU) the Meniscus Implant (NUsurface[®], Active Implants LLC, USA). However, the CMI received the first and only US Food and Drug Administration (FDA) approval so far, in 2016. The CMI is made of highly purified type I collagen fibres from purified bovine achilles tendon

supplemented with GAG [52]. The CMI implant was sutured by bioabsorbable wire to the host meniscal remnant along the periphery. Long term survival rates are unknown. Actifit and NUsurface are made by synthetic polymers. The Actifit implant is polyurethane polymers consisting of biodegradable polyester segments combined with semi-degradable stiff segments. An arthroscopy is used to position the implant, which is then sutured to the remaining native meniscus using horizontal stitches and to the meniscal wall using vertical stitches. [53]. There are unknown long-term effects of treatment with the Actifit implant due to semi-degradable property [54]. The first synthetic meniscus-like implant (NUsurface) was made by PCU, which is a non-degradable material, and the initial results show that primary PCU meniscus transplantation may protect, but not completely prevent articular cartilage degenerative changes following meniscectomy [55]. The PCU meniscus was secured with a tightening metal bolt by drilled tunnels on the tibia and sutured through ligaments. An ideal meniscal graft would protect the articular cartilage, by preventing the progression of OA, with good mechanical properties and biological response with surrounding tissues [56]. Those commercial products were designed in porous structures or with semi-degradable property which suggest insufficient mechanical strength and stability.

2.3 Hybrid materials

2.3.1 Definition of hybrid materials

Hybrid materials are a combination of inorganic and organic materials which interact at the molecular level and behave as one material. This molecular level integration behaves as a single phase compared with composites, which are usually two separate phases. The phase separation can possibly form weak points. Hybrid materials inherit properties from both parts with the inorganic part providing mechanical strength

and the organic part providing elasticity [58]. The sol-gel method can produce silica under an ambient environment [59], growing a silica network by polymerization of [59] hydrolyzed tetraalkyl orthosilicates (sol) precursors to form SiO₂ networks (Figure 2.8). Hybrid materials can be prepared by dissolving polymer precursors into the sol. Both inorganic and organic parts can be formed through simultaneous polymerization of the organic monomer and the sol-gel precursors. This process can enable the formation of covalent bonds or other weak chemical bonding between the networks [60].

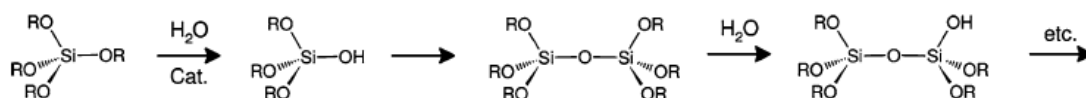


Figure 2.8 Schematic of the sol-gel process that includes the hydrolysis tetraalkyl orthosilicates and their subsequent condensation to produce 3D SiO₂ networks as gels. Adapted from [61].

2.3.2 Classification of hybrid materials

There are different macromolecular structures and phase connectivity methods in hybrids [60]. The categories of hybrid material can be based on these properties as four classes. Class I and II hybrids are formed using polymer produced ex-situ, whereas for Class III and IV hybrids the polymer is formed simultaneously with the sol-gel process. In Class I and III hybrids, interactions between inorganic and organic components are with weak bonds such as hydrogen bonding, van der Waals or electrostatic forces [59]. In Class II hybrid materials, the inorganic building blocks are covalently bonded to the organic polymer, which demonstrate a strong structure stability and controlled biodegradation. The polymer is introduced into the sol ready-formed. Class IV hybrids

go a step further than Class II in that the polymerization of the polymer occurs in the same pot as the inorganic polymerization [60].

Class II and IV hybrids have strong interactions between inorganic and organic components at the molecular level, resulting in non-degradable or controlled congruent degradation and the possibility for tailorable mechanical properties [62]. Our silica/polyTHF hybrid is Class IV. The schematic chemical structure of silica/polymer Class II or IV hybrid material is shown in Figure 2.9 [63]. The interpenetrating networks of inorganic and organic components are indistinguishable structure above the nanoscale. The polymer is mechanically entrapped in the silica network during condensation. Covalent bonding between the components can be achieved using a coupling agent molecule, a short chain molecule that contains organic moiety on one side and three alkoxy silane groups on the other side which can be used to link the silica and the polymer. Polymers containing nucleophilic groups, such as $-OH$, $-COOH$ or $-NH_2$ groups, can be used to react with a coupling agent. Alternatively, a polymer can be used (or synthesized) that already contains silane bonds incorporated with sol, the terminal groups hydrolysed to form silanol groups, which can condense with other silanol groups from hydrolysed sol and bonding the silica network [64]. A coupling agent used in this research is 3-glycidoxypropyltrimethoxysilane (GPTMS), which has an epoxy ring on one end that is susceptible to nucleophilic attack and three methoxysilane groups on the other end of the molecule [65]. GPTMS was also previously used for natural polymer hybrids such as gelatin and gives the ability to tailor both mechanical properties and dissolution properties [66]. Methacrylate based polymers can be synthesized with 3-trimethoxysilyl propyl methacrylate (MPMA) units that present pendent siloxane groups that can partake in the silica sol-gel reaction. This kind of coupling agent can potentially improve the physical properties of hybrids [67].

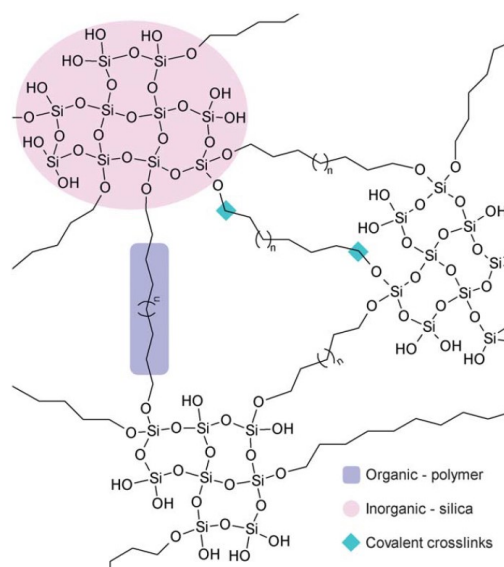


Figure 2.9 Schematic of the chemical structure of silica/polymer hybrid material. Adapted from [63].

2.3.3 *SiO₂/polyTHF based hybrids*

A novel self-healing Class IV hybrid material was reported by Tallia et al. [8]. Unique properties were generated by combination of intermolecular forces between two organic components which demonstrate London forces and dipole-dipole interactions between the polymer and silica networks [68]. The hybrids were synthesized by in situ cationic ring-opening polymerization (CROP) within the sol-gel process, creating silica/poly(tetrahydrofuran)/poly(ϵ -caprolactone), SiO₂/polyTHF/PCL hybrids [8]. PCL-diol was first oxidized by TEMPO oxidation to synthesize PCL-diCOOH, which provided -COOH groups that were then utilized for reaction with GPTMS in tetrahydrofuran (THF). The nucleophilic groups opened the epoxy ring on the GPTMS, but the GPTMS also acted as an initiator for the polymerization of THF solvent (in situ CROP), producing polyTHF. The polyTHF acts as a second organic phase to form a

unique tri-component hybrid material in the presence of a catalyst ($\text{BF}_3 \cdot \text{OEt}_2$) [8]. The schematic of the CROP reaction is shown in Figure 2.10. Firstly, $\text{BF}_3 \cdot \text{OEt}_2$ catalyst opens the epoxy ring on the GPTMS at step I. The THF nucleophilic groups attack the GPTMS epoxy ring and initiate CROP at step II and chain elongation at steps III–IV. Finally, a covalent bond forms between polyTHF and GPTMS. GPTMS is covalently bonded with polyTHF, which is ready to form hybrid by interaction with sol-gel silica as shown in Figure 2.7. The research results suggest biodegradable SiO_2 /polyTHF/PCL hybrids are suitable for cartilage regeneration material due to elastomeric bouncy behaviour, controllable mechanical strength, and cell recognition [8]. Furthermore, the hybrids showed elastomeric deformation under tension and the ability to recover the initial shape when the load was released, until fracture. As organic content increased from 2.5 wt% to 39 wt%, true strain to failure decreased from $25.5 \pm 3.3\%$ to $2.4 \pm 1.5\%$ and true stress to failure increased from 0.12 ± 0.05 MPa to 1.42 ± 0.47 MPa [8]. Our hypothesis is that a non-degradable version of the hybrid, i.e. SiO_2 /polyTHF, is potentially suitable material for a meniscus replacement application.

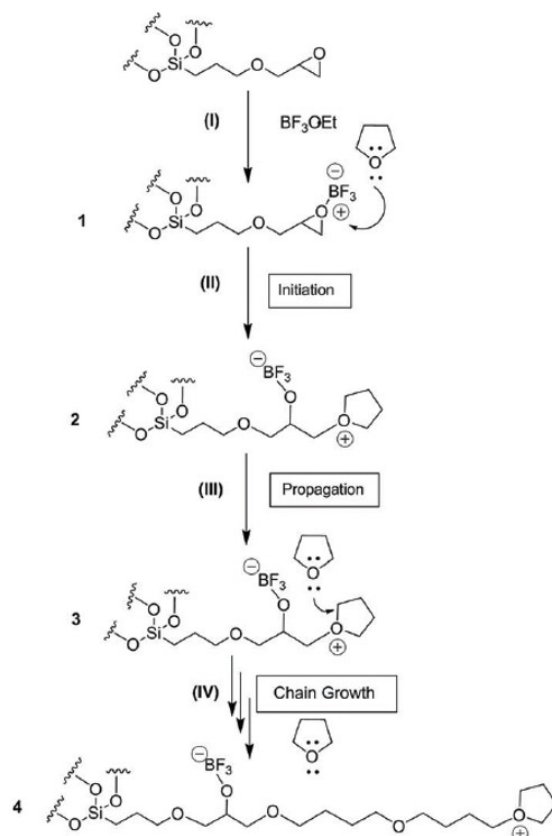


Figure 2.10 The schematic diagram the CROP reaction of THF, using GPTMS as an initiator, adapted from [8].

2.4 Chemistry/structure/property relationships of hybrids

2.4.1 Silica based hybrid applications

Silica-based hybrids can be made with different polymers, which will need different coupling agents, for applications in multiple fields. For example, N-[3-(trimethoxysilyl)propyl]ethylenediamine (TSD) can be used as a coupling agent for combining TEOS and Fe_3O_4 magnetic nanoparticles as a magnetic hybrid [69]. Many different organosilanes were reported as potential coupling agents such as trifunctional organosilane methyltrimethoxysilane (MTMS) [70], 3-aminopropyltrimethoxysilane (APTMS) [71], (3-isocyanatopropyl)triethoxysilane (ICPTS) [72], (3-

aminopropyl)triethoxysilane (APTES) [73], (3-mercaptopropyl)trimethoxysilane (MPTMS) [74], and (3-glycidoxypropyl)trimethoxysilane (GPTMS) and these coupling agents are conducted widely applications such as anticorrosive coating [71, 75], electrolyte [70], drug delivery, bioimaging [76] and other applications.

2.4.2 *SiO₂/polyTHF/PCL hybrid application*

This study focuses on SiO₂/polyTHF/PCL hybrids first reported by Tallia et al. [77]. Modern high tech glassy materials are needed to fulfil the complex engineering design criteria for novel applications, but they are usually brittle and have no self-healing ability. This advanced material system not only provides unprecedented mechanical properties, including bouncy elasticity, degradability but also has the intrinsic ability to self-heal autonomously [8]. The self-healing property of hybrids have been shown in Figure 2.11 (a). Images of Si0-CL530 to Si70-CL530 (PCL-diol (M_n = 530 Da)) demonstrate excellent self-healing 5 seconds after the creation of defects. A similar result was reported by Fan et al. in 2021 [78]. The surface morphologies of the self-healing process have been observed by scanning electron microscopy (SEM) as shown in Figure 2.11 (b-d). The SEM images captured a clear healing process by bringing together two fractured surfaces. This process is similar to natural tissue repairing. This ability can potentially be useful for smart glass application. Meanwhile, this hybrid is 3D printable without any additional binders which can be conveniently 3D printed as a designed scaffold. The 3D scaffold can provide a certain structure for tissue engineering applications. The SiO₂/polyTHF hybrids are theoretically nondegradable, however, the PCL brings degradability in this material system. To sum up, SiO₂/polyTHF/PCL hybrids demonstrate excellent self-healing properties, controllable mechanical properties, structure and degradation ability which are suitable

as a multifunctional materials and potential for cartilage regeneration and tissue engineering applications.

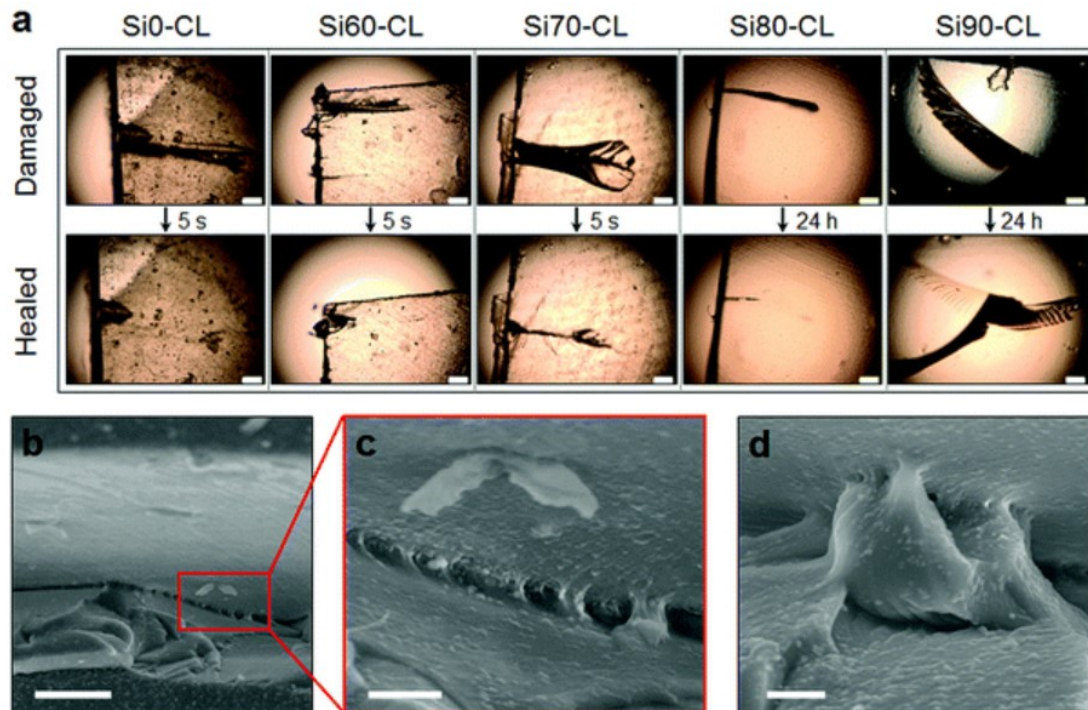


Figure 2.11 (a) Optical microscope images of SiO₂/polyTHF/PCL hybrids of the five hybrid compositions from Si0-CL530 to Si90-CL530 before creation of a defect (top) and after self-healing at RT (bottom). Images for Si0-CL530, Si60-CL530 and Si70-CL530 were taken after 5 s from defect creation; images for Si80-CL530 and Si90-CL530 (Si(wt%)-CL530 refers to TEOS (Si)/PCL-diCOOH (CL (Mn = 530 Da)), when 0% Si-100% CL is present (Si0-CL) and 60% Si-40% CL is present (Si60-CL)) were taken after 24 h from defect creation. Scale bar = 500 μ m and (b–d) SEM images of a defect created on a Si0-CL sample. From b-d images show the bridging effect along the fractured surfaces during the self-healing process. The margins of the defects are visible in (b) and a magnification of the bridging is reported in (c); this behaviour was confirmed also on other areas of the sample (d). Scale bars: 50 μ m in (b); 10 μ m in (c and d) images adapted from [8].

2.4.3 Non-degradable SiO₂/polyTHF hybrids

There are very few reports on the SiO₂/polyTHF hybrid system, most of which are to make the hydrolysis TEOS and mix with polyTHF for thin film or surface coating applications [79, 80]. However, our SiO₂/polyTHF hybrid system is synthesised by two-pot synthesis and forms a covalently bonded SiO₂/polyTHF hybrid system as a bulk specimen. The synthesis technique is similar to that reported by Tallia et al. but without PCL [8]. This covalent bonding can provide strong chemical interaction and make the bulk structure non-degradable. Various studies on the mechanical properties of a new SiO₂/PolyTHF hybrid with outstanding elastic mechanical properties were performed by previous MSc students Seyed Ataollah Naghavi, Manishankar Chellappan, and Enric Juan Alcocer under the supervision of Dr. Gloria Young and Dr. Francesca Tallia. This material has good elasticity, can bounce and demonstrates excellent mechanical properties. Meanwhile, the non-degradable property can make it a potential candidate for cartilage replacement.

2.5 Additive manufacturing

2.5.1 3D printing technique

Additive manufacturing (AM) technologies are well known as 3D printing techniques or additive layer manufacturing which are capable for fabricating materials with complex free form geometries and overcoming certain technical issues over conventional manufacturing techniques. AM processes can be classified into seven classes: vat polymerisation, material extrusion, sheet lamination, powder bed fusion, material jetting, binder jetting and directed energy deposition, respectively. Each AM

process has been developed due to its different working mechanisms for specific materials in polymers, ceramics, and metals. Polymers are generally matched low melting point and chemically modifiable properties which are suitable for vat photopolymerisation and material extrusion technique. Vat photopolymerisation uses liquid photopolymer in a vat and selectively cures it by light activated polymerisation. Material extrusion dispenses materials through heated nozzles and fuses material together. Ceramics are intrinsically brittle, have higher sintering temperature, and have low fracture toughness compared with metals which make it difficult to manufacture a high quality, defect-free object. Although conventional manufacturing processes can be built, the parts of designed geometry and dimension, high process temperature and low ductility require long and expensive later processes such as secondary heat treatment. Binder jetting AM can be properly used for manufacturing near designed shape structures for ceramic scaffolds [82, 83]. However, it is limited properties in binder properties used in the process. The selective laser melting (SLM) technique has recently gained popularity due to its ability to produce high melting point ceramic or metal.

2.5.2 Selective laser melting technique

Advanced materials offer unique properties for high-tech applications. However, these unique properties also cause a certain level of inconvenience in manufacturing such as high melting point, exceptional mechanical strength, thermal resistance and chemical stability [84]. The SLM technique was designed to use a high-power density laser focused on the metallic or ceramic powders to melt them together and the SLM process (Figure 2.12). Figure 2.12 (a) demonstrates the SLM process (AM250 metal powder bed fusion system, Renishaw plc., UK) which applied 40W focused high-power density laser with 50 μ m point distance and 110 μ s exposure time to melt 10-45 μ m

commercial pure titanium (CP-Ti) (Widnes, UK) powder in the powder bed following the designed pattern. Once the pattern has been scanned and melted, a scraper covers the sintered part with a new layer of powder ready for the next scan, as shown in Figure 2.12 (b).

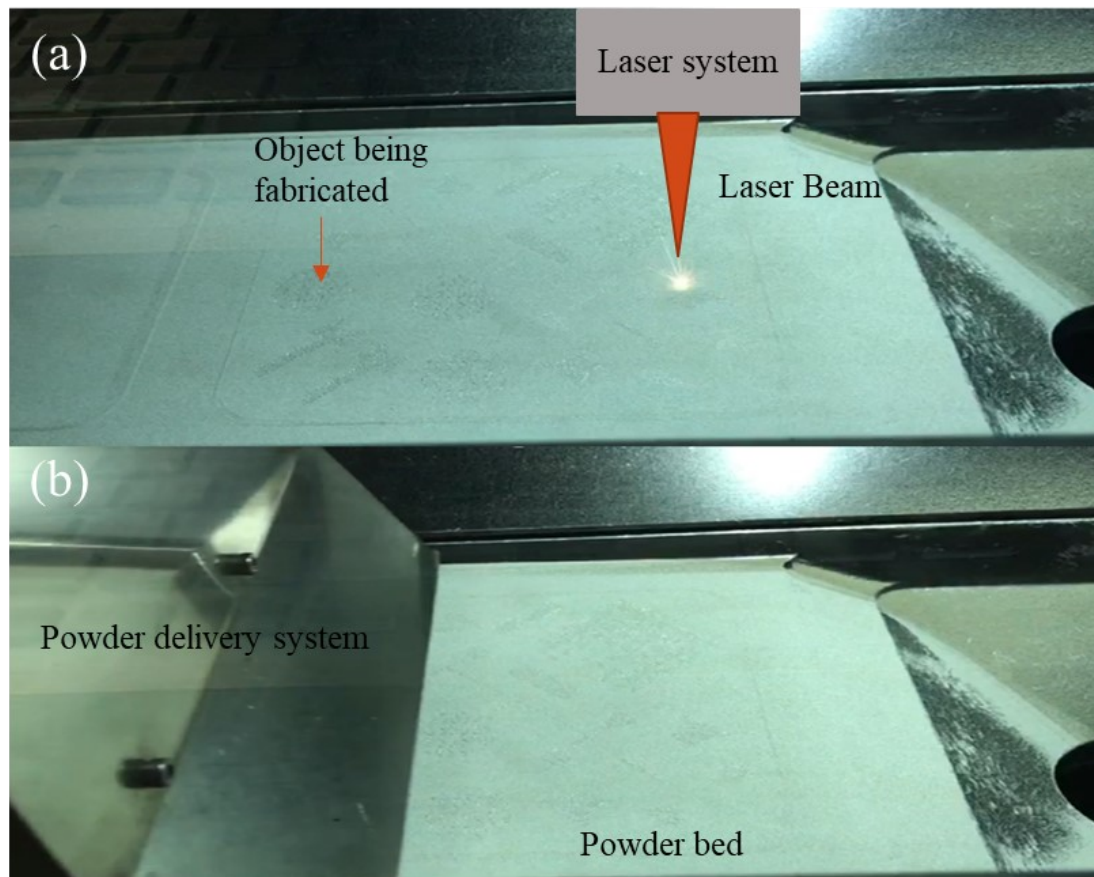


Figure 2.12 SLM process (a) is shown laser impinging on the centre powder bed where the power is melted together. The left powder bed (b) is supplying new powder and covered new layer of powder by a scraper coming from the left bed to the centre bed for next laser scanning.

The working mechanism of SLM technique is based on digital design software such as AutoCAD and Rhinoceros 6.0 (Robert McNeel & Associates, USA) to design of the built part and slice a 3D objective into 2D layer. The laser system will be applied

following the designed pattern layer by layer. The laser has a very short exposure time (about 110 μ s) which strongly limits fusion area, and the scanning depth is typically less than 100 μ m. Thus, it is the limit of the size of the powder and needs to be prepared beforehand. The centre powder bed stage will lift down once the laser pattern has been finished and the left powder supply bed stage will lift up a certain height then covers a new layer of powder by the powder delivery system. The quality of printing object strongly depends on the quality (purity, shape, particle size, particle size distribution, and printing environment) of powder also the working power on the laser and the powder bed stage.

2.6 Gyroid structure

Porous materials have been investigated for bone integration applications and titanium is a popular candidate material. It has been used in various porous forms, from shot opened to those produced by Additive Manufacturing (AM) methods, such as selective laser melting (SLM). CP-Ti tends to be produced as a bone implant scaffold. The gyroid is an interconnected porous structure that is recently designed as a bone implant scaffold due to controllable porosity and open pores. We hypothesis a gyroid structure to provide enhanced mechanical properties and integration with the hybrid structure.

2.6.1 Introduction of gyroid structure

The gyroid is a structure composed by a periodic minimal surface without self-intersection which was first published by Alan Schoen in 1970 [85]. His study mentioned how any connected graph may be embedded in an orientable surface in order to form the vertices and edges of a map. However, Schoen did not provide proof of

embeddedness in his research. Two decades later, Große-Brauckmann et al. [86] proved that gyroid is a triply periodic minimal surface in the associated family of the Schwarz P- and D- surface. Although the gyroid refers to the family of the Schwarz P surface, the gyroid exists in several families that preserve various symmetries of the surface. Similarly, these minimal surfaces appear in triply periodic minimal surfaces. Therefore, the gyroid surface can be trigonometrically approximated by the following equation:

$$\sin(x)\cos(y) + \sin(y)\cos(z) + \sin(z)\cos(x) = 0 \quad \text{Equation 2.6.1.1}$$

Because of these studies, we can simply use this equation to define the surface we need. The traditional casting techniques are not competent to prepare this infinite interconnected open porous structure. This structure can be produced using AM techniques such as SLM printing. This technique can print a complex structure directly from computer-aided design (CAD) design. (Figure 2.13) Figure 2.13 (a) and (b) demonstrate the united surface of the gyroid before and after render, showing the curvature on the rendered surface. The structure of the unit surface design can provide a very magnificent level of structural freedom. The porosity of the gyroid can be controlled by different connected angles and curvatures along the unite cell as well as the density determination is based on the thickness of unite surface. A whole gyroid structure is built by stacking different symmetry axes and the first layer of stack as shown in Figure 2.13 (c). Each layer of patterned gyroid surface must stack by a certain angle and orientation that can be consequently assembled as a gyroid unit cell as shown in Figure 2.13 (d). We can simply mirror gyroid unit cells to build an infinite interconnected gyroid. Triply periodic minimal surface demonstrates such unique geometry without self-intersection that provides biomorphic geometry as a platform to mimic the interconnected structure and controllable porosity of natural bones. The open

channels are interconnected and by controlling density, porosity and mechanical properties can potentially be similar to cortical bone and trabecular bone.

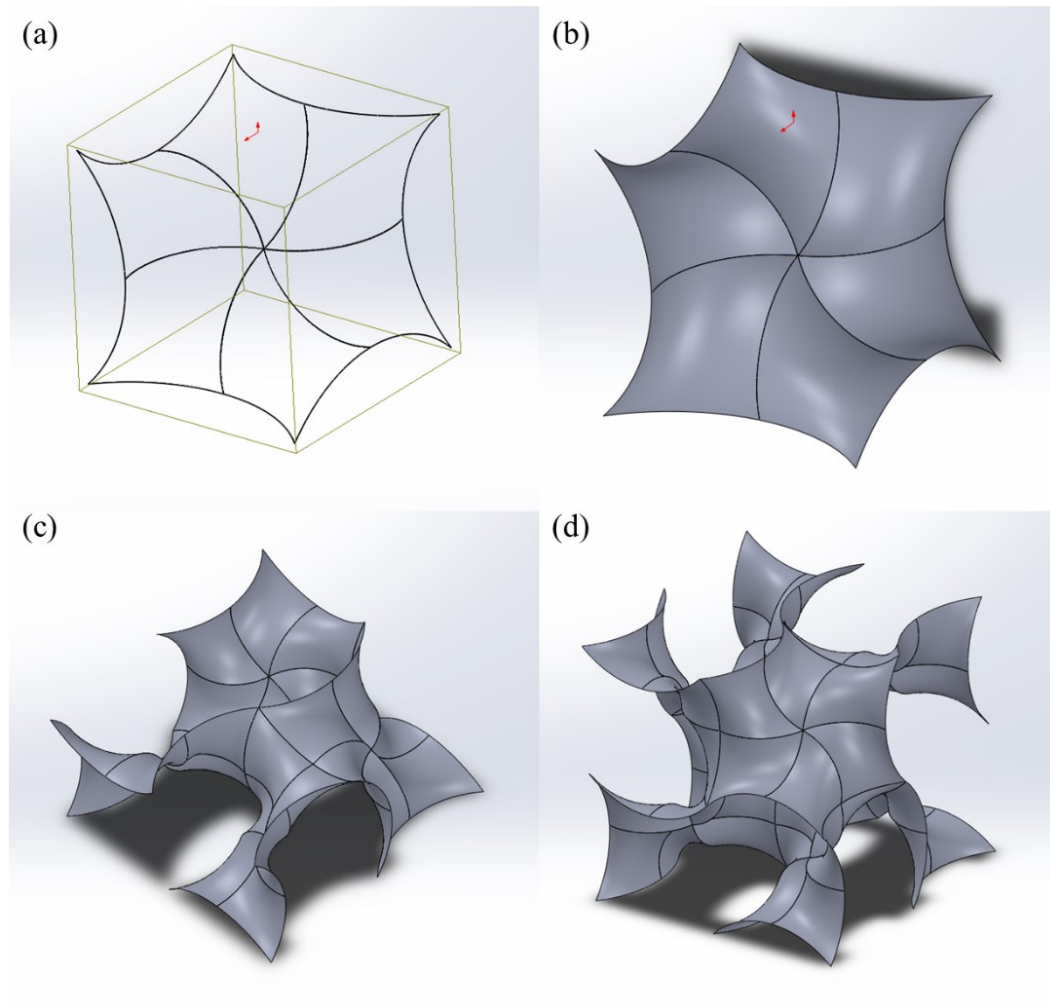


Figure 2.13 The gyroid structure designed by CAD software. (a) the unit surface of gyroid design, (b) the rendered gyroid unit surface, (c) assembly gyroid unit cell by patterning gyroid unit surface and stack with adjusting symmetry axis and (d) the gyroid unit cell. The infinite interconnected gyroid can be built by mirroring the gyroid unit cell in (d).

2.6.2 Application of gyroid structure

Gyroid structure is composed of triply periodic minimal surfaces to create a unique type of open-cell porous structure that can be mathematically defined as

$$\sin(x) \cos(y) + \sin(y) \cos(z) + \sin(z) \cos(x) = C \quad \text{Equation 2.6.2.1}$$

where C is a constant to represent the overall geometry of the surface. While $C = 0$ is represented the overall geometry of the structure is composed of a surface with two sides that split equally in 3D space into two domains to create two symmetric interconnected networks with the same volume as the simple gyroid as mentioned in the above section. On the other hand, while $C \neq 0$, the geometry of the surface is changed. The surface has been changed by different values of C , which can create unique porous distribution and different kinds of interconnected regular geometry in the gyroid. These changes have been used in applications such as electron transport, catalysis, other mechanical applications [87, 88]. Gyroid scaffolds have been made and used widely in many fields, for example, a biodegradable implant made of poly(L-lactide) (PLA) [89, 90] and other metal implants such as titanium and alloys [91]. In this section, we focus on the titanium and titanium alloys gyroid scaffold mechanical properties for bone applications. Titanium-based materials have been used in bone repair due to their excellent biocompatibility, chemical inertness and high corrosion resistance. Dense Ti-6Al-4V implants fail to match the modulus of bone compared with human bone modulus from 1.5-30 GPa to Ti-6Al-4V of about 110 GPa, causing bone resorption due to the stress shielding effect [92, 93]. Gyroid structure is a promising alternative to decrease the stiffness of dense titanium-based materials and make it as tailorable to match the modulus of the bone. In terms of conventional porous material which can tune the mechanical properties by filling space with materials, the gyroid structure can control its mechanical properties by thickening the gyroid surface [94].

This surface thickening can change the porosity and according to previous studies suggest the porous gyroid structure exhibit a comparable porosity with trabecular bone and cortical bone. Meanwhile, the modulus of titanium-based scaffolds can be controlled in a similar range to trabecular bone and cortical bone [95]. The comparison of compressive strengths of different fabrication methods to titanium-based gyroid scaffold as well as the compressive strengths of the trabecular bone and cortical bone are listed in Table 2.2. The porosity of scaffolds can be manipulated from 5% up to 95 % which are covering the porosity ranges from cortical to trabecular bone. Similarly, the compressive strengths of titanium-based scaffolds can be controlled from 5.4 MPa to 206 MPa. Titanium alloy is a very stiff material. However, the advanced AM technique means titanium alloy can be designed into a gyroid structure. This structure provides high flexibility of mechanical manipulation which allows titanium alloy suitable for bone tissue engineering application. Meanwhile, the 3D porous structure creates a favourable geometry for cell attachment and suggests a potential benefit for bone ingrowth and regeneration [96].

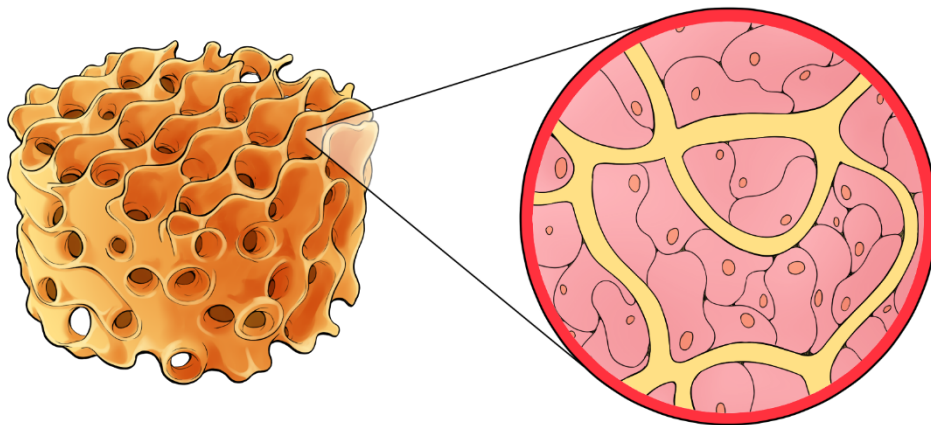
Table 2-2 Comparison of compressive strengths and moduli of porous CP-Ti and Ti alloy made by different fabrication methods compared to trabecular bone and cortical bone.

No. and material	Pore size (μm)	Porosity (%)	Compressive strength (MPa)	Modulus (GPa)	Method	ref
Ti-6Al-4V						
1	250	10.9	206	0.134	SLM	[97]
	300	11	173	0.126	SLM	
	350	11.3	163	0.113	SLM	
	400	11.2	156	0.11	SLM	
	bulk	0	1450	1.061	SLM	
2	560-1600	80-95	6.50 \pm 1.62	0.13 \pm 0.02	SLM	[95]
			81.30 \pm 2.60	1.25 \pm 0.04		
3	560-160	5-10	1342 - 1481	17.45 - 19.14	SLM	
	286.0 \pm 12.3	70.99 \pm 9.3	22.44 \pm 0.46	10.60 \pm 0.28	SLM	[98]
	372.2 \pm 23.4	71.00 \pm 9.3	18.44 \pm 0.39	8.77 \pm 0.52	SLM	
	471.6 \pm 14.5	77.21 \pm 7.0	13.43 \pm 0.24	7.80 \pm 0.23	SLM	
4	558.4 \pm 23.2	88.86 \pm 8.2	11.23 \pm 0.31	5.60 \pm 0.36	SLM	
	1300	75.66 \pm 0.31	47.45 \pm 1.34	1.91 \pm 0.12	EBM	[99]
5	1280	83.97 \pm 0.14	14.62 \pm 0.34	0.45 \pm 0.02	EBM	
	1470 - 1500	85	5.4 \pm 0.1	131 \pm 3	EBM	[100]
Cp-Ti						
1	1240 \pm 0.1	68.7	51.6 \pm 2.0	2.67 \pm 0.16	SLM	[101]
	1660 \pm 0.1	73.3	44.9 \pm 0.9	0.04	SLM	
	1910 \pm 0.1	72.4	53.3 \pm 1.2	1.46 \pm 0.03	SLM	
Trabecular bone						
			0.1 - 16	0.05 - 0.50		[97]
		up to 90	0.8 - 11.6	0.22 - 0.712		[102]
Cortical bone						
			130 - 200	7 - 30		[97]
		5 - 10	10 - 222	7.7 - 21.8		[102]

2.7 Summary and objectives

In biomedical applications, many reasons lead to composite materials failure, including inhomogeneities in their structure that result in weak interfaces between the components of the composites. Hybrid materials have the excellent structural integrity to overcome these problems. Hybrid materials have inorganic and organic networks interacting at the molecular level that produce unique mechanical properties. There is no current satisfactory solution to the problem of whole meniscus replacement which has not completely prevented cartilage degenerative changes following meniscectomy due to insufficient mechanical strength. In this study, an artificial meniscus is made using a hybrid material. The bottleneck of the artificial meniscus application is based on a lack of sufficient mechanical properties and reliable fixation techniques. The mechanical properties will be optimised by controlling hybrid compositions of THF: GPTMS ratios and comparing the mechanical properties such as compressive strength, cyclic testing, and tribological properties with living cartilage tissues. A specially designed titanium scaffold with a gyroid pore structure is incorporated with hybrid to investigate the initial stage of joining the two materials. This study is expected to provide stability for the hybrid meniscus in the early stage of implantation and mechanical pivot on fixation. To should be noted that, the biggest challenge in hybrid and titanium composite scaffold is the significant shrinkage of hybrid. Therefore, the optimisation techniques have been studied in this study in terms of controlling hybrid compositions and the manufacturing method in the drying process. Meanwhile, the systemic evaluations have been used in this study in structure/mould/scaffold design, material/chemical characterisations, mechanical tests before and after 90 days *in-vitro* tests, cell studies, and tribology tests to again bovine cartilage.

Chapter 3: Characterisation Techniques



3. Characterisation techniques

3.1 Composition characterisation

The general material characterisations and methods are described in this section and some specific methods and specific operation parameters will be mentioned in each chapter.

3.1.1 TGA/DSC

Thermogravimetric analysis (TGA)/ differential scanning calorimetry (DSC) (Netzsch Jupiter STA 449C with Proteus software) techniques are commonly used to determine the thermal properties of material. TGA analysis records the mass change of a sample under heating over the time and is used to determine the organic : inorganic ratio of the hybrid. DSC measurement detects the difference in the amount of heat required to increase the temperature of a sample and reference while TGA is running which can provide endothermic/exothermic of composite over the temperature. Thus, hybrid samples were prepared for analysis after drying and grinded in a pestle and mortar and collected 10-15 mg of hybrid powder was added to a platinum crucible. The TGA analysis was conducted from 20 to 800 °C with 10 °C min⁻¹ heating rate. The temperature raises up then the organic part of the hybrid is burnt out leaving the silica and quote silica weight percentage as the inorganic content in the hybrid.

3.1.2 FTIR

Fourier Transform Infrared Spectroscopy (FTIR) (Thermo Scientific Nicolet iS10) was used to evaluate the chemical structure of hybrid materials with an absorbance

module with 32 scans within a measurement and scan range from 400 to 4000 cm^{-1} .

3.1.3 Solution state NMR

Solution state NMR is recording proton resonances due to the tumbling of molecules in the liquid state, which means the magnetic field at the nucleus is constantly changing and so most interactions are averaged out, chemical shift peaks can give information about atoms bonded directly to protons which can be used to identify functional groups. Proton (^1H) NMR spectroscopy was used to confirm the formation of PolyTHF and the opening of the GPTMS epoxide ring before and after mixing with $\text{BF}_3 \cdot \text{OEt}_2$ catalyst, which together indicates the formation of a polymer network. ^1H NMR was carried out in CDCl_3 solvent at 400 MHz. Samples of GPTMS/THF solution were taken for NMR before and after the bubble formation and collected one drop into CDCl_3 to terminate the reaction from each time points before the solution became too viscous to collect. The analysis was done before the addition of the TEOS solution to confirm the synthesis of PolyTHF polymer and to study the relation between increase in molecular weight and bubble formation. Also, to verify which time point is more suitable for the addition of TEOS for hybrid fabrication.

3.1.4 Degradation test (PBS degradation study) and ICP studies

In order to understand the behaviours of hybrids before and after PBS degradation study in wet condition, 1 cm diameter and 1 cm of height cylinder SiO_2 -PolyTHF hybrids were immersed in PBS for the *in-vitro* dissolution. Dissolution vessels were placed in an incubating orbital shaker held at 37°C , agitated at 120 rpm. The sample weights were recorded after 60°C oven drying overnight and recorded dried weights for 0, 1, 7, 14,

60, and 90 days. The soaked PBS solutions were collected and ready for the elemental concentration measurements using a Thermo Scientific iCAP 6300 Duo inductively coupled plasma-optical emission spectrometer (ICP-OES) with an autosampler. ICP-OES gives the accurate element concentration in the dissolution solution. The plasma flame is created by argon gas and electromagnetic field and the dissolution solution feed into nebuliser then solution droplets are transferred to the plasma flame. Solutions were atomised under the plasma due to the collision with electrons and charged particles in the plasma. Thus, electrons in atomised solution are excited and emit a radiation with specific wavelength are detected by the optical emission spectroscopy. Sample concentrations are compared with the intensity of the standard solution. Silicon standards were prepared from 0 to 40 ppm. If sample concentrations were higher than 40 ppm they were diluted 10 times prior to the measurement to prevent possible precipitation in the chamber and further contamination.

3.2 Mechanical property testing

3.2.1 Compression testing

Uniaxial compression was performed using Zwick/Roell testing machine 10 kN load cell at 0.1 mm/ min compression rate under 9 N of preload to failure for compression testing. The compression testing representative curve is shown as a stress-strain curve which can record a material's response to stress. The engineering stress and strain can be calculated by Equations 3.1 and 3.2.

$$\text{Engineering stress, } \sigma_c = \frac{\text{Applied force (F)}}{\text{Crosssectional area (A)}} \quad \text{Equation 3.1}$$

$$\text{Engineering strain, } \varepsilon_c = \frac{\text{Displacement}(\Delta l)}{\text{Initial length} (l_0)} \quad \text{Equation 3.2}$$

3.2.2 Shear testing

The shear testing of the interface between the Ti and hybrid was performed by Zwick/Roell testing machine 10 kN load cell at 0.1 mm/ min shear rate under 9 N of preload to failure. A shear testing rig was designed by Solidworks that is suitable for 10-18 mm diameter cylinder samples and the screw size is M4*20mm as shown in Figure 3.1. Shear force was applied by a one-sided cutting blade (as shown in Figure 3.1 (a)) which has 1 mm of blade width to the base of the bracket (as shown in Figure 3.1 (b)) parallel to the hybrid and titanium gyroid scaffold interface (as shown in Figure 3.1 (c)). Shear bond strength can be calculated using Equation 3.1 where A is the cross-sectional area calculated by “the length of sample × 1 mm of blade width”. The strain was recorded sample diameter as initial length and calculate using Equation 3.2.

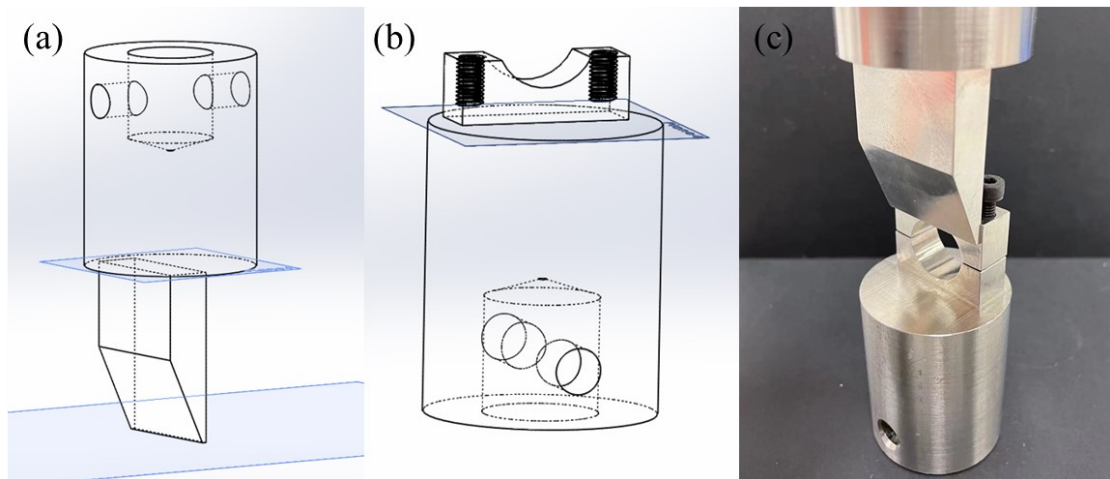


Figure 3.1 Universal shear testing rig designed by Solidworks. (a) top component is designed as a one-sided cutting blade with 1 mm of blade width and (b) bottom component is designed suitable for 10-18mm diameter of cylinder sample and the screw size is M4*20mm. Both top and bottom components have pin hold for the fixation on

the machine. (c) is computer numerical control (CNC) manufactured universal shear testing rig.

3.2.3 Cyclic testing in dry and wet conditions

Cyclic loading tests were performed using the same cyclic uniaxial compression mode by Zwick/Roell testing machine 10 kN load cell. The samples were preloaded under 9 N of preload and compression displacement was dependent on the 20% of failure strain obtained from compression testing and the cyclic rate was set as 1 Hz. For example, the compression failure strain is at 100 mm which compression path is 20% of 100 mm and times two as one cycle that path is 40 mm per cycle. One compressive cycle per second can be calculated as $40 \text{ mm} \times 60 \text{ s} = 2400 \text{ mm per minute}$. The cyclic testing was performed as received hybrid cylinder for 10^4 cycles. In order to understand the sample reliability in wet condition, the hybrid cylinders were soaked into PBS for 1, 14, 30, 60, and 90 days and samples were placed in an incubating orbital shaker held at 37°C , agitated at 120 rpm. Cyclic testing was performed at each time point on the soaked sample directly with PBS without other treatments.

3.2.4 Digital image correlation (DIC)

Digital image correlation (DIC) is an optical technique to track displacements and strains in 2D measurements. This technique is kind of dynamic mechanical analysis which is used a camera to record displacements and strains changes in images during uniaxial compression application. The images were recorded the surface pattern all the time throughout the dynamic mechanical analysis. The GOM Correlate 2018 software

was used to recognise the initial surface pattern and correlated it with the loaded pattern to determine the relative displacement of the sample pattern. The software compared the surface pattern which can be used to produce maps of the principal strain and calculate the percentage of strain and the displacement distribution. In order to obtain good quality images, the surface pattern should be high in contrast with the original surface such as a black marker on a white surface and a unique pattern label which allows a good correlation between unloaded and loaded surface determination. An ink pattern was drawn by hand on the surface of the hybrid using a blue marker to create a speckle pattern to emphasise the contrast between the surface and the pattern. A Canon 750D camera with EF-S 60 mm macro lens and 34 mm extension tubes was used, to further increase the magnification. The exposure time was 1/60 s, aperture f / 5.6 and ISO 800. The camera was set up parallelly to the uniaxial compression machine and protected by a screen from the testing rig. The compression rate is 1 mm/minute and photos were taken every 2 seconds during compression tests and testing was paused every 1 mm of displacement in order to briefly refocus the camera. ImageJ software was used to post-processed displacement photos in order to minimise other unnecessary backgrounds by cropping and stacking images. GOM correlate 2018 software was used to process the processed photos to create the surface correlation in terms of deformation pattern, distribution, and percentage of stain in a specific point.

3.3 Material observations

3.3.1 Scanning electron microscopy (SEM)

Scanning electron microscopy (SEM) is used to observe surface morphological information in this study. The SEM source generates a high-energy electron beam to bombard the surface of the sample to scatter or release several types of electrons such

as secondary electrons, Auger electrons, backscattered electrons, characteristic X-ray, etc. These electrons or signals can provide information about topography. A Zeiss Auriga Focused ion beam SEM (FIB-SEM) equipped with an EDS detector was used at 5 kV in inlens mode, with a working distance of 5-7 mm. Samples were prepared for SEM by mounting on aluminium stubs with carbon tape followed by coating with 10 nm of gold twice (Q150T sputter coated, Quorum Technologies, UK) to prevent charging of the sample. SEM was used to observe the surface of the hybrid and to image the fracture surface pattern of the hybrid.

3.3.2 X-ray micro-computer tomography (μ CT)

X-ray micro-computer tomography (μ CT) is a non-destructive X-ray microtomography scanning technique utilizing X-rays to see inside an object, slice by slice covering 360° to build up a 3D structure of an object. The μ CT detector captures a series of 2D planar X-ray images. These slices can be reconstructed into 3D models which can apply on a small object with high resolutions. The image quality is strongly affected by the material. The working principle of μ CT is that X-rays are generated and transmitted through the sample and recorded by the detector. However, there are some operational challenges in this study. Hybrid and titanium composite samples have significant density differences which affects the X-ray attenuation. This density difference may cause lower resolution and unable to clearly identify the material interface.

3.4 In-vitro testing

3.4.1 MTT assay for cytotoxicity

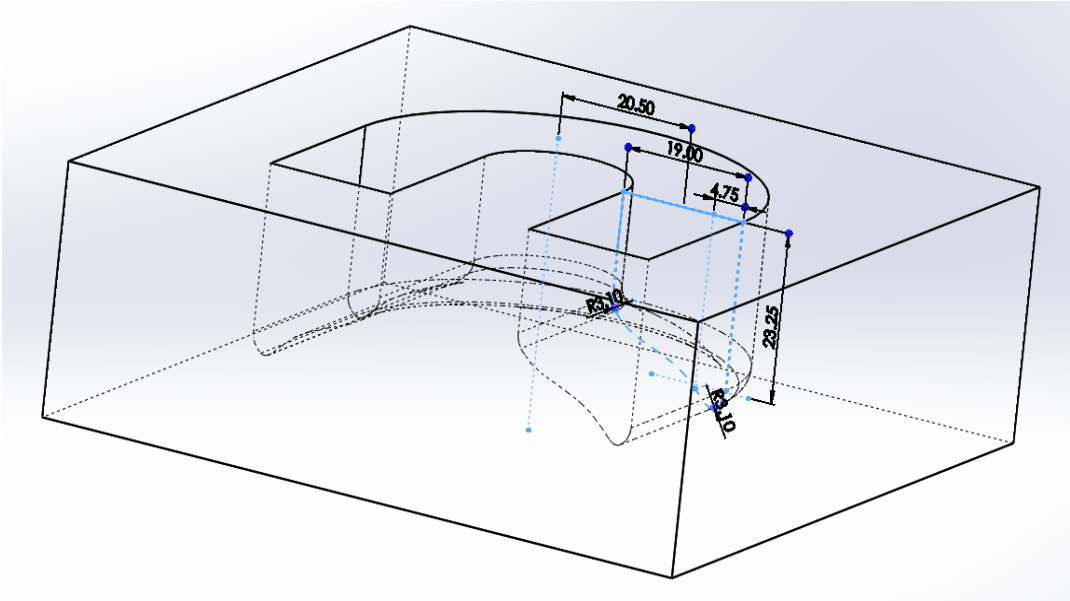
Cytotoxicity is a key index to determine if a biomaterial is suitable for *in-vivo* applications. Samples were prepared according to the ISO 10993-5 standard in order to determine any potential cytotoxicity of hybrids and scaffolds. Their dissolution products were co-cultured with Sarcoma osteogenic (Saos-2) human osteosarcoma cell line into 96-well plates (Corning, Thermosience, UK) for cell viability assay. A concentration of 5×10^4 cells/mL of Saos-2 cells was left to grow and attach in the basal alpha-minimum essential media (α -MEM) in 96-well plates for 24 h. The relationship between cell viability with dissolution products of hybrids and scaffolds was investigated using 3-[4,5-dimethylthiazol-2-yl]-2,5-diphenyl tetrazolium bromide (MTT) cell viability assays, which evaluated the activity of mitochondrial enzymes. The dissolution product of hybrids and hybrid and titanium gyroid composites were prepared in basal media. Sterilization was performed in 70% of ethanol for 30 minutes and samples were washed several times using culture media to prevent ethanol contamination. Samples were placed in an incubator shaker at 37°C, 120 rpm for 72 hours to obtain dissolution media. The dissolution product contained media was filtered through a 0.2 μ m syringe filter to sterilise and removed samples from the media, 10% foetal bovine serum (FBS) (v/v), 100 U/mL penicillin and 100 mg/mL streptomycin were supplemented [103, 104]. Separately, the culture media was removed from the Saos-2 cell line and replaced by dissolution media in an incubator shaker at 37°C, 120 rpm for 24 hours, the dissolution media was removed and cells were incubated with MTT solution (1 mg/mL in serum-free α -MEM) for 3 h. The resulting formazan derivatives were dissolved with dimethyl sulfoxide DMSO for 20 min and the optical density was determined spectrophotometrically at 570 nm using a microplate reader (Spec-traMax M2e, Molecular device). Cell metabolic activity was determined in three independent experiments in six replicates ($n = 6$). Cells cultured under the basal α - MEM were used as the positive control.

3.4.2 Cell attachment

In order to observe the cell attachment on the samples. Saos-2 cells were used for cell attachment evaluation. Samples were cut into 1 cm square size and were washed using DI water for 10 seconds for three times and soaked into 70% of ethanol for 30 minutes for sterilisation. The sterilised samples were washed in fresh α -MEM with 100 U/mL penicillin and 100 mg/mL streptomycin for three times. As prepared samples were placed into a 24-well plate (Corning, Thermoscience, UK) and concentrated Saos-2 cells were seeded to grow and attach directly on the surface of the sample in the incubator for 30 minutes at 37°C, 5% CO₂ and 21% O₂ for initial stabilisation. After 30 minutes stabilisation, culture media was added to 5 x 10⁴ cells/mL concentration and the samples were left in the incubator for 3 days. Samples were collected at day 3 and soaked into formalin waiting for the surface observation. The surface observation used SEM technique. To get high resolution images, samples should be pre-treated. Cells were fixed on the surface of samples using the gradient ethanol drying method. Samples were soaked into 50, 70, 90, and 98% of ethanol for 10 minutes, respectively. The ethanol-soaked samples were removed from 98% of ethanol and left in the fume hood and covered by tissue for air dry. The dried samples were observed the surface morphology using SEM and the rest of the steps were mentioned in Section 3.3.1.

Chapter 4

Mould design and scaffold design



4. Mould and gyroid design

4.1. Introduction of mould design

4.1.1. Mould design and challenge

The aim of this chapter was to understand the basic properties of the SiO₂-PolyTHF hybrid materials before and after casting in a mould designed to give the hybrid the shape of a meniscus. SiO₂-PolyTHF hybrid materials were originally synthesised and cast using cylindrical moulds, in order to create monoliths to understand the properties of hybrid in a simple shape. Then, more complex moulds were used to produce a meniscus. with a crescent shape (from the top-view). The shape of the meniscus in cross-section is triangular, thinner inside (avascular region) and thicker outside (vascularised region).

The objectives were to evaluate the hybrid shrinkage during drying and how it was affected by THF:GPTMS ratios. Hybrid materials have significant shrinkage during the aging and drying processes, which is a challenge for the mould casting process. The high shrinkage rate will not only increase uncertainty in the mould design but also cause shape deformation during the synthesis. The deformation is more likely to cause serious consequences such as material rupture and the designed structure cannot be formed. Therefore, the simple cylindrical hybrid was used to test the shrinkage rate of the hybrids based on changing different THF:GPTMS ratios to obtain shrinkage factors. The largest shrinkage composition was used for C-shaped menisci mould casting. The largest shrinkage composition can better fit mould design and gives more freedom for further adjustment. The comparison of two menisci moulds was evaluated in compression mechanical property and strain distribution and mechanical behaviour using digital image correlation technique.

4.2. Methods

4.2.1. Hybrid synthesis

The silica/polytetrahydrofuran (SiO₂/PolyTHF) hybrid synthesis was using two-pot synthesis that synthesis modified from previous research by Tallia et al. [105] and Dr. Gloria Young [106] in our group. The schematic experimental steps for synthesising hybrid material is shown in Figure 4.1. The inorganic SiO₂ was prepared by hydrolysis reaction from tetraethoxysilane (TEOS) in a sealed acidic environment. Separately, the organic solution was prepared by mixing THF and (3-glycidoxypropyl) trimethoxysilane (GPTMS), afterward, boron trifluoride diethyl etherate (BF₃EtO₂) was added to the THF-GPTMS solution to catalyse the polymerization in a water bath at 20°C. The inorganic solution was dropwise added into organic solution at 400 rpm until bubbles appeared, then the inorganic solution was mixed with organic solution and the hybrid solution was mixed for 10 minutes and stabilise for 10 minutes, then poured into a cylindrical mould which has 15 mm of diameter and 25 mm of height. The mould was sealed carefully in a perfluoroalkoxy (PFA) beaker and placed in at 40°C oven for aging for seven days and then either freeze drying (FD) was performed with a further seven days oven drying (OD) or only a further seven days OD (more detail synthesis optimisation in chapter 5). The effect of the ratio of THF: GPTMS on mechanical properties and shrinkage factors was investigated. According to Dr. Gloria Young unpublished results[106], 0:1 of TEOS: GPTMS ratio was too soft and 30:1 was too brittle. Thus, the 2.5:1 of TEOS:GPTMS ratio was chosen in this study. The synthesis was performed in OD and FD drying methods with molar ratios THF:GPTMS of 25:1, 50:1, 75:1, and 100:1, respectively. The hybrids were named as 25OD, 25FD, 50OD, 50FD, 75OD, 75FD, 100OD, and 100FD.

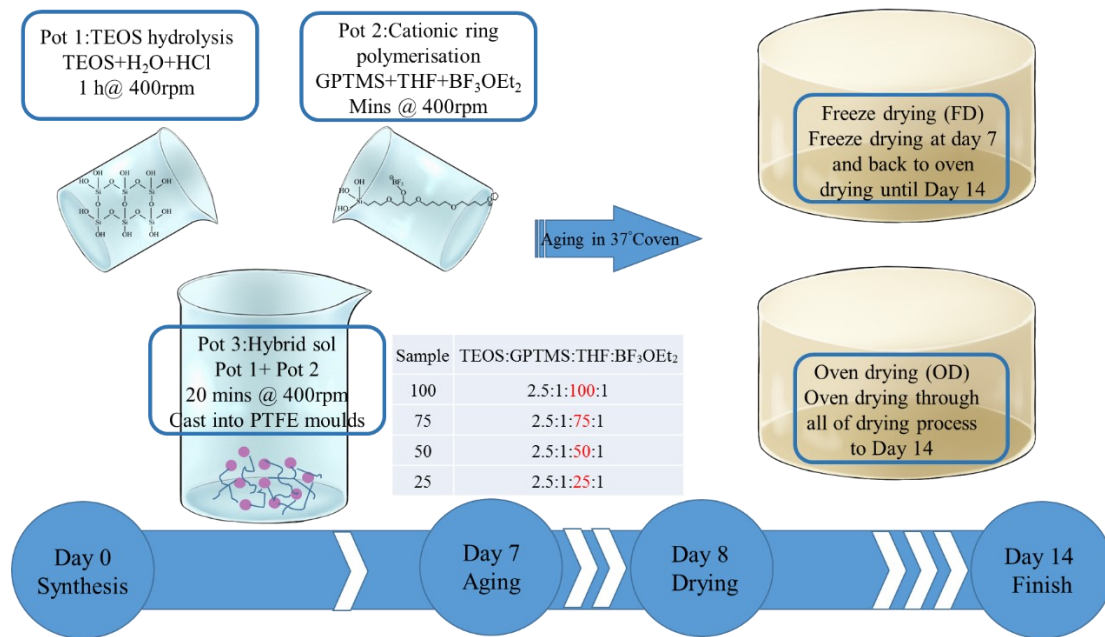


Figure 4.1 The experimental flow chart of in situ cationic ring opening polymerisation (CROP) synthesised SiO₂/PolyTHF monolithic hybrid with different compositions and different drying processes.

4.2.2. Mould casting

The preliminary design of a meniscus mould was designed and fabricated by CNC machine and was optimised in this project. The CNC machine was applied for fabricating a PTFE mould for hybrid meniscus casting although there were some limitations of the CNC machine such as it can only move in the three axes x, y and z-axis directions. Shrinkage happened in aging and drying processes. The preliminary studies were performed by 100OD hybrids. So, the aim here was to investigate how are the hybrid shrinkage to the mechanical properties and further mould optimisation.

Polytetrafluoroethylene (PTFE) was chosen for the mould material as it does not react with the hybrid solution. The meniscus shapes were designed in Solidworks into

two sections of the mould (top and bottom) and were fabricated using a CNC machine as shown in Figure 4.2 (a) and (b). The hybrid solution was left without stirring to allow the small bubbles to travel to and burst on the surface. Meanwhile, the moulds were tightened by multiple G-clamps to form a fixed mould for hybrid casting. The solution was poured into the mould via the 8 mm hole located on the top section as shown in Figure 4.2 (b) and (c). Then, mechanical force was applied to remove any bubbles trapped within hybrid solution. The mould parts were sealed by aluminium tape to prevent sudden evaporation of the solvent and placed at 40 °C oven for three days ageing and open a small hold on aluminium tape for three days that allow the solution drying completely.

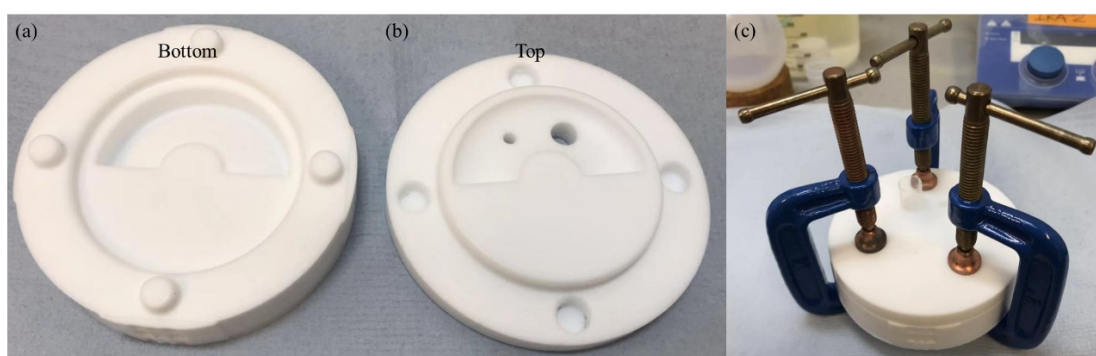


Figure 4.2 The images of PTFE mould for meniscus casting are (a) bottom and (b) top sections. (c) The moulds parts are tightened by 3 G-clamps. (Diameter of mould is 9cm)

4.2.3. *Compression testing*

Mechanical properties of hybrid meniscus are crucial parameters which act as knee stabiliser and preserve surrounding tissue. A specially produced curved platen was developed by our group for mechanical testing of the meniscus in order to apply a uniform load to the inner curvature of the hybrid meniscus (Figure 4.3). The platen was

designed with a same inner radius of meniscus mould using a CNC machine. Compression tests were performed in a dry condition without lubricant. The systematic study over a range to hybrid compositions will be investigated in this study. This testing rig was used to test optimised meniscus hybrid materials and DIC measurement.

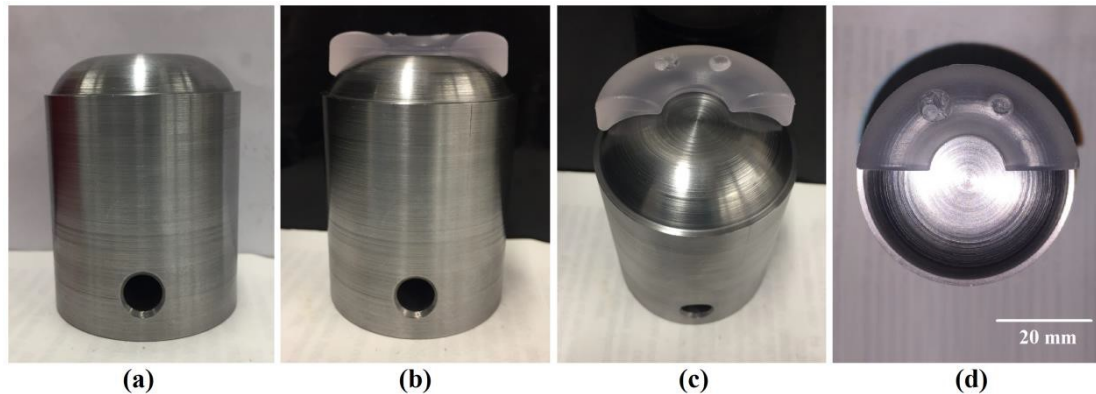


Figure 4.3 The images of (a) side view of curved steel platen, (b) side view of platen with synthetic meniscus, and (c, d) top view of platen and sample. Courtesy of S.A. Naghavi thesis [107].

4.2.4. Digital Image Correlation (DIC) measurement

To understand the effects of deformation and strain on hybrid structure, the Digital Image Correlation (DIC) technique was used as a direct measure of strain in the sample. DIC is an optical method that employs tracking and image registration techniques for accurate 2D and 3D measurements of changes in images. This method is often used to measure displacement and strains; compares strain gauges and extensometers; gathers the fine details of deformation during mechanical tests. The GOM Correlate 2018 software was used to recognise the initial surface pattern and correlated with the loaded pattern to determine the relative displacement of the sample surface pattern.

The cross-sectional area of the sample in contact with the platen of the compression rig was measured and an image captured every second of the cyclic test with an automatic shutter release. The schematic of the compression rig setup is shown in Figure 4.4.

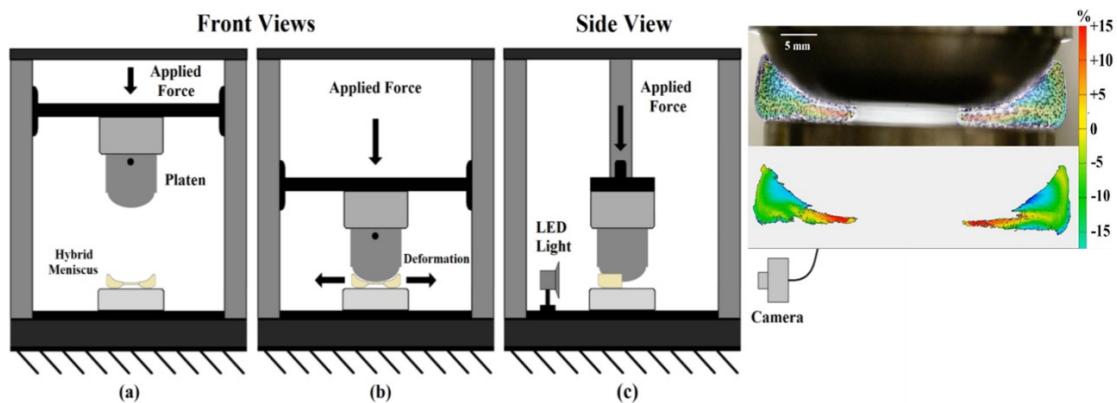


Figure 4.4 Schematic diagrams of compression rig setup (a) before applying force, (b) after applying force, and (c) side view with LED light for image quality improvement. Adapted from S.A. Naghavi unpublished research in our group [107].

4.2.5. μ CT and shrinkage measurement

Shrinkage factor determination is based on the measurement results to compare with computational results. The samples produced with hybrid material were imaged using a laboratory-based μ CT system (ZEISS Xradia 510 Versa). The X-ray source was operated at 70 kV and 75 μ A during the imaging. Captured projections were reconstructed using filtered back projection algorithm resulting in an 3D image matrix of $250 \times 256 \times 252$ with isotropic voxel size of 19.3 μ m. Hybrid samples within the 3D images were segmented to distinguish signals and noises using random forest voxel classifier (a machine learning algorithm) implemented using Ilastik software [108].

Each 3D image contained three samples with the same material composition. Each sample within the 3D images were labelled, and volume of those samples (V) were calculated using 3D imageJ suite plugin of ImageJ software [109, 110]. The volume of the mould (V_0) used to produce sample is 4417 mm^3 . The shrinkage of each sample was calculated as Equation 4.1,

$$\text{Shrinkage} = \frac{V_0 - V}{V_0} \quad \text{Equation 4.1}$$

4.3. Results and discussion

4.3.1. μ CT and shrinkage characterisation

The mixed two-pot sol was cast in PTFE cylindrical moulds with 15 mm of diameter and 25 mm height. The dried cylinder hybrids are shown in Figure 4.5. The concave top surfaces were caused by solvent evaporating during synthesis and were removed with sandpaper. To determine the shrinkage factor of samples, sample volumes were measured by the digital vernier callipers and from μ CT images for computational script calculation (Table 4.1). The measured volume shrinkages were about 78.44% up to 87.00% for all samples, which were similar to the values obtained with μ CT of 77.38% up to 87.37%, for different THF:GPTMS ratio. The computational volume shrinkage has higher accuracy compared with measurement result as it can avoid some man-made measurement errors caused by the shrunk surfaces. To note that the results of measurement in different dimensions show that the shrinkage in the diameter of the cylinder was lower than the height shrinkage. That is due to evaporation rate being higher than aging rate during aging process. The higher THF ratio of 100:1 produced significant shrinkage compared lower THF ratio samples. Meanwhile, different drying processes had less effect on the shrinkage. The μ CT scan images were reconstructed

using ImageJ software and reconstructed images are shown in Figure 4.6. Figure 4.6 (a-d) shows that the hybrids have close to cylindrical shape without obvious necking and deformation in samples 25OD to 50 FD. The samples 25OD to 50FD were treated by sandpaper to remove uneven edges. In Figure 4.6 (e-f), the upper surfaces were curved and the samples were too soft to grind. The most obvious shrinkage shows in Figure 4.6(g and h) for 100OD and 100FD, which had significant reduction in height compared with other cylindrical hybrids. The volume shrinkages were not hugely different compared with two measurements; the dimensional shrinkage can clearly demonstrate shrinkage in height from 54.72% down to 30.96%. The 100OD sample was chosen for menisci shaped mould optimisation due to highest volume shrinkage based on the computational script calculation results.

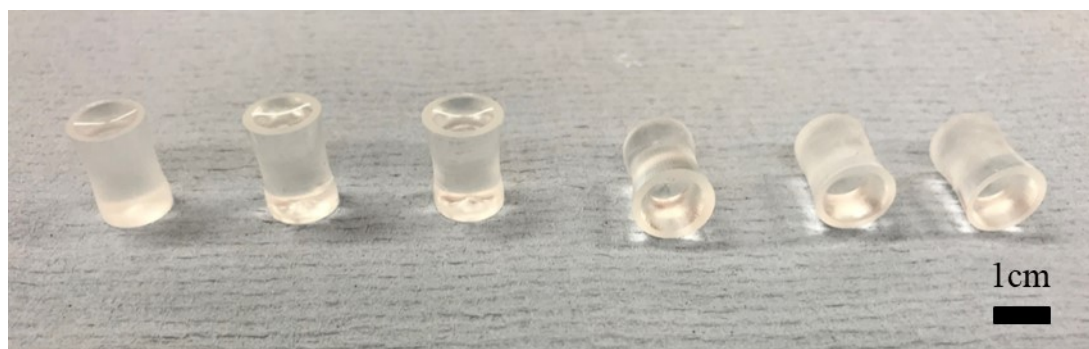


Figure 4.5 Photograph of synthesised hybrid cylinders after drying.

Table 4-1 The volume shrinkage and dimension of shrinkage as measured by calipers and from μ CT imaging (computational).

Volume shrinkage (%)	25OD	25FD	50OD	50FD
Measurement	82.02±1.23	82.01±0.69	78.44±0.20	79.51±0.14
Computational	81.23±0.73	80.85±1.52	77.38±1.25	80.50±1.20
	75OD	75FD	100OD	100FD
Measurement	81.94±0.50	80.06±1.28	87.00±0.74	86.72±0.51
Computational	79.11±0.38	78.21±0.18	87.37±3.18	85.67±1.31

Dimensional shrinkage (%)	25OD	25FD	50OD	50FD
Height	47.76±3.21	49.29±2.29	52.87±0.50	54.72±1.09
Diameter	61.35±0.06	60.42±0.49	62.26±0.43	62.77±0.47
	75OD	75FD	100OD	100FD
Height	50.52±2.35	46.85±0.40	36.40±3.40	30.96±0.99
Diameter	62.81±0.60	62.09±0.64	59.91±4.00	65.50±0.80

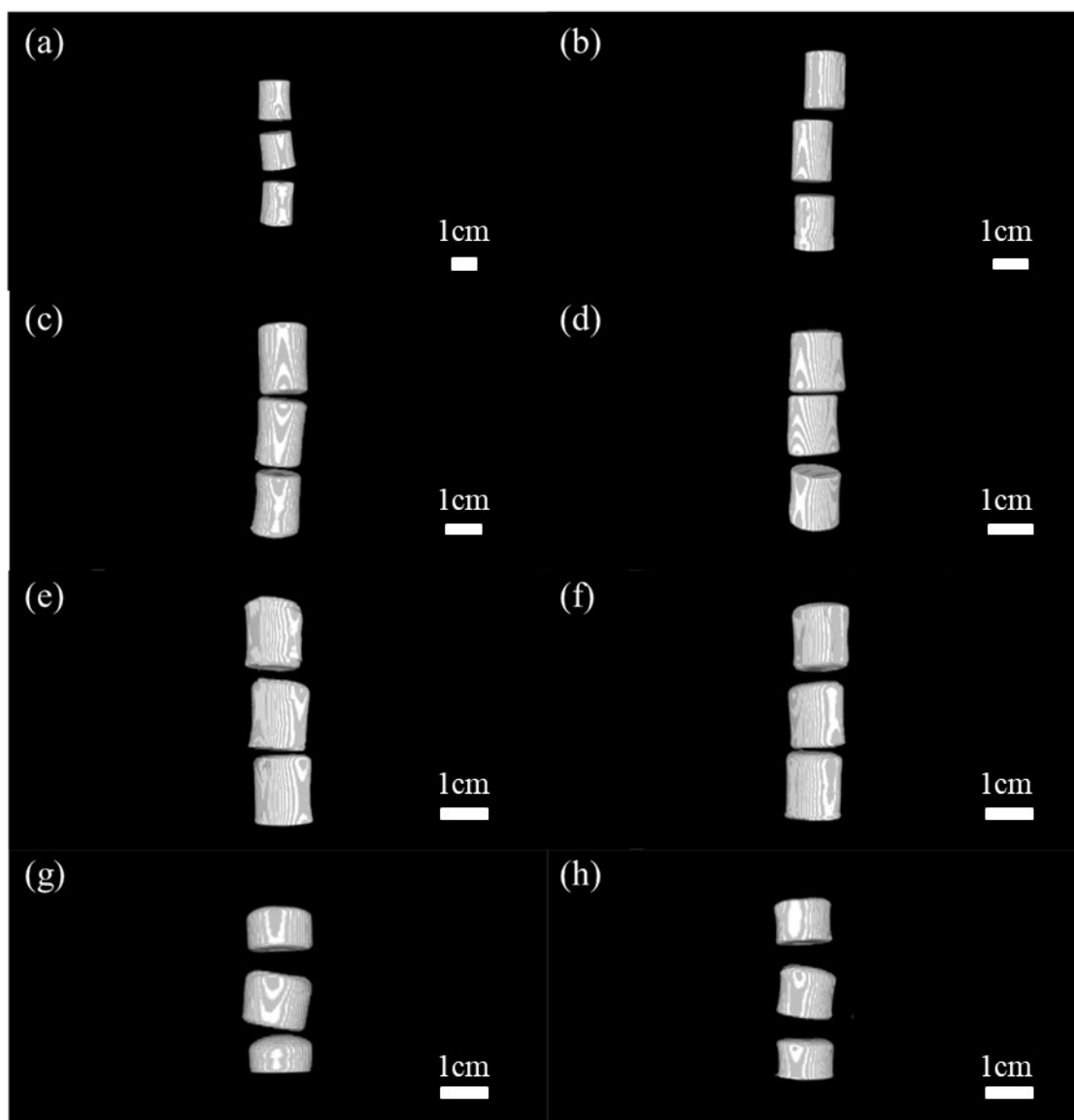


Figure 4.6 μ CT scans that illustrate the shape of (a) 25OD, (b)25FD, (c) 50OD, (d) 50FD, (e)75OD, (f)75FD, (g) 100OD, and (h) 100FD.

4.3.2. *Shrinkage factor of C-shaped meniscus hybrid*

In the case of $\text{SiO}_2/\text{PolyTHF}$ hybrid, the PolyTHF is a majority component in the hybrid synthesis. The THF has two important roles in hybrid synthesis: monomer and solvent. The PolyTHF is crosslinked THF by 3-glycidoxypolytrimethoxysilane (GPTMS) coupling agent in 100 to 1 molar ratio. Uncrosslinked THF solvent can be

removed by oven evaporation. Removal of solvent and polymerisation result in significant shrinkage while drying. Thus, the shrinkage factor of hybrid should be evaluated for meniscus mould optimisation. The shrinkage factor was evaluated by a C-shaped meniscus mould in terms of measuring the sizes of hybrid material before and after the mould casting. The shrinkage factor of hybrid material can be measured in several dimensions from A to E as shown in Figure 4.7. and values are listed in table 4.2. The average results suggest a shrinkage factor in different dimensions of approximately 0.6. This information is crucial for the meniscus mould design which the dimension of the final product can be anticipated following this factor.

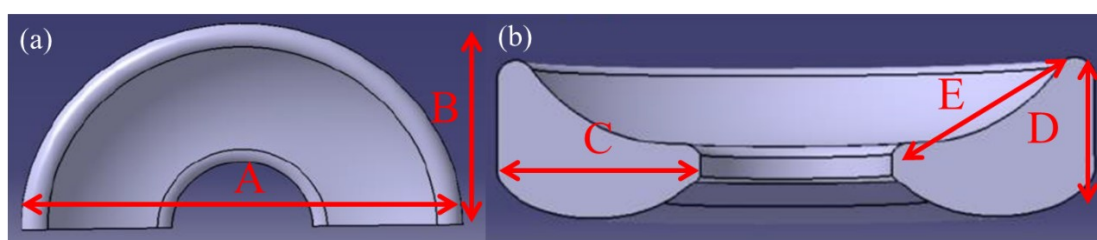


Figure 4.7 A schematic diagram of meniscus showing dimensions measured A to E (a) top view and (b) side view.

Table 4-2 The shrinkage factors of hybrid materials (1-5) in different dimension from A to E as shown in Figure 4.7.

Sample (cm)	mould	1	2	3	4	5	Shrinkage factor
A	6	3.65	3.3	3.8	3.8	3.5	0.60
B	3	1.9	1.8	1.75	1.7	1.7	0.59
C	2	1.2	1.2	1.2	1.2	1.2	0.60
D	1	0.55	0.6	0.55	0.6	0.55	0.57
E	1.4	0.9	0.9	0.9	0.9	0.9	0.64

4.3.3. Optimisation of meniscus mould

The meniscus mould design is based on two aspects. The shrinkage factor of the hybrid material can be used for anticipating the size of final product from the mould casting. The size and shape of natural meniscus can be used to design a biomimetic structure. The sizes of human medial and lateral menisci have significant individual differences. Though both menisci have a similar crescent shape, lateral menisci have been reported more circular in shape and cover a larger portion of the tibial plateau (75-93% laterally) in comparison to medial menisci (51-74% medially). Lateral menisci are approximately 32.4 mm to 35.7 mm length and 26.6 mm to 29.3 mm width [12]. According to this information, an optimised meniscus mould is designed by a Solidworks software as shown in Figure 4.8. The Figure 4.8 (a) shows a horseshoe shaped mould with 60 mm length and 58 mm width. Figure 4.8 (b) shows the thickness, width, and curvature of meniscus, respectively. Those values are based on the shrinkage factor of hybrid, dimensions of natural meniscus, and additional experimental requirements. For example, the extra thickness of mould can be preserved for further fixation design.

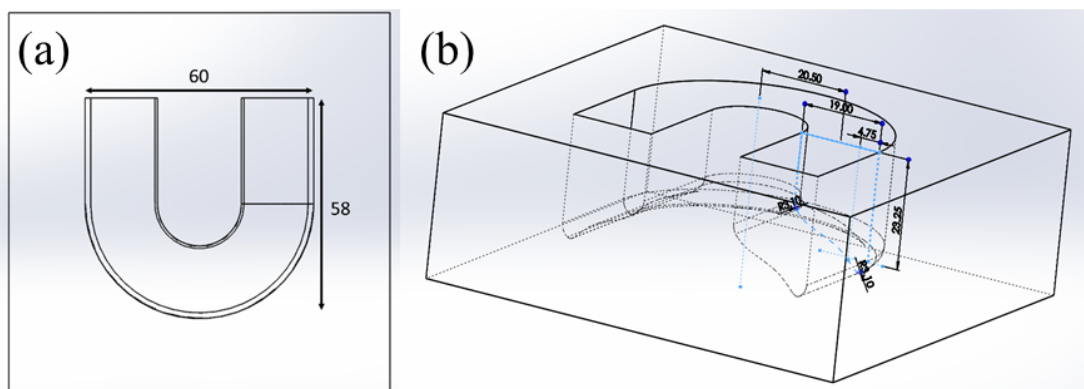


Figure 4.8 The optimised meniscus mould design (a) top view and (b) side view (units in mm).

The designed mould was manufactured using computer numerical control machining on 100 mm diameter of PTFE bulk as shown in Figure 4.9 (a). The left mould is the C-shaped mould which has a top and a bottom mould. The C-shaped mould cast hybrid is in Figure 4.9 (b) and detail casting method mentioned in chapter 4.2.2. Although the manufacturing process was trying to avoid bubbles formation, defects can still clearly be seen caused by the bubbles. These defects could be a potential risk in the application which are easy to become weak points on the structure of hybrid. On the contrary, the optimised menisci mould casted hybrid demonstrated smooth surface and structure integrity., although there is some shrinkage at the bottom. This shrinkage behaviour happened in the cylindrical hybrid synthesis. In order to further understand the optimisation of hybrid mould, the compressive strength test and DIC dynamic mechanical property test were used to compare the performances between two moulds cast hybrids.

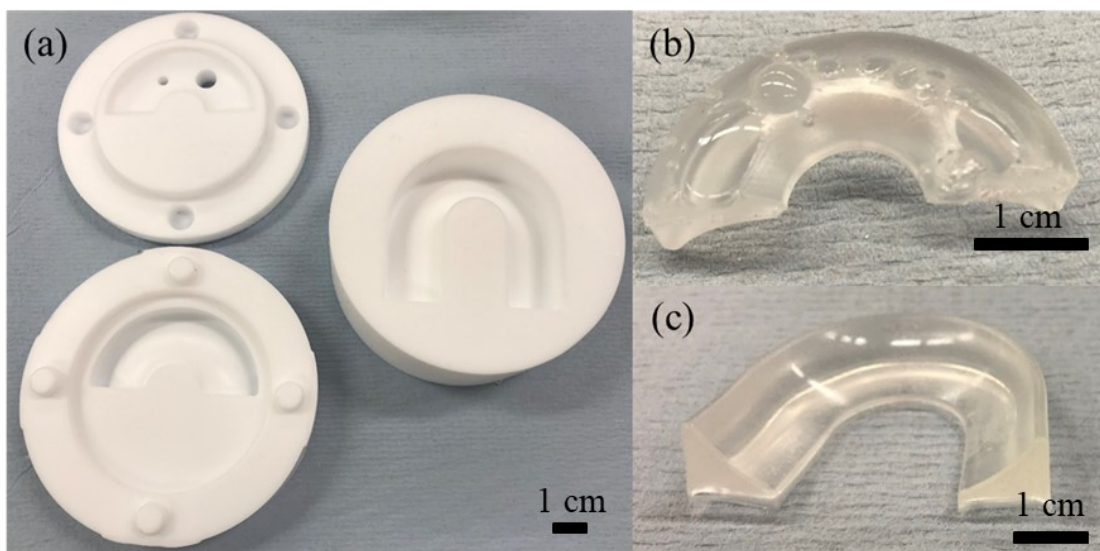


Figure 4.9 (a) Two types of hybrid meniscus moulds, (b) hybrid meniscus cast using the left mould, and (c) is hybrid meniscus cast with an improved (right) mould.

4.3.4. Mechanical properties of hybrid meniscus

To compare two mould cast hybrid menisci, a compression test was used for mechanical strength evaluation on menisci produced using old and new moulds, as shown in Figure 4.9. The compression test was performed using curved steel platen as shown in Figure 4.3. Hybrid menisci were set up along the curved platen and 9 N of preload was applied with 1 mm/min compressive rate. The hybrid meniscus cast with the first (Figure 9a, left) demonstrated serious damage while the compression test and the damaged parts focused on the surrounding region (Figure 10 (a)). The load at failure was ~4000 N standard force with 3.5 mm of displacement. By comparing with new mould cast hybrid meniscus, the new designed meniscus maintained meniscus shape without significant damaged on the bulk structure and presented a good surface for the cartilage contact area. Furthermore, the load at failure was ~10 kN with 3 mm of displacement. This result suggests that the hybrid meniscus cast in the new mould had higher mechanical strength and better structural integration under compression. The new mould simplified the step of the synthesis processes and reduced the air bubble formation, resulting in a significant improvement in mechanical properties and hybrid integration. In order to understand more about the new mould cast hybrid meniscus behaviours under compression, dynamic mechanical analysis (DMA) was used. Optical images were captured from time 0 to failure with 2 images per second shooting rate (Figure 4.10).

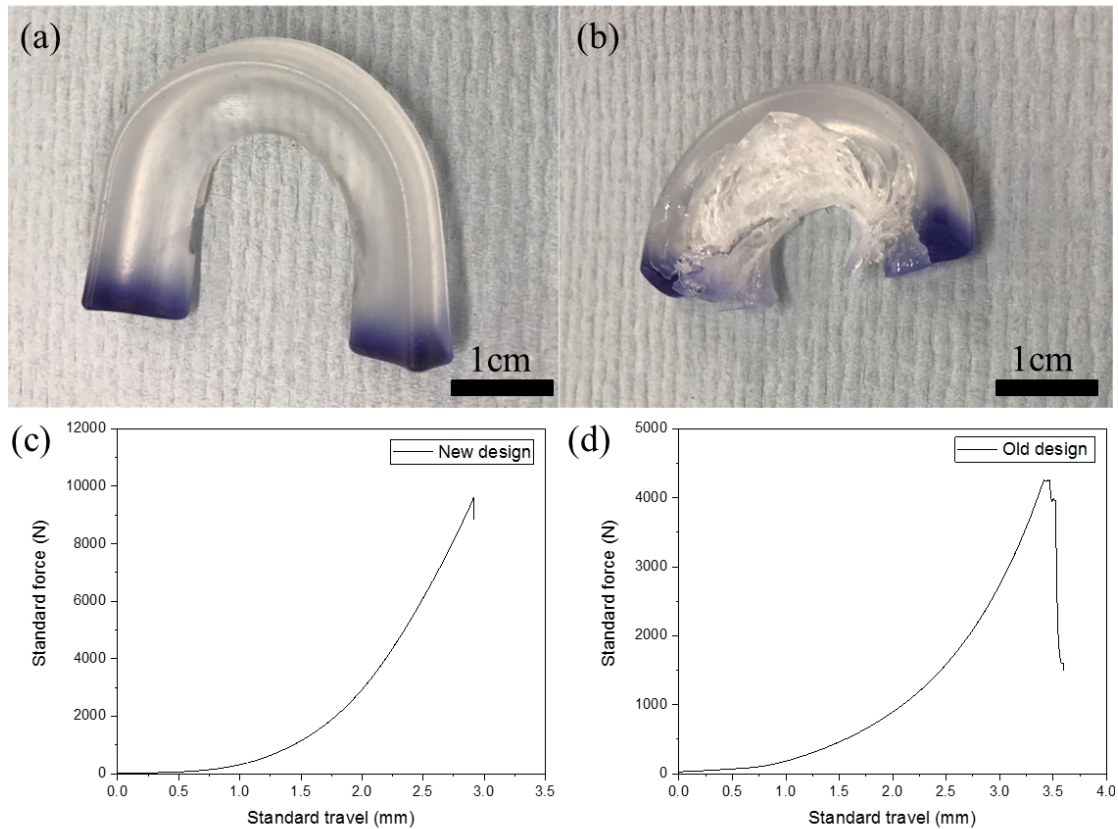


Figure 4.10 Compression testing (a) photograph of the hybrid meniscus cast in the original mould after compression testing and (b) compression test graph; compression test on (c) photograph of the hybrid meniscus cast in the improved mould after compression testing and (d) the compression test graph.

The DMA results demonstrated the hybrid meniscus deformation behaviour which was clear to observe with the contact mainly on the curve region. This is similar to natural meniscus behaviour where the inner meniscus bears higher compressive stress compared with peripheral region. The hybrid meniscus experienced a certain amount of deformation before failure but the images were not able to quantify the deformation. DIC was used to quantify the percentage of hybrid meniscus deformation as shown in Figure 4.11 based on the surface pattern changed. The surface pattern was made before the test using an ink pattern on the surface. This deformation of the pattern can be used

to represent the deformation and force distribution. The deformation patterns have been recorded from time 0 to the sample no longer to recorded.

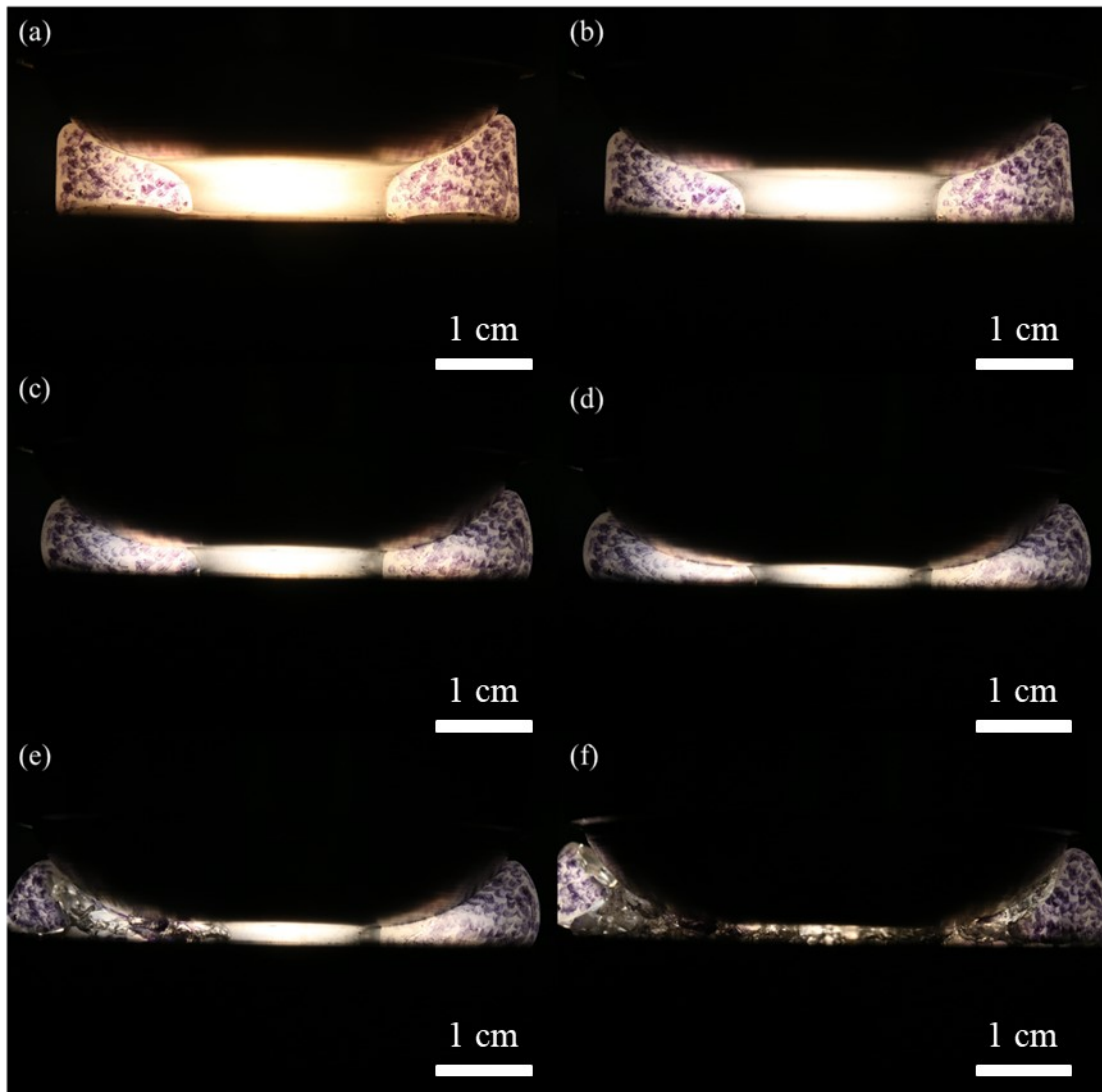


Figure 4.11 DIC results were captured in optical photographs using a canon 750D camera with EF-S 60 mm macro lens and 34 mm extension tubes which demonstrate hybrid meniscus deformation by the time as shown in (a) 0s, (b) 10s, (c) 30s, (d) 40s, (e) 50s, and (f) 55s. (An ink pattern was drawn by hand on the surface of the hybrid using a blue marker to create a speckle pattern to emphasise the contrast between the surface and the pattern.)

The DIC images show zero deformation in Figure 4.12 (a). The colour distribution

demonstrates the deformation pattern in the inner side suggest compressed state. However, the peripheral region suggests a slight stretch behaviour. At the beginning of the experiment, the samples were deformed following the stress applied direction, but after the applied pressure increased to a certain position, the samples began to move, and the test was no longer accurate. The proposed solution is discussed in the chapter 4.4.

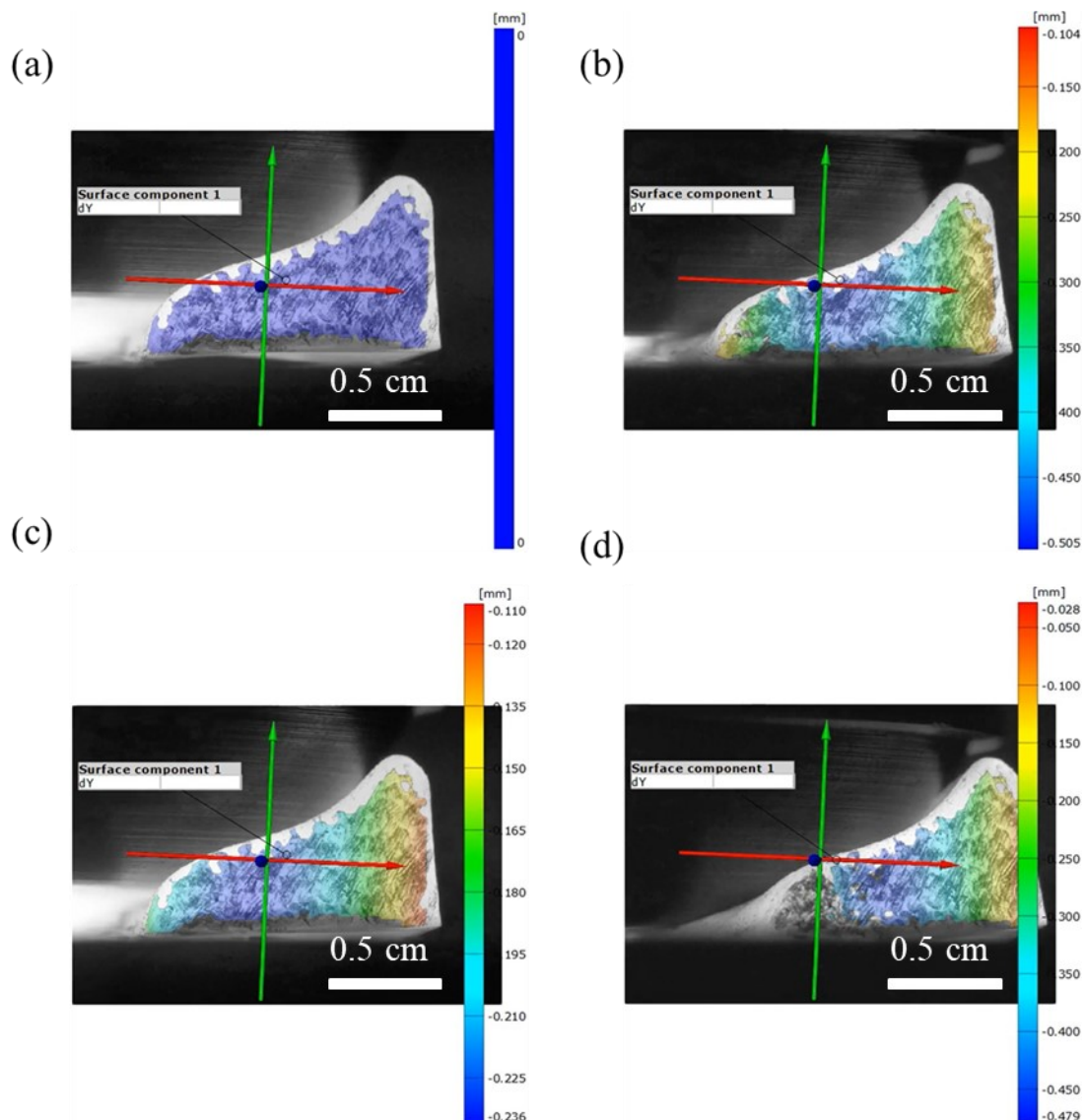


Figure 4.12 Dynamic mechanical test results were analysed using digital image correlation (DIC) technique which demonstrate hybrid meniscus deformation by the time as shown (a) 0s, (b) 10s, (c) 20s, and (d) 30s.

4.3.5. Conclusions

In this chapter, a hybrid meniscus device was successfully synthesised by mould casting. Hybrid cylinder and hybrid meniscus shrinkage factors have been evaluated using μ CT and measurement methods. These factors were used in conjunction with natural meniscus size for new mould design. The new hybrid meniscus mould produced a device with higher compressive strength and better structure integrity compared with the original castings. The deformation pattern suggested similar deformation distribution with natural meniscus. However, an unexpected sample movement happened while DMA analysis. The fixation mechanism is required and discussed in the next chapter.

4.4. Introduction of gyroid scaffold design

This chapter proposes a solution for the fixation of the moulded meniscus and completed a preliminary design for the further material combination. The solution proposed here is based on bioinspiration of the fixation mechanism of the natural meniscus, which is fixed by the peripheral muscles and the anterior and posterior cruciate ligaments (Chapter 2). The design is a combination with hybrid meniscus and porous titanium anchors. The hybrid meniscus can be used to replace the natural meniscus while the titanium anchors are designed with a gyroid structure. This anchor does not only provided an initial fixation but also the secondary biological fixation. Thus, this chapter is focused on the titanium gyroid structure design and manufacturing and an *in-vitro* cell viability test to prove that the combination of hybrid and titanium gyroid materials can be used in the further biomaterial application.

4.5. Methods

4.5.1. Solidworks gyroid scaffold design

Gyroid structure is a triply periodic minimal surface in the associated family of the Schwarz P- and D- surface described in Chapter 2.5.1. The gyroid design is founded on a star-shape simple surface and 8 of these simple surfaces are joined in one simple unit as shown in Figure 4.13 (a). The unit is established on 6 connecting points and 6 curve points which points location can be labelled using point coordinates (x,y,z). The 6 connecting points are located in (1,0,0), (1,1,0), (0,1,0), (1,0,1), (0,0,1), and (0,1,1) also the 6 curve points are located in (2/3,0,1/2), (1,1/2,1/3), (1/2,2/3,0), (1/3, 1, 1/2), (0,1/2,2/3), (1/2,1/3,1). These 6 connecting points are used to connect near connecting points which has fixed position and orate as whole unit. On the other hand, the 6 curve points can be used to control the curvature based on changing the location, which is mentioned with underline value in curve points location that range can be changed from ~0 up to 1/2. The structure porosity and pore size can be controlled by thickening the simple surface as shown in Figure 4.13 (b). In order to use the gyroid structure as a scaffold, the unit cells need to be patterned and built up to certain size (in Figure 4.13 (c)) then shaping as a cylinder scaffold (in Figure 4.13 (d))

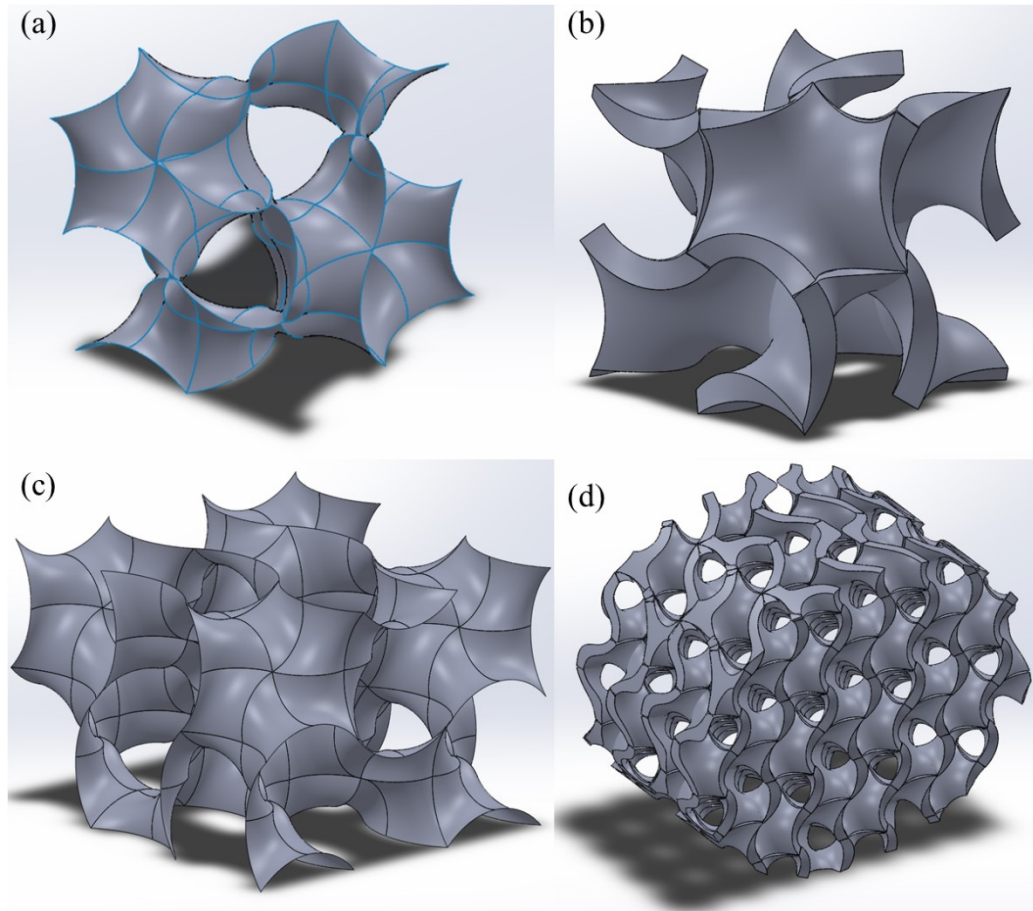


Figure 4.13 Gyroid structure designed by Solidworks software: (a) a single unit of gyroid structure which is stacked by eight star repeating units by certain angle rotation joined at specific angles; (b) demonstrates different wall thickness which can be used for controlling density and pore size; (c) patterning gyroid to build up 3D scaffold, and (d) cylindrical gyroid.

4.5.2. *Rhinoceros gyroid design*

Rhinoceros (Robert McNeel & Associates) is a design software which supports a Grasshopper function, which can install numerous plugins that can be used to build a 3D structure based on the mathematical function. The function boxes for building gyroid structure are shown in Figure 4.14. The gyroid structure can be simplified as one equation (Equation 2.5.1.1 and 2.5.2.1) and built up in 10 steps. Steps 1 is to input the

equation of gyroid to define the fundamental feature and the steps 2 and 3 are giving function and setting the range for x, y, and z values for mesh creation needed to create a simple unit of gyroid then step 4 uses Laplace smooth (using Laplace operator for imaging sharpening) and thicken function to create thicker surfaces with continuous joins. Step 5 is used to pattern the simple unit of gyroid as different sizes of cube. The Box function is a provided signal for the first cube size and the ArrBox function duplicates the number of cubes and joins them by WbJoin function, which signals the next shaping function. Another signal also comes from step 6 volume setting which provides information about the wall thickness and moves to step 7. Step 7 is the combining of information from step 5, 6 and the Brep function to create a scaffold shape in Rhinoceros that defines the scaffold bulk shape, such as cylinder. Step 8 is the final mesh smoothing to join everything as an interconnected volume and bake function (assembly) the scaffold in step 9. Rhinoceros is fast and can precisely create a scaffold in a complex architecture using multiple function and mathematic equation. Due to the structure is built by the calculation result of equation and lots of smooth and join functions which can create an excellent scaffold.

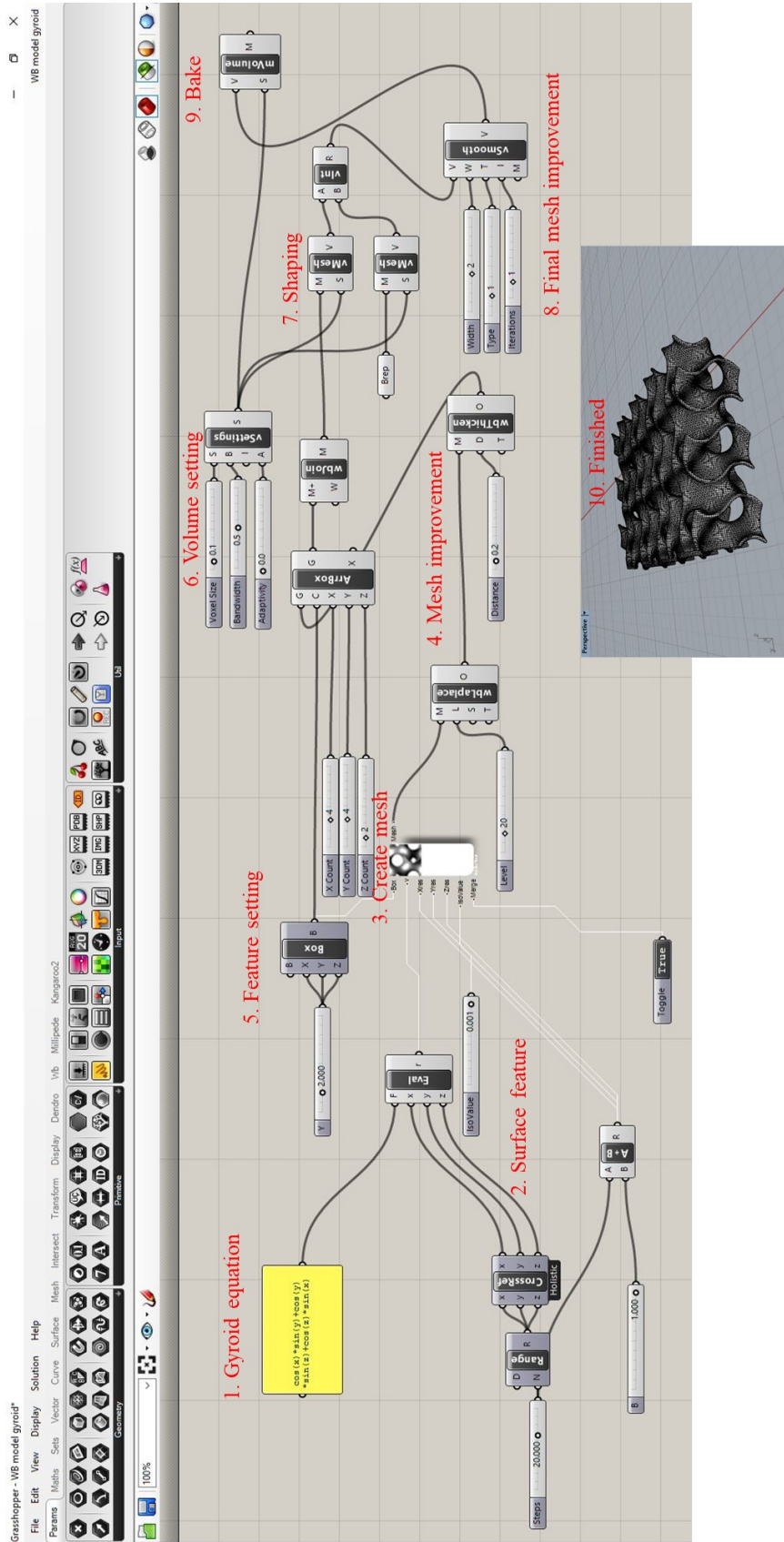


Figure 4.14 Rhinoceros is a software to design gyroid which is based on mathematic function.

4.6. Results and discussion

4.1.1. Solidworks gyroid scaffold

The Solidworks designed gyroid scaffold can be manufactured using SLM technique and the printed scaffold as shown in Figure 4.15. The manufacture details have been mentioned in chapter 2.5.2. The Solidworks gyroid scaffolds were first made with Stainless Steel 316L powder (Carpenter Additive Ltd.), spherical powder of particle size range 10-45 μm . The optical images show 3D printed gyroid scaffolds which demonstrate excellent printability and remain designed structure and porous. However, there is a disadvantage shown in the Solidworks design that is the join interface. This disadvantage is not particularly obvious when the thickness of the gyroid wall is thinner. But, when the thickness of the gyroid wall was increased, a small gap formed at the join interface and is likely to reduce mechanical strength. Therefore, Rhinoceros software was used for improved gyroid design to avoid this disadvantage.

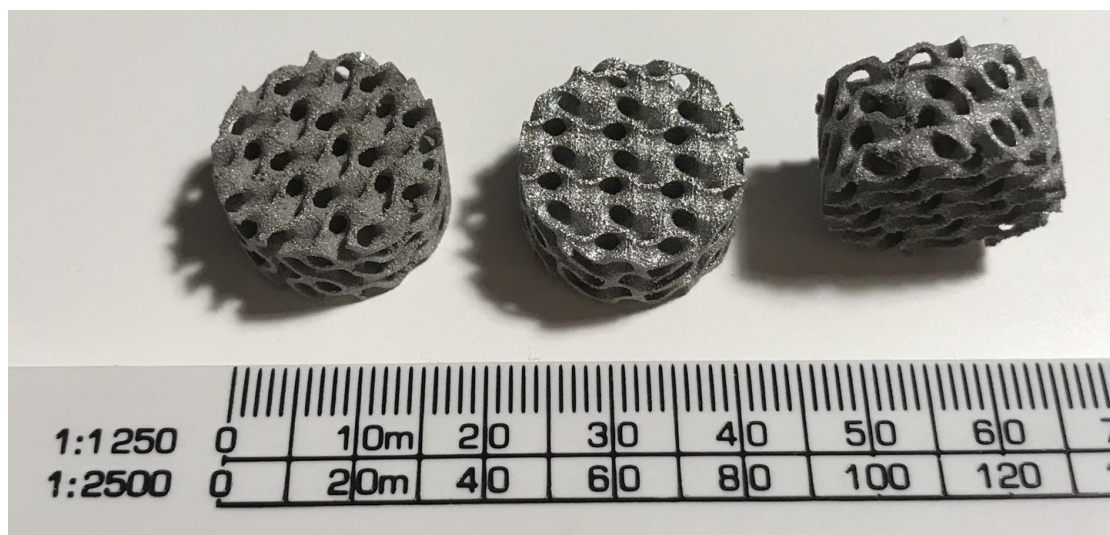


Figure 4.15 Optical images of Solidworks-designed gyroid stainless steel scaffold manufactured using SLM technique in different orientations.

4.1.2. *Rhinoceros gyroid scaffold*

The Rhinoceros-designed gyroid scaffold printed in CP-Ti by SLM are shown in Figure 4.16. Rhinoceros used various functions to avoid structure mismatch also the equation and defined parameter provide accurate printing route for the SLM machine. Thus, there is no obvious gaps on the interface and joining interface shown in Figure 4.16.

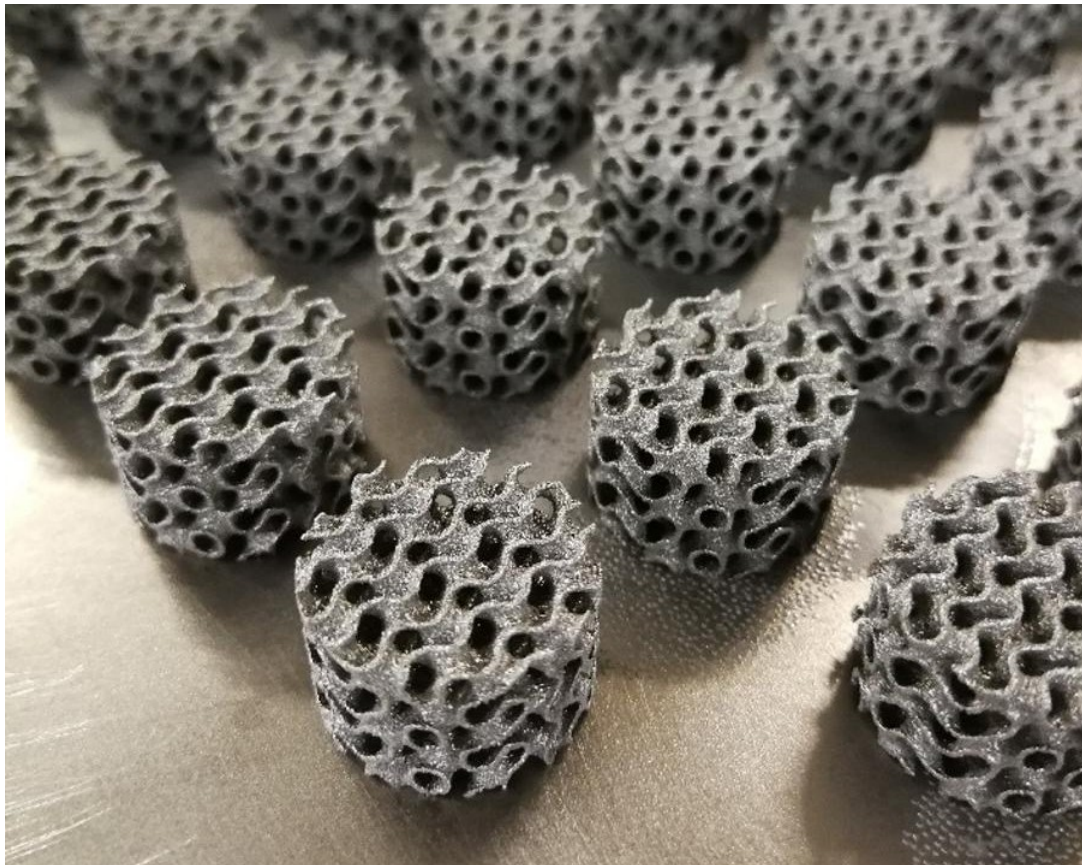


Figure 4.16 Rhinoceros-designed gyroid scaffolds printed using SLM technique using titanium material which demonstrate a great structure integration without any visible mismatch at joins. (Size of scaffold is 16 mm)

4.1.3. *Selective laser melting manufacturing*

The selective laser melting (SLM) technique and experimental methods were described in Chapter 2.6.2. The post-treatment of SLM are shown in Figure 4.17. The manufacturing mechanism of SLM is used laser to sinter scaffold layer by layer. Figure 4.17 (a) shows a scaffold covered by metal powder bed and Figure 4.17 (b) shows removal of the excess powder using brush and vacuum cleaner. In order to obtain a flat scaffold (Figure 4.17 (c and d)), a wire electrical discharge machine used a tiny copper wire as a blade to saw off samples from the manufacturing substrate. This machine can accurately cut the sample to obtain a flat surface. The flat surface can provide consistent conditions for further material manufacturing and synthesis.

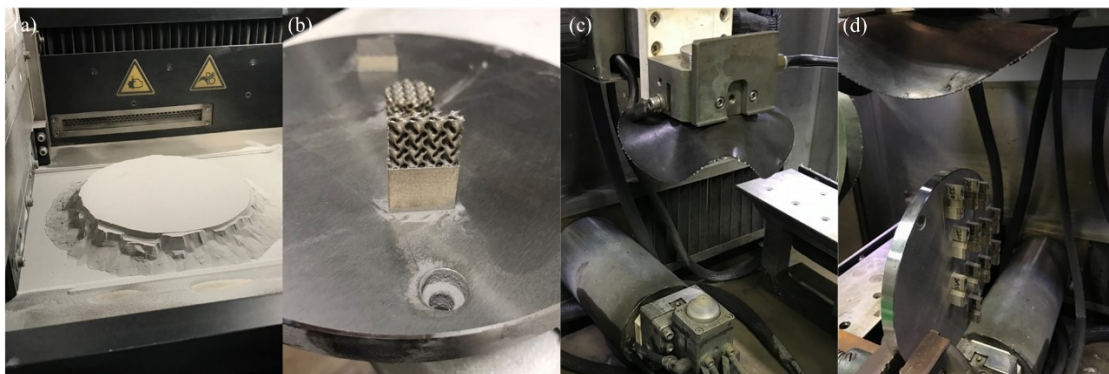
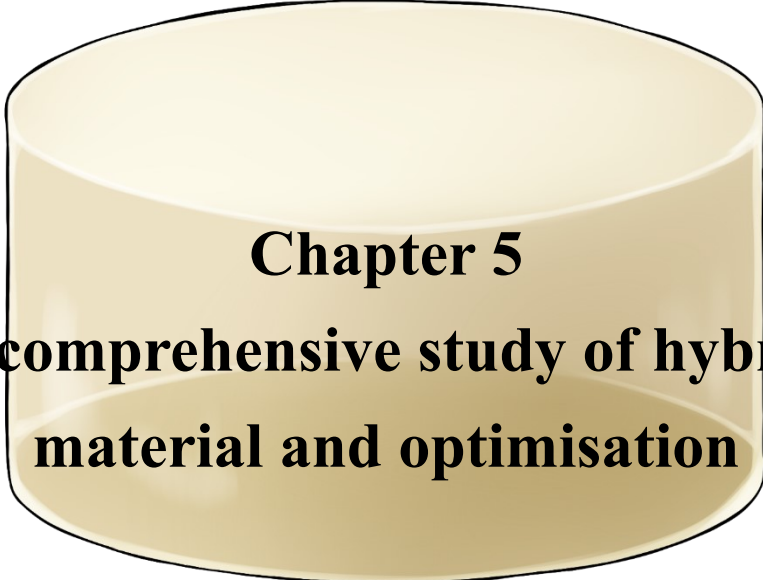


Figure 4.17 The post-treatment of printed scaffolds (a) after SLM printing samples are covered by metal powder; (b) the metal powder was removed; (c) a wire electrical discharge machine, and (d) sample and sample stage fixed on the wire electrical discharge machine for cutting along the sample substrate.

4.7. Conclusions

Gyroid scaffolds were successfully designed using Solidworks and Rhinoceros and the design optimisation has been using multiple plugins and mathematic equation. SLM manufacturing was successfully used to make gyroid structure CP-Ti scaffolds,

when they were designed in Rhinoceros software, which can be a possible solution for hybrid meniscus fixation. Gyroid can provide the possible solution for hybrid meniscus fixation and the further study on joint hybrid and gyroid scaffold is required and the hybrid and gyroid scaffold synthesis and evaluation is mentioned in chapter 6.



Chapter 5
**A comprehensive study of hybrid
material and optimisation**

5. A comprehensive study of hybrid material and optimisation

5.1. Introduction

Hybrid materials are distinguished from other traditional composite materials in that the inorganic and organic networks interact at the molecular scale. Hybrids co-networks can be bonded using coupling agents [111, 112], inheriting the advantages from inorganic and organic moieties simultaneously [113]. Therefore, inorganic and organic hybrid has received attention and want to find out more applications on this material.

Cracks are common issues during the silica-based hybrid synthesis, especially happen during the drying process. This is the main reason why the application of hybrid has tended to be as devices of small dimensions, such as coatings [121]. There are several possible reactions that cause crack formation during the hybrid synthesis. For example, phase separation of solvent and reactant, sol-gel transition, and gelation processes. Phase separation can be affected by solvent polarity, wherein reactants could have different mixability in different solvents. Organic content plays an important role for regulating phase separation rate. For instance, a higher organic concentration can slow phase separation which can provide a better homogeneous polymerisation environment. Therefore, gelation would be dominated in the initial polymerisation step rather than phase separation [119]. If the organic concentration is decreased, phase separation proceeds faster resulting in more inorganic (silica skeleton) network formation, as seen for triblock copolymer surfactants [124, 125] and hexadecyltrimethylammonium bromide that have been employed to suppress phase separation [117]. Other factors include gelation temperature and catalyst concentration.

Tallia et al. [105] discovered a combination of sol-gel and an *in situ* cationic ring opening polymerisation (CROP) to synthesise silica/poly(tetrahydrofuran)/poly(ϵ -

caprolactone) (SiO₂/PolyTHF/PCL-diCOOH) hybrid materials which demonstrated excellent mechanical properties, elastomeric behaviour and intrinsic autonomous self-healing ability. This combination of sol-gel and *in-situ* CROP synthesis technique brings huge benefit for crack-free synthesis. GPTMS was used as coupling agent to bridge inorganic (hydrolysed TEOS as SiO₂) and organic (PolyTHF) moieties. The siloxane groups of GPTMS were used to connect with silica sol (hydrolysed TEOS) [126] and the epoxide ring of the GPTMS also acted as an initiator for THF polymerisation, resulting in *in situ* CROP to PolyTHF [105].

Here, a comprehensive study focused on how to synthesise crack-free large monolithic hybrids and improve reproducibility, and to investigate its properties over 90 days *in-vitro* test. Different drying processes were evaluated to observe the phase separation, surface and fracture surface morphologies and systematic mechanical tests.

5.2. Materials and methods

5.2.1. Materials

All chemicals were purchased from Sigma Aldrich (Dorset, UK). Tetrahydrofuran (THF), (3-glycidoxypropyl) trimethoxysilane (GPTMS), boron trifluoride-diethyl ether (BF₃ · OEt₂), tetraethylorthosilicate (TEOS), HCl, phosphate buffered saline (PBS) solution were used directly without further purification.

5.2.2. Hybrid synthesis

Two-pot synthesis was used to prepare SiO₂-PolyTHF hybrids following the

method outlined in Dr. Gloria Young's thesis[106]. The synthesis is based on controlling molar ratios of organic component which are listed in Table 5.1. The inorganic pot was prepared 1 hour before the organic pot. The inorganic pot was prepared by hydrolysis of TEOS in 1 M HCl and deionised water with 1:3 vol% ratio, stirring at 400 rpm for at least 1 hour. During mixing of the inorganic solution, the solution went from phase separation to a homogeneous clear solution. The organic pot was THF mixed with GPTMS at 400 rpm for at least 15 minutes with molar ratios THF:GPTMS of 25:1, 50:1, 75:1, and 100:1 in a sealed PFA beaker. This mixing is to make sure the organic solution mixes properly before the next reaction. The *in-situ* CROP of THF monomer was initiated by the addition of $\text{BF}_3 \cdot \text{OEt}_2$ catalyst. The polymerisation was observed by visible bubbles formation after few minutes of mixing. Subsequently, the hydrolysed TEOS solution was added dropwise into the organic pot for continued stirring at 400 rpm for a minimum of 10 minutes and then left to stand without stirring for 10 minutes to allow bubbles escaped from the solution. The mixing times were recorded as part of optimisation as the *in-situ* CROP was quenched when the TEOS solution was added.

Table 5-1 Hybrid synthesis reagent quantities where A refers to the moles of GPTMS and B refers to the moles of TEOS. The organic ratios was controlled by the THF/GPTMS ratio which are from 25:1 to 100:1.

Reagent	Molar ratio
GPTMS	A
$\text{BF}_3 \cdot \text{OEt}_2$	0.25A
THF	25A, 50A, 75A, 100A
TEOS	B= 2.5A
H_2O	C= 3A+4B
HCl (1M)	1/3 volume of C

PTFE moulds were used for cylinder hybrid preparation. The inorganic and organic solutions were poured into the moulds which were 15 mm in diameter and 25 mm in height. The mould were placed and sealed inside poly(methyl pentene) (PMP) pots, double sealed by Parafilm and placed in an oven at 40 °C for 7 days. The first 7 days was the ageing time, which ensures the polymerisation and prevents THF evaporation possible. At day 7, two different drying processes were applied. For oven drying samples, lids were opened gradually over a period of rest 7 days to prevent sudden evaporation of THF and then the samples were allowed to dry in open moulds and ready to do further tests. The alternative drying method was freeze-drying, where samples were put into a -80 °C freezer for at least 4 hours to freeze samples and then the lid was opened for freeze-drying (CoolSafe 4-15L Freeze Dryers, LaboGene, UK) at -93 °C overnight. After freeze-drying process, the freeze-dried samples were allowed to reach room temperature and placed back to the 40 °C oven, the rest of steps are the same with oven drying condition. Samples are named as molecular ratio of THF:GPTMS and the drying methods which are 25OD, 25FD, 50OD, 50FD, 75OD, 75FD, 100OD, and 100FD.

5.2.3. *Solution state NMR*

Proton nuclear magnetic resonance (NMR) spectroscopy was used to confirm the formation of PolyTHF and the opening of the GPTMS epoxide ring before and after mixed with $\text{BF}_3 \cdot \text{OEt}_2$ catalyst, which together indicate the formation of a polymer network. ^1H NMR was carried out in CDCl_3 solvent at 400 MHz. Samples of GPTMS/THF solution were taken for NMR before and after the bubble formation and collected one drop into CDCl_3 to terminate the reaction from each time points before the solution becoming too viscous to collect. The analysis was done before the addition

of the TEOS solution to confirm the synthesis of PolyTHF polymer and to study the relation between increase in molecular weight and bubble formation. Also, to verify which time point is more suitable for the addition of TEOS for hybrid fabrication.

5.2.4. μ CT and shrinkage factor determination

Shrinkage factor determination was based on the measurement results to compare with computational results. The samples produced with hybrid material were imaged using a laboratory-based μ CT system (ZEISS Xradia 510 Versa). The X-ray source was operated at 70 kV and 75 μ A during the imaging. Captured projections were reconstructed using filtered back projection algorithm resulting in an 3D image matrix of $250 \times 256 \times 252$ with isotropic voxel size of 19.3 μ m. Hybrid samples within the 3D images were segmented using random forest voxel classifier (a machine learning algorithm) implemented using Ilastik software [108]. Each material composition was scanned three repetitions. Each sample within the 3D images were labelled, and volume of those samples (V) were calculated using 3D imageJ suite plugin of ImageJ software [109, 110]. The volume of the mould (V_0) used to produce sample is 4417.86 mm³. The shrinkage of each sample was calculated as Equation 5.1,

$$\text{Shrinkage} = \frac{V_0 - V}{V_0} \quad \text{Equation 5.1}$$

5.2.5. Characterisation techniques

The inorganic content was measured using Thermogravimetric analysis (TGA) on on Netzsch Jupiter STA 449C with Proteus software. Hybrid samples were prepared for analysis after drying and grinded in a pestle and mortar was collected 10-15 mg of

hybrid powder and added to a platinum crucible. The TGA analysis was conducted from 20 °C to 800 °C with 10 °C min⁻¹ heating rate. The temperature rises (exothermic) when the organic part of hybrid is burnt out leaving the silica and quote silica weight percentage as the inorganic content in the hybrid. Fourier Transform Infrared Spectroscopy (FTIR) (Thermo Scientific Nicolet iS10) was used to evaluate the chemical structure of hybrid materials with an absorbance module with 32 scans and scan range from 400 to 4000 cm⁻¹. Uniaxial compression and cyclic loading tests were performed using Zwick/Roell testing machine 10 kN load cell at 0.1 mm/ min compression rate to failure for compression test and 20% of deformation to failure for cyclic loading test. For long-term sample stability testing, all samples were soaked into PBS for 0, 1,7, 14, 60 and 90 days, respectively and recorded cyclic loading test at every time points. All mechanical testing were performed under 9 N preload. A Zeiss Auriga FIB-SEM equipped with an EDS detector was used at 5 kV in inlens mode, with working distance of 5-10 mm. Samples were prepared for SEM by mounting on aluminium stubs with carbon tape followed by coating with 10 nm of gold twice (Q150T sputter coated, Quorum Technologies, UK) to prevent charging of the sample.

5.2.6. Dissolution study and ICP

In order to understand the behaviours of hybrids before and after in wet conditions, SiO₂-PolyTHF hybrids were immersed in PBS for in-vitro dissolution. For detail experiment method has been mentioned in chapter 3.1.4. The soaked PBS solutions were collected and ready for the elemental concentrations measure. The concentration measurement was conducted using a Thermo Scientific iCAP 6300 Duo inductively coupled plasma-optical emission spectrometer (ICP-OES) with an auto sampler.

5.3. Results and discussion

5.3.1. Systematic optimisation of hybrid synthesis

The hybrid synthesis is using two-pot synthesis method. Once the two pot are mixed a gelation reaction forms a highly viscosity hybrid solution. However, before mixing, there will be some reactions in both pots: hydrolysis in the inorganic pot, which is relatively stable and consistent; *in-situ* CROP of organic moiety in the organic pot, making mixing time critical. Due to presence of PolyTHF in the material, THF could not be used as a solvent for any measurement technique. Thus, the solution state NMR was used to focus on the organic part to know the molecular weight formation during *in-situ* CROP at different time points. The solution state NMR data are shown in Figure 5.1. The spectrum in Figure 5.1 (a) is from the organic pot which contained THF and GPTMS without added catalyst. The labelling represents the proton resonances at specific site of GPTMS chemical structure (inset).

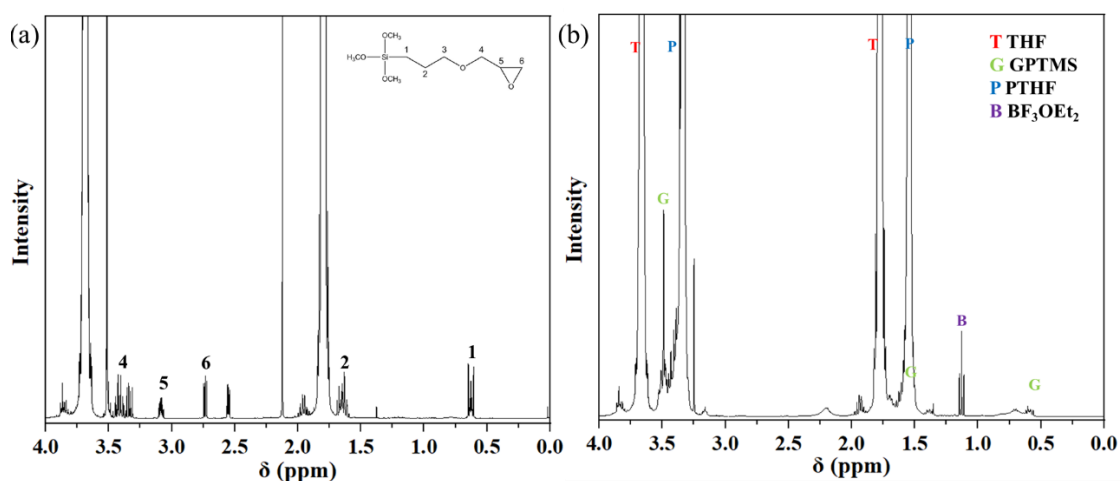


Figure 5.1 Solution ¹H NMR data of (a) mixing THF and GPTMS for 15 minutes without added BF₃ · OEt₂ catalyst with the GPTMS chemical structure labelled the representative proton resonance sites to the NMR peaks (inset); (b) is the result of mixed THF and GPTMS after adding the BF₃ · OEt₂ catalyst for 3 minutes and 45

seconds. The molecular weight calculations were calculated using integration of the area under the GPTMS characteristic peak at 0.58 ppm and PolyTHF characteristic peak at 1.54 ppm.

In ^1H NMR spectroscopy, the area under each resonance signal is proportional to the molar concentration of the protons being analysed [127]. The molecular weight (M_n) can be calculated using following Equation 5.2:

$$M_n = I_{GPTMS} + N \times MW_{THF} \quad \text{Equation 5.2}$$

Where I_{GPTMS} is the molecular weight of GPTMS initiator and N is number of repeating unites of THF and MW_{THF} is the molecular weight of THF. Figure 5.1 (b) is the result of mixed THF and GPTMS after adding the $\text{BF}_3 \cdot \text{OEt}_2$ catalyst for 3 minutes and 45 seconds. In order to calculate the molecular weight of organic, the peak at $\delta = 0.58$ ppm was selected as the GPTMS identical peak and calculate the peak area as end group to compare with the first THF representative peak at $\delta = 1.54$ ppm. So, the repeating unit of THF can be calculated as Equation 5.3 [127, 128]:

$$\frac{\text{Peak area of repeating units}}{\text{Number of protons in repeating units}} = \frac{\text{Peak area of end groups}}{\text{Number of protons in end groups}} \quad \text{Equation 5.3}$$

Once the number of repeating units were obtained, based on Equation 5.3, The results can be used in Equation 5.2 to obtain the final molecular weight. The calculation results suggested the number of repeating units in the chains after 3 minutes and 45 seconds polymerisation was 921 and the molecular weight was 66649 g/mol. MW is plotted against Time in Figure 5.2. The time point for this experiment starts from 0

seconds to 5 minutes after the catalyst was added and the whole solution appears completely clean and transparent at beginning. As time reaches 2 minutes and 20 seconds, small bubbles begin to form and more and more by the time, after 3 minutes and 10 seconds, the number of bubbles has filled the entire solution until after 5 minutes the solution with incredibly viscosity and unable to do the sample collection. The best mixing two-pot timing was really short from the bubble formation to highly viscous solution formation.

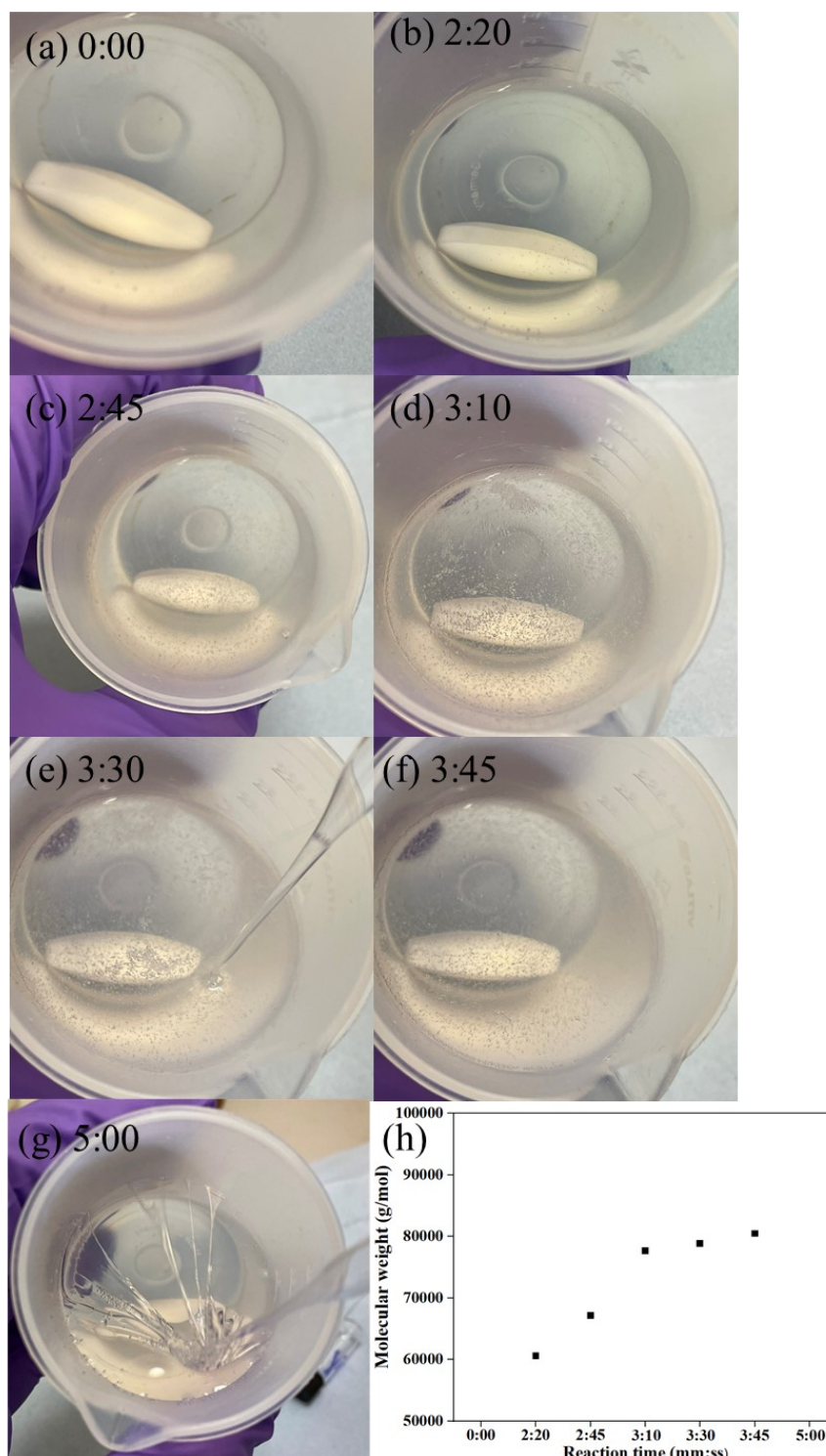


Figure 5.2 Molecular weight determination of organic moiety by recording time points for adding $\text{BF}_3 \cdot \text{OEt}_2$ catalyst to initiate the in-situ CROP for (a) 0:00, (b) 2:20, (c) 2:45, (d) 3:10, (e) 3:30, (f) 3:45, and (g) 5:00 (minutes: seconds). The solution was too viscous to do the test after 5 minutes mixing. The Mw data against time points is shown in (h).

In order to fully understand the factors of hybrid synthesis, the time at which the pots were mixed was recorded (Figure 5.3) along with photographs of sample morphology. The synthesis optimisation was based on the mixing time and the composition of THF:GPTMS molecular ratio which are from 100:1 to 25:1. The recorded results suggest high success rate in the lower THF:GPTMS ratios of 50:1 and 25:1. The success synthesis is shown as homogeneous cylindrical shape hybrid; the unsuccessful synthesis is shown as irregular semi-cylindrical shape and hollow cylinders. Refer to the table below, the temperature and humidity do not suggest significant impact in the optimisation. The combination of bubble observation and polymerisation time point are quite reliable to determine the two-pot mixing time point for the hybrid synthesis due to high successful rate at THF:GPTMS ratio at 50:1 and 25:1.

Batch/sample	100:1	75:1	50:1	25:1	TEMP(°C)	Humidity(%)
1	>60:00 ✘	>60:00 ✘	7:40 ○	NA ○	19.5	31
2	17:00 △	8:00 ○	4:30 ○	2:15 ○	21.2	29
3	17:00 △	7:30 ○	4:1 ○	2:15	21.5	31
4	>60:00 ✘	>60:00 ✘	3:45 ○	NA	21.5	34
5	>60:00 ✘	>60:00 ✘	3:30 ○	NA	21.7	32
6	>60:00 ✘	>60:00 ✘	>60:00 ✘	NA	21.9	28
7	>60:00 ✘	>60:00 ✘	4:30 ○	NA	21.9	31
8	17:00 △	7:30 ○	4:15 ○	2:00 ○	22.0	30
9	35:00 △	10:30 △	4:45 ○	NA	22.3	33
10	>60:00 ✘	10:00 ○	3:15 ○	1:36 ○	23.8	29
11	>60:00 ✘	30:00 △	4:50 △	1:30 ○	23.8	34
12	>60:00 ✘	>60:00 ✘	3:30 ○	2:30 ○	23.8	30
13	>60:00 ✘	>60:00 ✘	3:30 ○	NA	24.5	29
14	>60:00 ✘	>60:00 ✘	>60:00 ✘	NA	25.7	30
15	>60:00 ✘	>60:00 ✘	2:30 ○	NA	26.5	31
16	>60:00 ✘	>60:00 ✘	3:30 ○	1:25 ○	27.2	33



Figure 5.3 The polymer optimisation recorded for 16 batches of hybrid synthesis for different THF:GPTMS ratios, the two-pot mixing time point (mm:ss), and representative photographs of samples. The black circle represents homogeneous cylindrical shape hybrid; the black triangle irregular semi-cylindrical shape; and the black X represents formation of hollow cylinders which formed when no bubble formation occurred after added $\text{BF}_3 \cdot \text{OEt}_2$ catalyst in organic pot and mixed two-pot after 60 minutes. (Hybrid diameter is 1.2 cm and NA is not applicable)

The mixed two-pot solutions were cast in PTFE cylindrical moulds of 15 mm diameter and 25 mm height. To understand the shrinkage factor of samples, the dried samples were measured by the digital vernier calipers and μCT for computational

measurement and the results have been listed in table 5.2. The measured volume shrinkages are about 78.4% up to 87.0% for all samples compared with computational volume shrinkage of about 77.3% up to 87.3% based on different THF:GPTMS ratio. The computational volume shrinkage has higher accuracy compared with measurement result. However, the results suggest there is not much difference. To note that the results of measurements in different dimensions show that the shrinkage in the diameter of the cylinder was lower than the height shrinkage. The higher THF ratio at 100:1 demonstrates significant shrinkage compared with lower THF ratio samples. THF is acting as solvent and polymer. If the higher amount of THF is applied during the hybrid synthesis which can decrease the polymerisation rate and consequently increase evaporation during ageing process before forming a cylinder. Meanwhile, different drying processes have less effect on the shrinkage.

Table 5-2 The shrinkage behaviours of hybrid monoliths were evaluated and compared using μ CT and Vernier calliper measurement. The dimensional shrinkages were measured by Vernier callipers.

Sample	25OD	25FD	50OD	50FD	75OD	75FD	100OD	100FD
Volume shrinkage (%)								
Measurement	82.0 \pm 1.2	82.0 \pm 0.7	78.4 \pm 0.2	79.5 \pm 0.1	81.9 \pm 0.50	80.1 \pm 1.3	87.0 \pm 0.7	86.7 \pm 0.5
Computational	81.2 \pm 0.7	80.8 \pm 1.5	77.4 \pm 1.2	80.5 \pm 1.2	79.1 \pm 0.4	78.2 \pm 0.2	87.3 \pm 3.2	85.6 \pm 1.3
Dimensional shrinkage (%)								
Height	47.7 \pm 3.2	49.3 \pm 2.3	52.9 \pm 0.5	54.7 \pm 1.1	50.5 \pm 2.3	46.8 \pm 0.4	36.4 \pm 3.4	30.9 \pm 1.0
Diameter	61.3 \pm 0.1	60.4 \pm 0.5	62.2 \pm 0.4	62.7 \pm 0.4	62.8 \pm 0.6	62.1 \pm 0.6	59.9 \pm 4.0	65.5 \pm 0.8

5.3.2. Hybrid chemical and thermal analysis

TGA is an ideal characterisation technique for determination of the inorganic:organic ratio in the hybrids (Figure 5.4). As heating started in TGA, initially

only a few percent of the weight loss occurred, due to residual moisture evaporation around 100 °C and then weight began to drop drastically up to 180 °C, until the weight loss tended to ease after 350 °C, due to burn out of the organic components. The silica content can be obtained as 25OD (31.7%), 25FD (31.2%), 50OD (18.0%), 50FD (17.1%), 75OD (13.1%), 75FD (15.3%), 100OD (12.4%), and 100FD (13.8%), respectively.

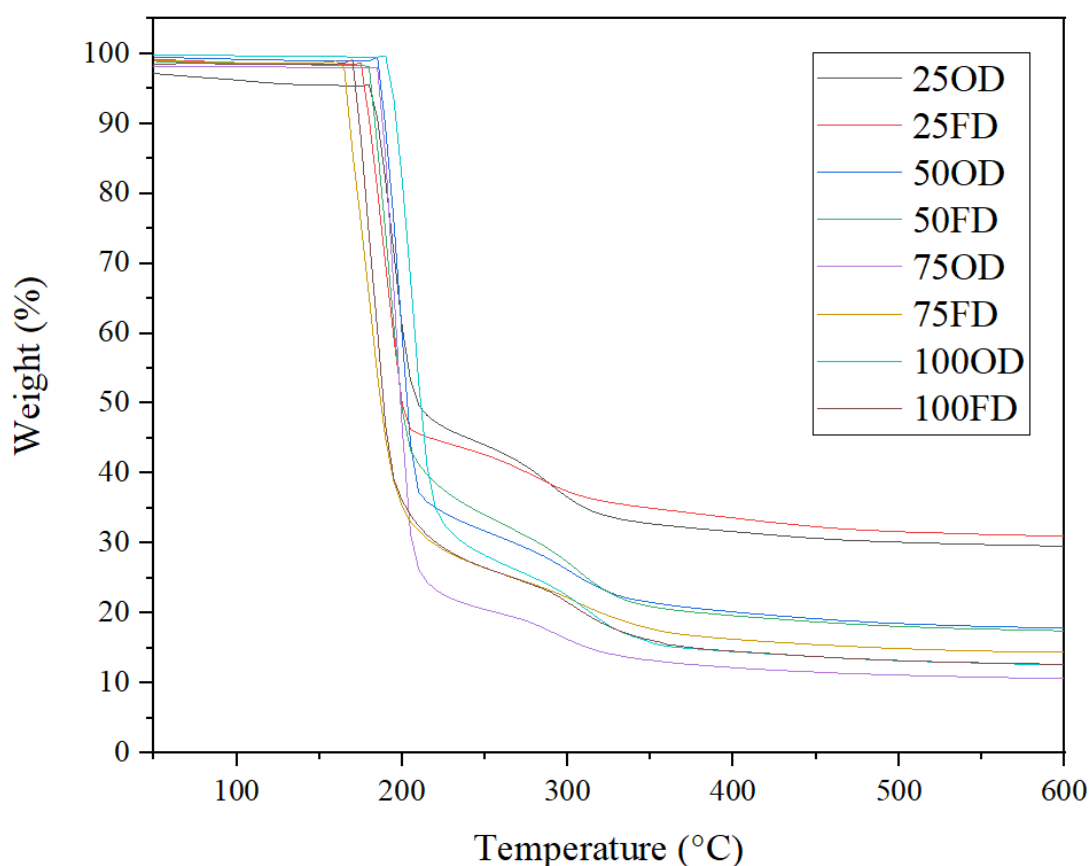


Figure 5.4 TGA analysis for quantitative analysis of the inorganic and organic compositions in SiO₂-PolyTHF hybrids by comparing oven drying (OD) and freeze drying (FD) samples. The samples named by the molecular ratio of THF:GPTMS (as 1) and the drying methods which are 25OD, 25FD, 50OD, 50FD, 75OD, 75FD, 100OD, and 100FD.

The chemical analysis of hybrids has been evaluated by FTIR. The FTIR results are shown in Figure 5.5. All spectra showed similar absorption position. The absorption of the Si-O-Si symmetric vibration at around 800 cm^{-1} and the Si-OH stretch at around $960\text{-}980\text{ cm}^{-1}$ increased as the THF:GPTMS ratio increased. There was also an absorption shift from 1079 cm^{-1} to 1042 cm^{-1} , the absorption shift contributed more oxygen-containing dimers incorporated into a single dimer from H-Si-O-Si-H to H-Si-O-Si(O)-H [129, 130] which suggested in the lower THF contained sample.

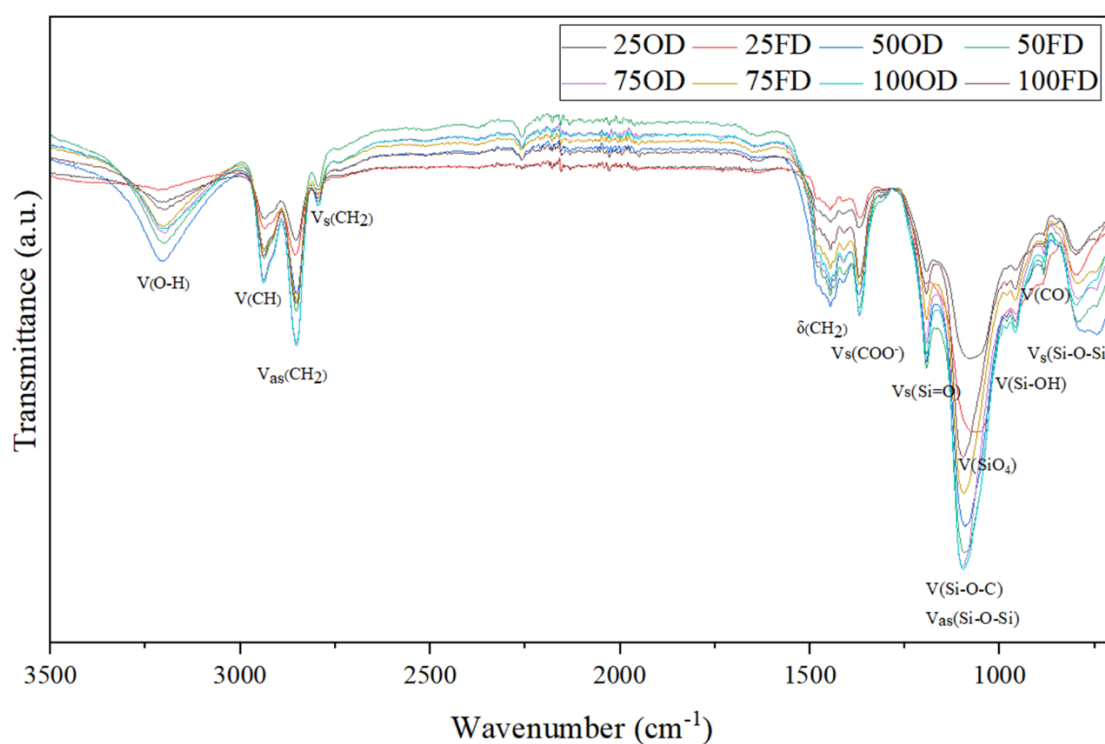


Figure 5.5 FTIR spectra of SiO_2 -PolyTHF hybrids with different compositions and oven drying (OD) and freeze drying (FD) methods. The samples named by the molecular ratio of THF:GPTMS (as 1) and the drying methods which are 25OD, 25FD, 50OD, 50FD, 75OD, 75FD, 100OD, and 100FD.

5.3.3. Hybrid characterisation

The mechanical property is one of crucial properties of monolithic hybrids. Compression testing was conducted in vertical direction on the cylindrical hybrids. The representative stress-strain curves are shown in Figure 5.6. Figure 5.6 (a) shows oven drying results and the figure 5.6 (b) shows freeze drying results. The higher silica samples had higher compressive strength. The 25OD and 25FD samples deformed when stress is applied, and cracks occurred while reached the maximum stress. Finally, the samples were squeezed. The 50OD and 50FD samples demonstrated greater deformation and cracks occurred while the maximum stress is applied. For the lower silica samples, the samples collapsed when the stress reached the maximum. The trend of stress and strain is shown in Figure 5.7 (a) and (b), which shows that the compressive strength decreased as the amount of silica content decreased. Also, FD samples of the composition had lower compressive strength than the corresponding OD. In terms of strain, the samples with the highest and lowest silica content that were FD showed reduced strain to failure. The 50OD and 50FD samples have a better balance between compressive strength and strain, they have higher strength and behave highest deformation tolerance simultaneously.

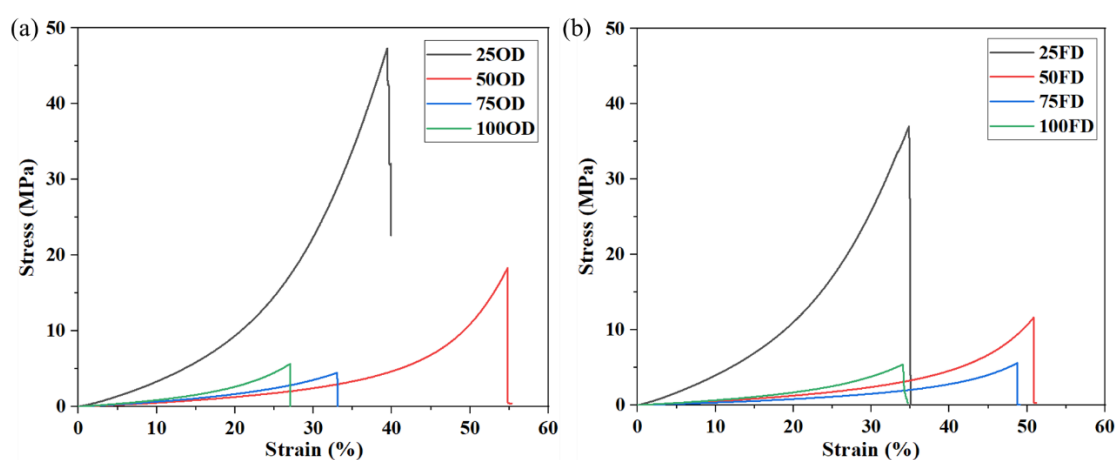


Figure 5.6 Representative curves for stress-strain behaviour of the hybrid cylinders following; (a) oven drying (OD); (b) freeze drying (FD). The samples named by the

molecular ratio of THF:GPTMS (as 1) and the drying methods which are 25OD, 25FD, 50OD, 50FD, 75OD, 75FD, 100OD, and 100FD.

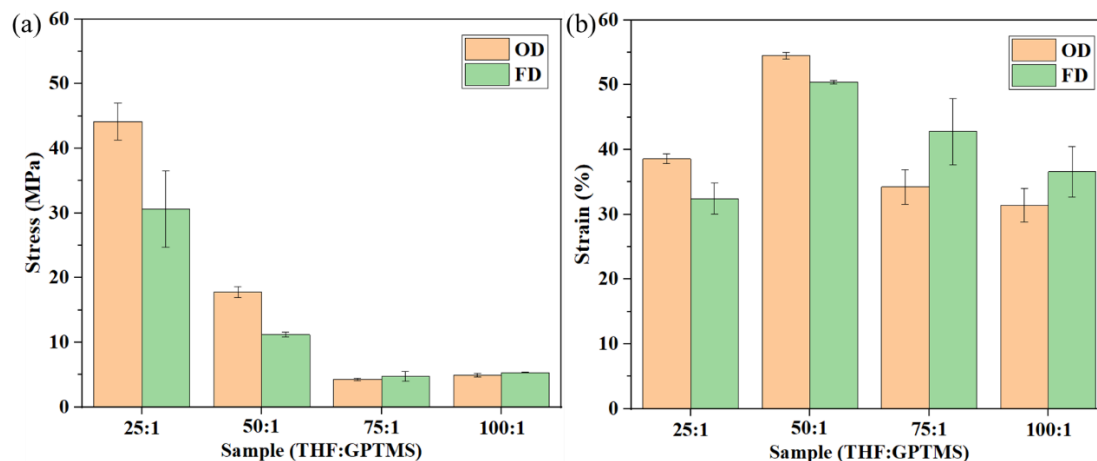


Figure 5.7 (a) Stress and (b) strain at fracture for hybrids the same THF:GPTMS ratio but different drying methods. The samples named by the molecular ratio of THF:GPTMS (as 1) and the drying methods (Oven drying (OD) and freeze drying (FD)) which are 25OD, 25FD, 50OD, 50FD, 75OD, 75FD, 100OD, and 100FD.

The surface morphology and inner structure of crack-free hybrid monoliths was imaged using SEM (Figure 5.8). The SEM images illustrated the surface morphology of all samples were approximately flat without obvious cracks and defects. The FD samples had irregular island-like phase separation. In order to analyse these phase separations, the inner structure of hybrid materials was observed. SEM was used to image the fracture surfaces from the compression test samples.

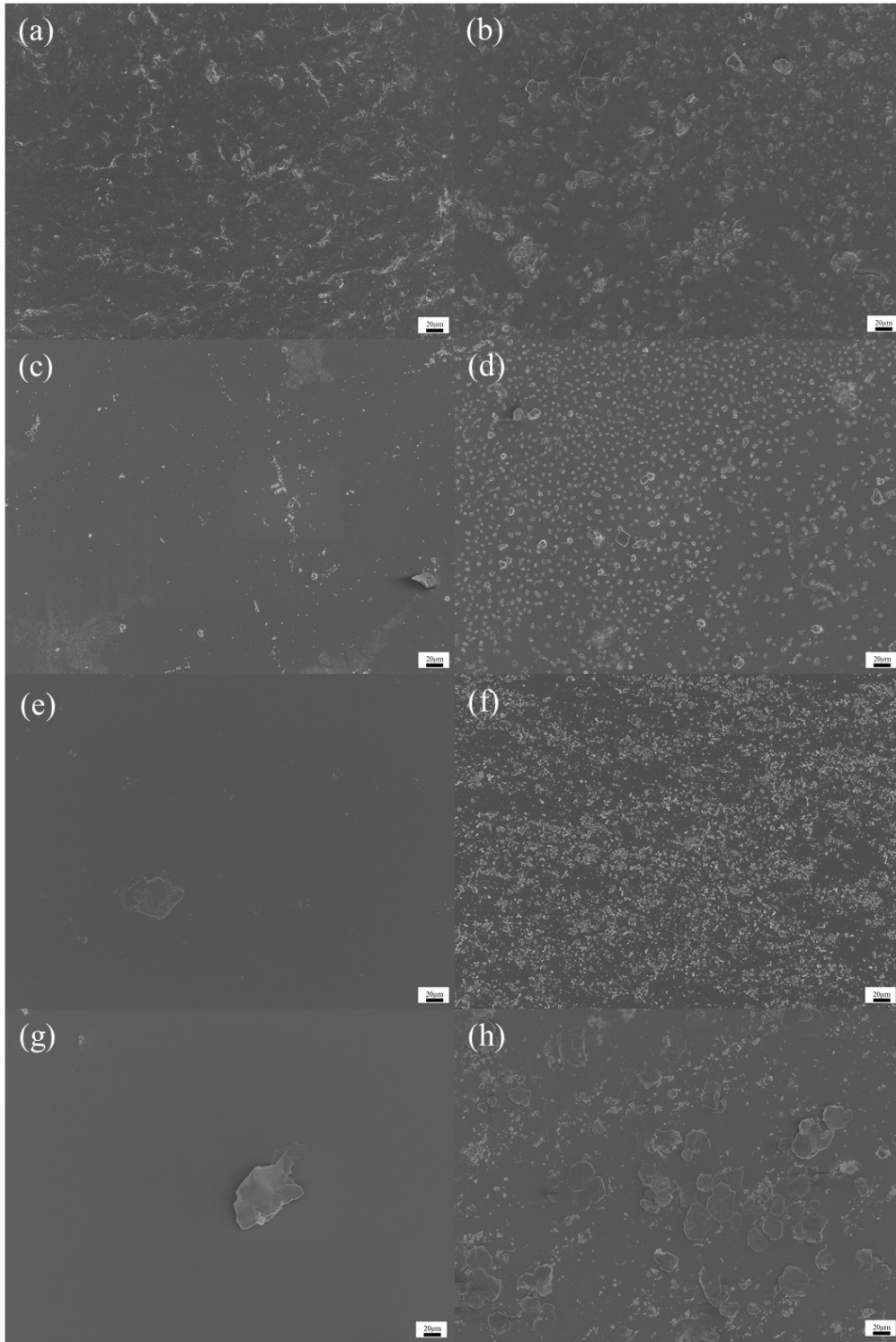


Figure 5.8 SEM images of SiO₂-PolyTHF hybrid surface morphology: (a) 25OD, (b) is 25FD; (c) 50OD; (d) 50FD; (e) 75OD; (f) 75FD; (g) 100OD; (h) 100FD.

The SEM images of fracture surface are shown in Figure 5.9. When observing the

fracture surface, no obvious structural cracks were found in all samples. Fracture patterns formed on the high silica content sample surfaces and they were more dense on the FD sample surfaces. Many island-like lump phase separations appeared on the fracture surface of the FD samples but were less present on the OD samples. The EDS technique has been used for the composition analysis. Since the SiO₂-PolyTHF hybrid has only silica and PolyTHF, the EDS analysis focused on silicon composition of 50OD and 50FD samples as shown in Figure 5.10.

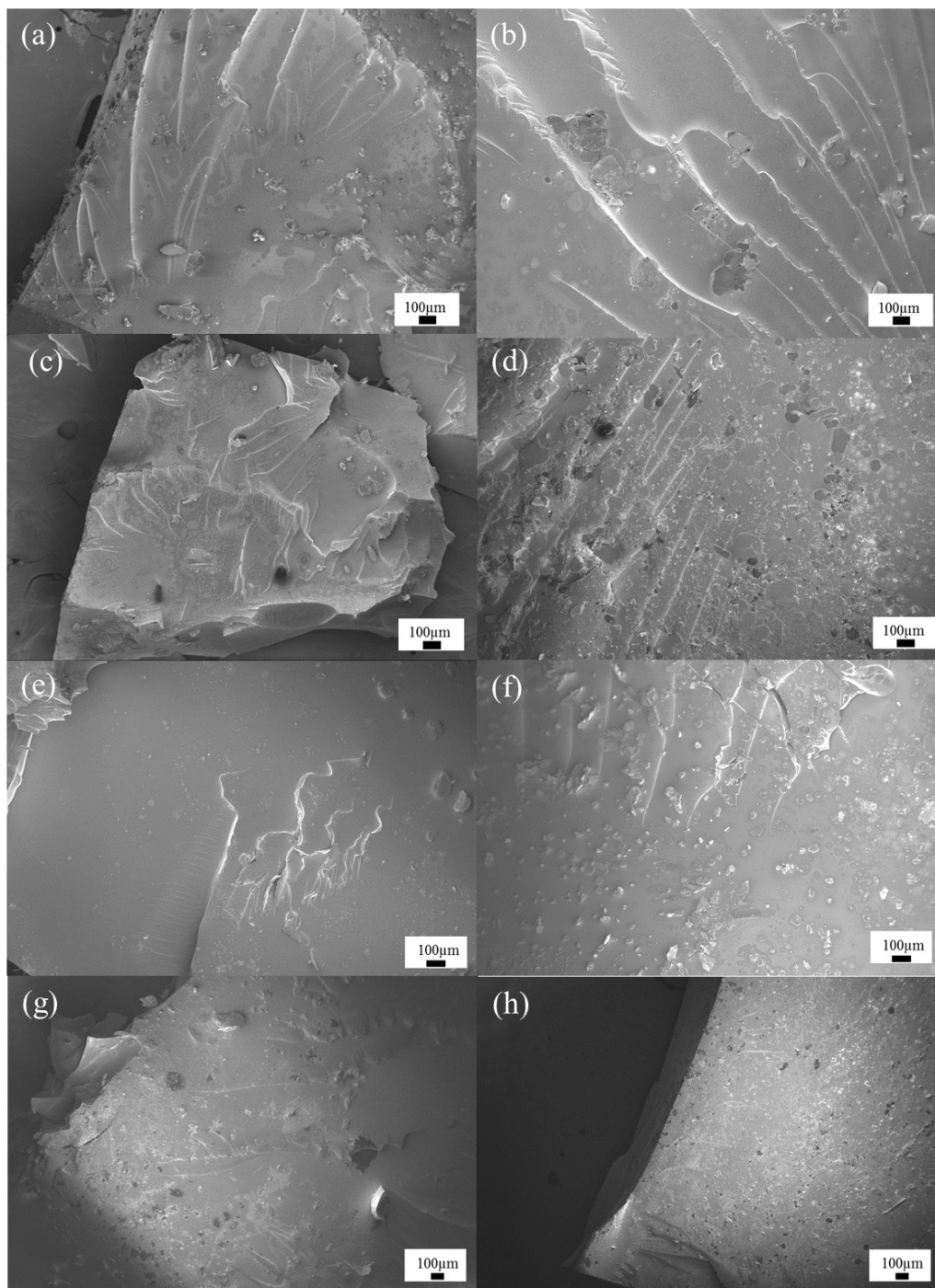


Figure 5.9 SEM images of SiO₂-PolyTHF hybrid fracture surface after compression test to failure: (a) 25OD; (b) 25FD; (c) 50OD; (d) 50FD; (e) 75OD; (f) 75FD; (g) 100OD; (h) 100FD.

The EDS analyses were focused on the flat fracture surface and the island-like phase separation. The flat surface had a strong silicon signal compared with the island-

like phase separations, which indicated the phase separation had higher organic content rather than being higher inorganic phase separation. That phase separation is due to OD and FD samples were prepared in different drying processes. OD samples were kept in the 37 °C oven throughout all aging and drying processes which is relatively stable. THF in *in-situ* CROP acted as a reactant and solvent simultaneously [105], GPTMS is used not only as initiator of polymerisation of PolyTHF but also the coupling agent between inorganic and organic moieties. The strong covalent bonds were formed between GPTMS with SiO₂ while mixing two-pot solution, thus reducing or preventing silica phase separation. On the other hand, FD sample were aging at 37 °C oven for 7 days then moved to -80 °C freezer to cooling sample before -93 °C FD process. This cooling stage may potentially cause nucleation on unreacted or semi-reacted THF and consequently observed the organic rich phase separation in the SEM images. These phase separations become potential weakening points in the structure as resulting in the compression tests.

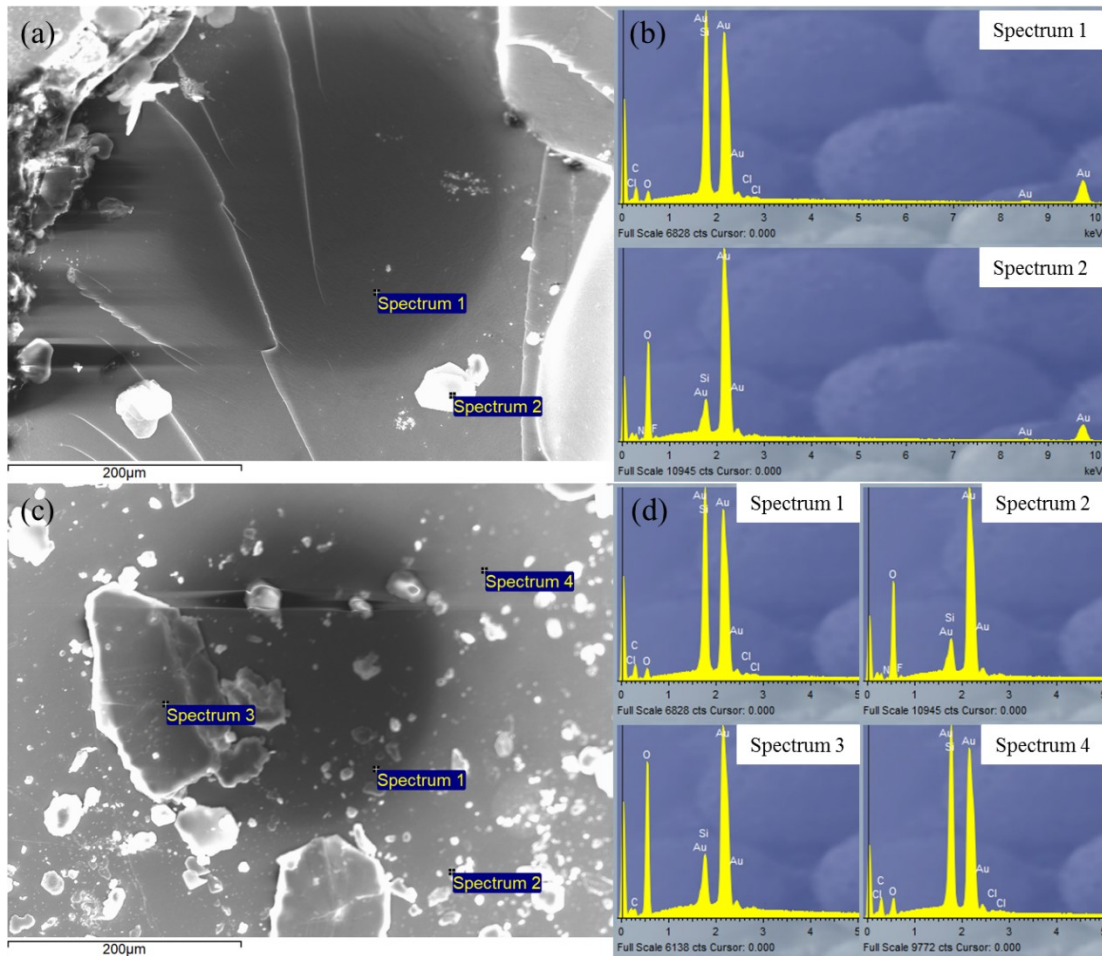


Figure 5.10 (a) SEM image of the surface of 50OD sample and (b) EDS with spectrum 1 focused on the flat surface and the spectrum 2 focused on precipitation; (c) SEM image of 50FD sample and (d) EDS (d) analysis with spectra 1 and 4 focused on the flat surface and spectra 2 and 3 focused on the precipitations.

5.3.4. Hybrid dissolution and long-term use study

The stability of hybrid monolith was evaluated *in-vitro*. The degradation and mechanical cyclic tests were tested before and after SBF immersion and cyclic tests were performed under wet condition compared with day 0 dry condition. Weight loss was recorded before and after soaking in SBF for 90 days and the results have been shown in Figure 5.11. Full data of the tests have been listed in table 5.3. For high silica content samples nearly 2.7% of weight was lost on the first day, and the weight loss

decreased to about 0.5% after 7 days, and the weight loss was further reduced by less than 0.1%. However, the lower silica content sample lost less than 0.1% of weight loss over 7 days. That is because the higher density of incompletely reacted silica was at the surface of the hybrid and was flushed away when soaked into SBF. While the *in-vitro* test data is shown the weight loss tend to stable after 14 days test. The weight loss is reduced less than 0.1% in each composition.

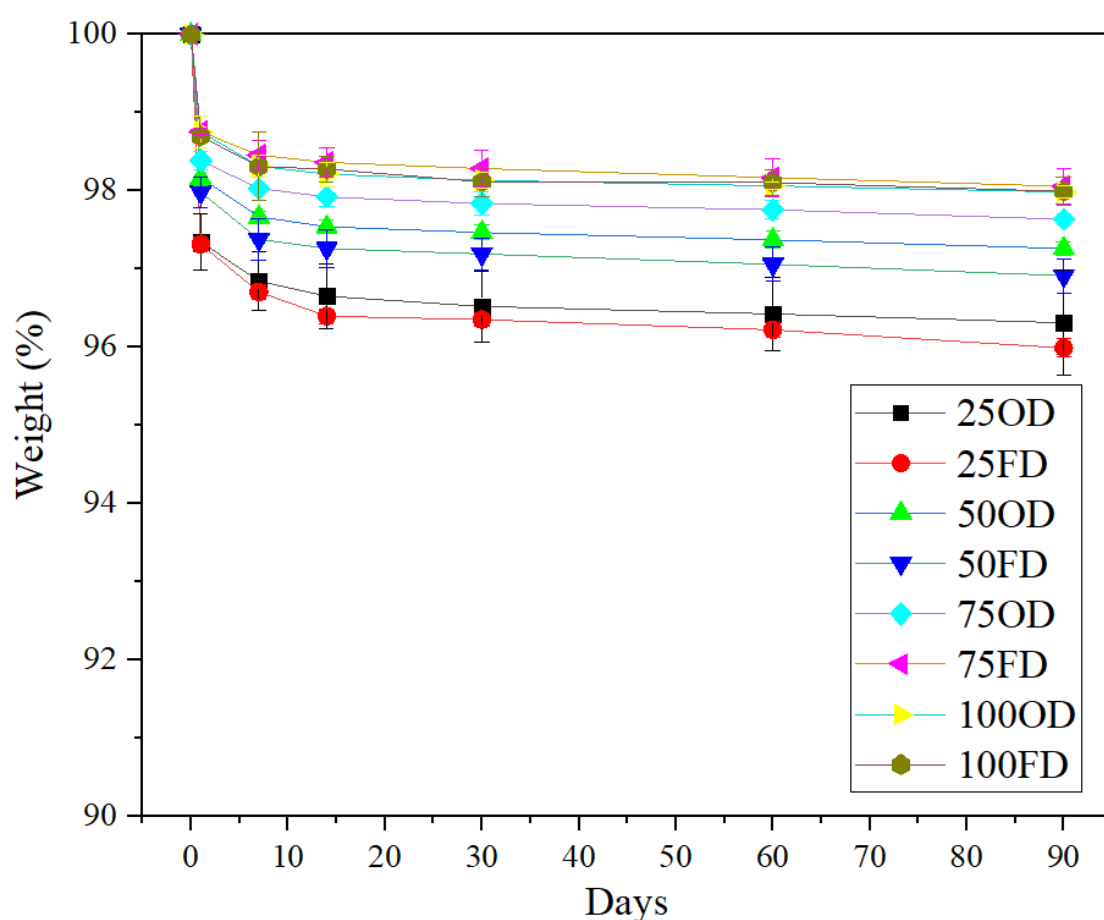


Figure 5.11 The degradation study recorded the weight loss before and after soaking SiO₂-PolyTHF hybrids in PBS in an incubating orbital shaker held at 37°C, agitated at 120 rpm for 1, 7, 14, 30, 60, and 90 days. The samples named by the molecular ratio of THF:GPTMS (as 1) and the drying methods (Oven drying (OD) and freeze drying (FD)) which are 25OD, 25FD, 50OD, 50FD, 75OD, 75FD, 100OD, and 100FD.

Table 5-3 The full data of weight loss of hybrids for 90 days *in-vitro* test. The samples named by the molecular ratio of THF:GPTMS (as 1) and the drying methods (Oven drying (OD) and freeze drying (FD)) which are 25OD, 25FD, 50OD, 50FD, 75OD, 75FD, 100OD, and 100FD.

Day	Weight (%) \pm							
	25OD		25FD		50OD		50FD	
0	100		100		100		100	
1	97.34	0.35	97.31	0.09	98.16	0.10	97.98	0.19
7	96.84	0.36	96.70	0.08	97.66	0.07	97.37	0.26
14	96.65	0.41	96.39	0.09	97.54	0.08	97.26	0.23
30	96.52	0.45	96.35	0.09	97.46	0.09	97.19	0.20
60	96.42	0.46	96.22	0.08	97.37	0.10	97.05	0.22
90	96.31	0.67	95.98	0.11	97.26	0.08	96.91	0.21

Day	Weight (%) \pm							
	75OD		75FD		100OD		100FD	
0	100		100		100		100	
1	98.38	0.11	98.75	0.04	98.75	0.20	98.69	0.08
7	98.03	0.14	98.45	0.18	98.31	0.14	98.31	0.43
14	97.92	0.12	98.36	0.19	98.21	0.15	98.28	0.16
30	97.83	0.15	98.28	0.23	98.13	0.09	98.11	0.18
60	97.75	0.11	98.16	0.24	98.06	0.04	98.10	0.16
90	97.63	0.06	98.05	0.23	97.98	0.07	97.99	0.18

The dissolution ICP suggested a similar trend in Figure 5.12. Higher silica content and FD samples produced higher silicon release in the ICP results. The 25FD sample showed 128 ppm of silicon released after the first 14 days and the cumulative release only increased by 67 ppm in the remaining experiment. On the contrary, the 100OD sample showed about 42 ppm of silicon released at first 14 days and 21 ppm released after 90 days study. These results suggested significant release at initial stage and tend to be less degradation behaviour at long-term study. The full data of dissolution study is listed in table 5.4.

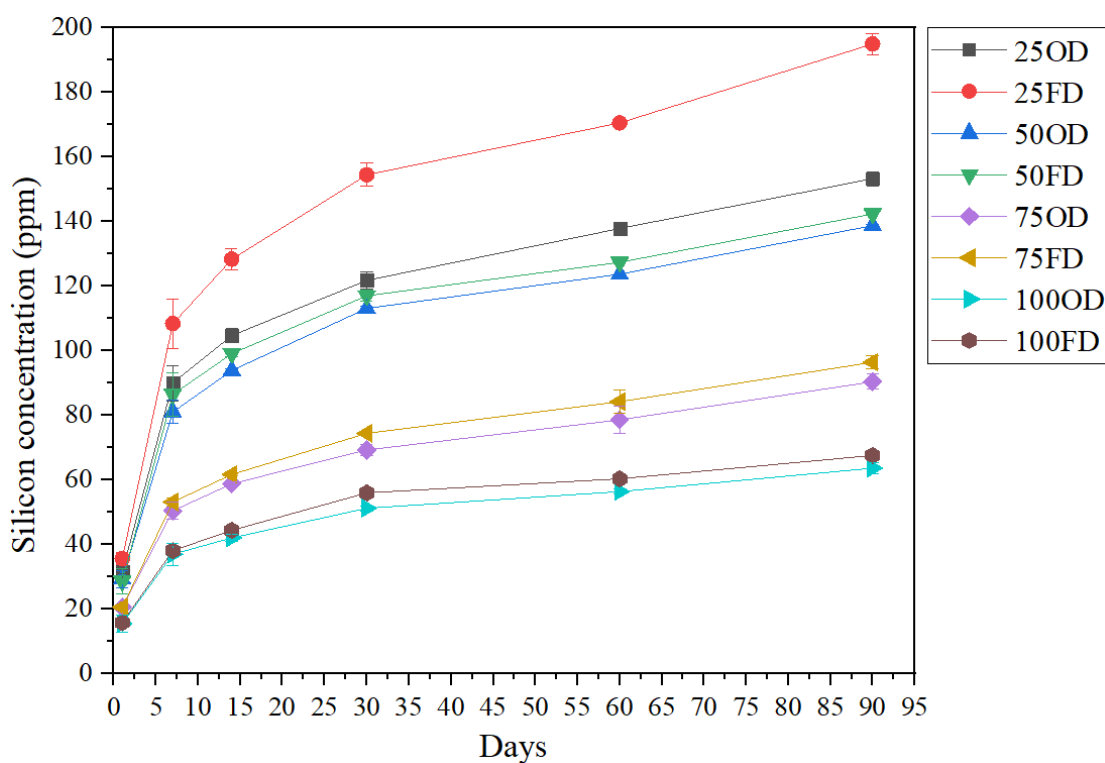


Figure 5.12 The dissolution study of SiO₂-PolyTHF hybrids soaked in PBS and placed in an incubating orbital shaker held at 37°C, agitated at 120 rpm for 1, 7, 14, 30, 90 and 90 days.

Table 5-4 The full data of ICP of hybrids for 90 days in-vitro test.

Day	Ppm ±							
	25OD		25FD		50OD		50FD	
1	31.60	0.71	35.57	1.92	29.25	2.57	28.56	3.96
7	90.01	5.46	108.38	7.761	81.06	3.58	86.49	6.63
14	104.70	2.29	128.32	3.33	93.86	0.59	99.07	0.86
30	121.77	2.53	154.48	3.59	113.15	0.63	117.03	1.62
60	137.87	1.34	170.58	1.344	123.69	0.26	127.41	0.34
90	153.33	2.15	195.02	3.20	138.78	0.41	142.39	0.13

Day	Ppm ±							
	75OD		75FD		100OD		100FD	
1	20.48	0.52	20.55	0.50	15.42	2.68	15.81	1.45
7	50.43	2.57	53.16	1.15	36.94	3.37	38.11	1.65
14	58.79	0.60	61.70	0.29	42.03	0.98	44.34	0.61
30	69.29	1.67	74.43	0.33	51.19	0.83	55.95	1.49
60	78.58	4.24	84.20	3.50	56.34	0.82	60.32	0.59
90	90.39	2.38	96.44	2.08	63.58	1.58	67.58	0.50

Cyclic compression testing was carried out on cylindrical hybrids before and after soaking in PBS for 90 days. The samples experienced 1000 cycles in compression before being soaked in PBS and 100 cycles at each time point after 1, 7, 14, 30, 60 and 90 days soaking and were tested in wet condition. The cyclic test results of OD samples and FD samples are shown in Figures 5.13 and 5.14. The cyclic curve was regular at day 0 which has no significant curve deformation while applying cyclic stress and the appearance of the material did not change even after 1000 cycle compression loading in OD and FD samples. Although, the FD samples demonstrated lower compression strength, the cyclic patterns remained compact and regular in elastic deformation behaviour after 90 days soaking tests. At the lower THF contained samples, the cyclic stress increased after 90 days soaking test that increasing caused by PBS uptake in the hybrid. The lower THF contained samples have relatively higher SiO₂ which provides more hydrophilic behaviour due to the presence of the silanol (Si-OH) groups on the surface of the hybrid. The cyclic test results demonstrated the stress decreased by the testing time. The cyclic test results indicated that the SiO₂-PolyTHF hybrid monoliths have good reliability on the cyclic behaviour. There is no significant change in the response to cyclic compression stress even after thousands of cycles of cyclic compression and after PBS soaking for 90 days. The SiO₂-PolyTHF hybrid monolith exhibits excellent structural integrity and good mechanical reliability which brings many potential applications to the field of biomaterials such as cartilage replacement, joint defect filler, and intervertebral disc replacement.

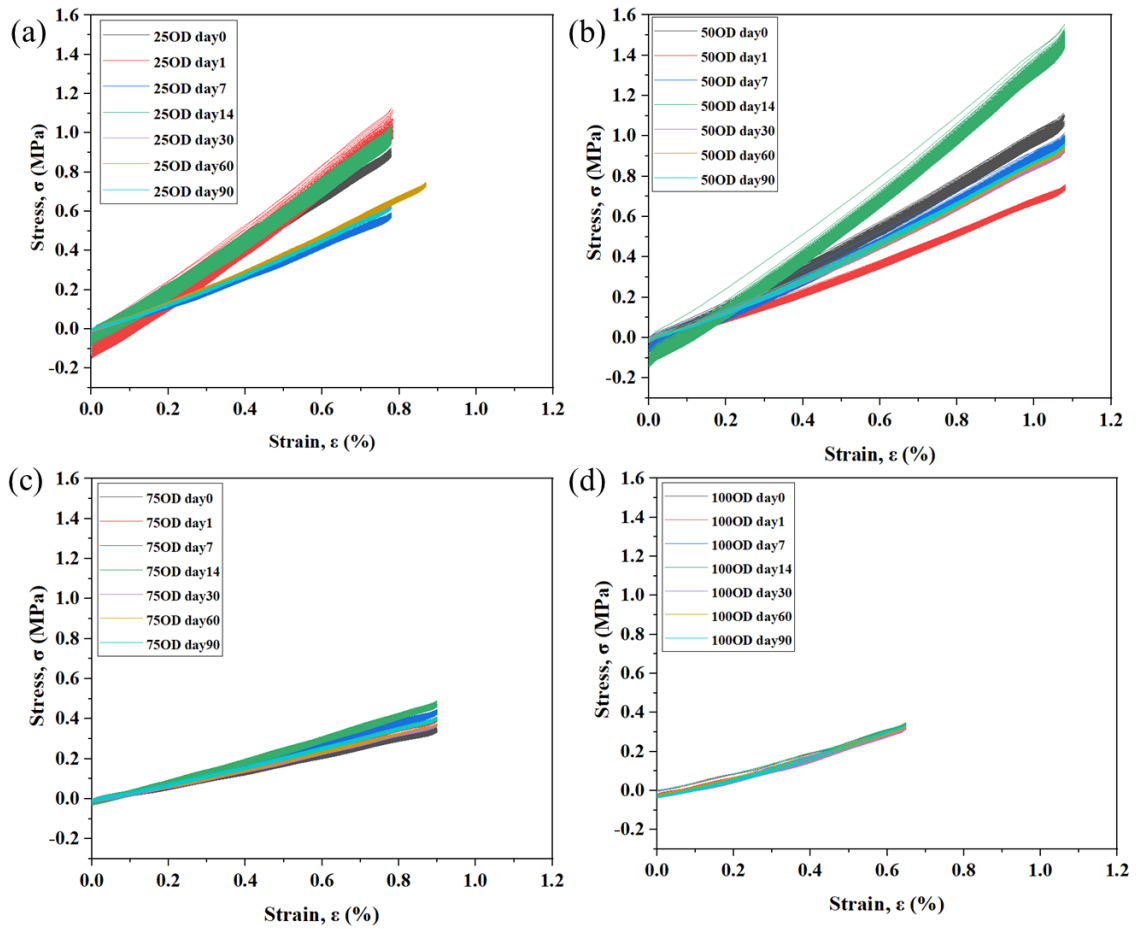


Figure 5.13 Cyclic compression testing of SiO₂-PolyTHF hybrids before and after soaking in PBS for 90 days: (a) 25OD, (b) 50OD, (c) 75OD, and (d) 100OD samples. Every 10 cycles of 10⁴ are shown. The samples named by the molecular ratio of THF:GPTMS (as 1) and the drying method (Oven drying (OD)) which are 25OD, 50OD, 75OD, and 100OD.

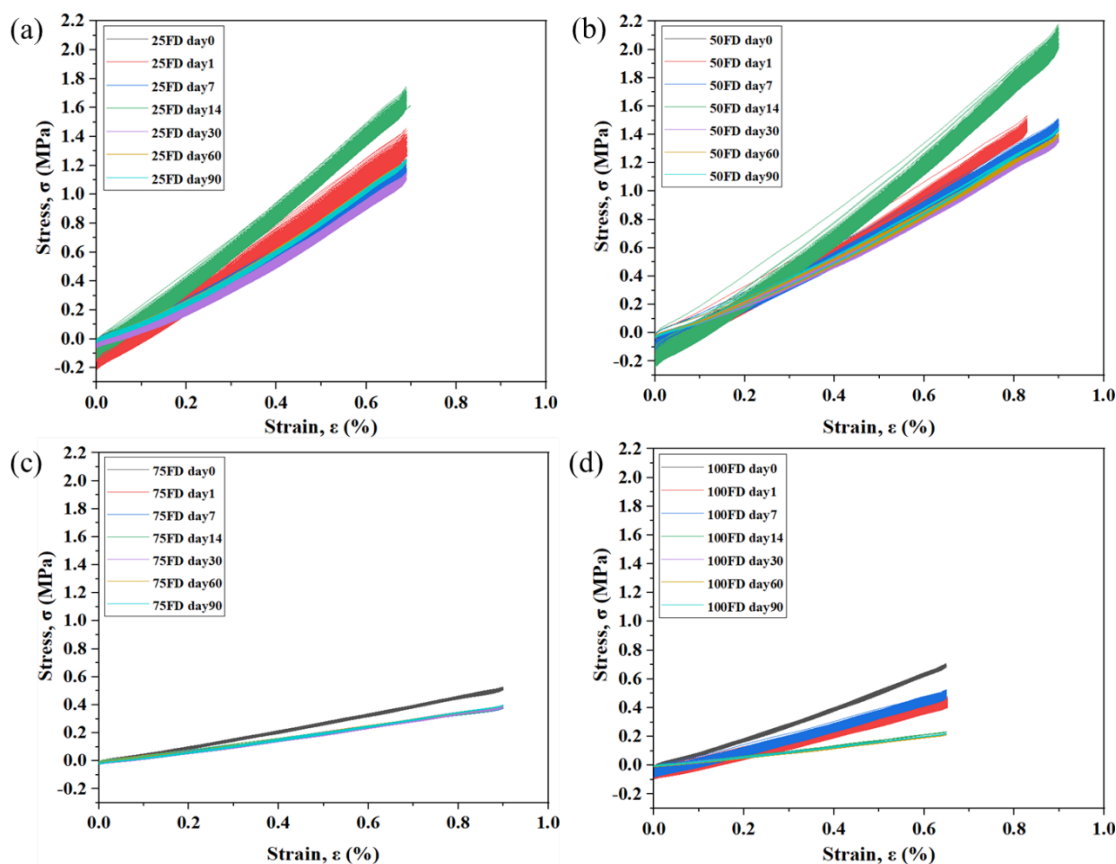


Figure 5.14 Cyclic compression tests of SiO₂-PolyTHF hybrids before and after soaking in PBS for 90 days: (a) 25FD, (b) 50FD, (c) 75FD, and (d) 100FD samples. Every 10 cycles of 10⁴ are shown. The samples named by the molecular ratio of THF:GPTMS (as 1) and the drying method (freeze drying (FD)) which are 25FD, 50FD, 75FD, and 100FD.

The compression study results suggest a similar behaviour in Section 5.3.3 on each OD and FD samples as shown in Figure 5.15. Hybrids with lower organic amount demonstrated higher compressive strength in two drying methods. The results of the two methods are consistent, which means that the performance of this material after long-term use is very consistent, and it can be used as a preliminary result to prove long-term stable application.

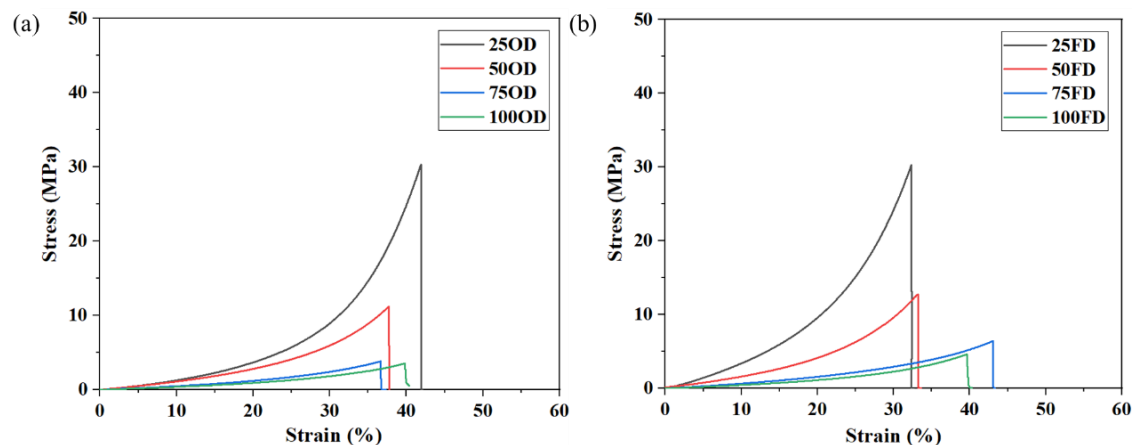
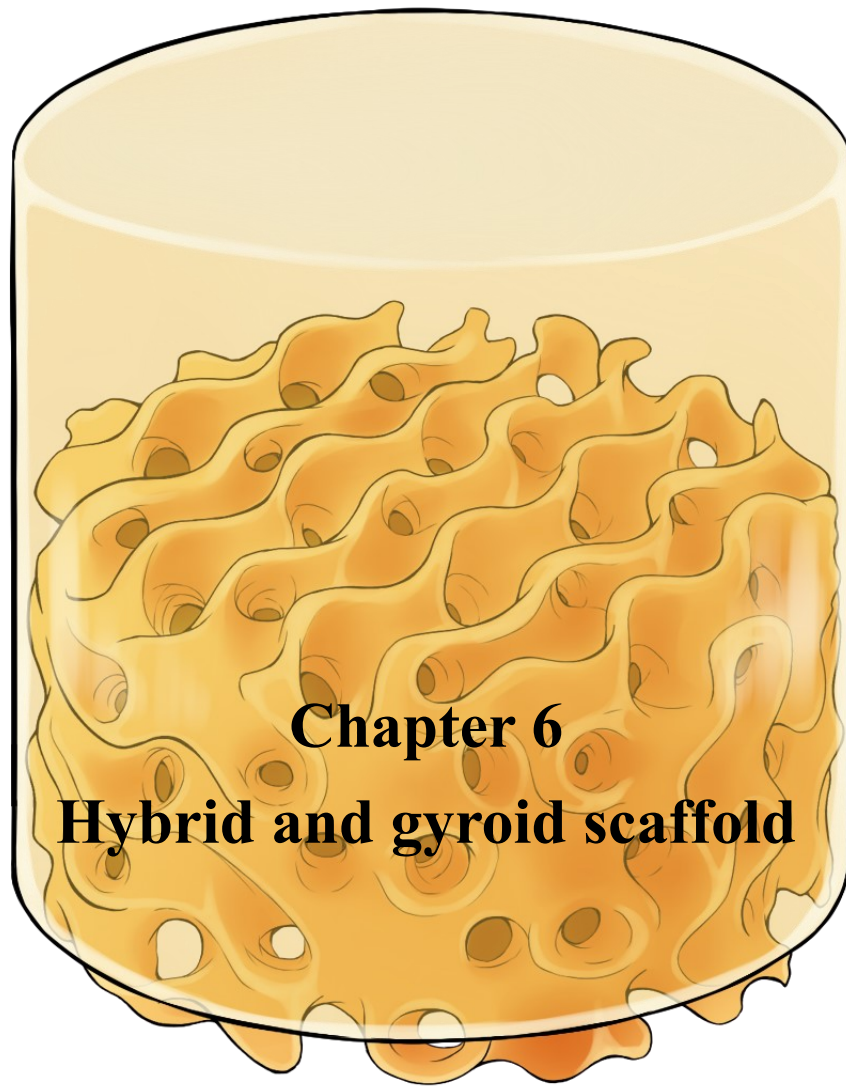


Figure 5.15 The representative compression curves for hybrids after 90 immersion in PBS (a) oven drying (OD) (b) freeze drying (FD). The samples named by the molecular ratio of THF:GPTMS (as 1) and the drying methods which are 25OD, 25FD, 50OD, 50FD, 75OD, 75FD, 100OD, and 100FD.

5.4. Conclusions

This research conducted a comprehensive study on SiO₂-PolyTHF hybrid monolith synthesis by investigating the effect of organic: inorganic ratios and two different drying processes. This hybrid material inherited both advantages from inorganic and organic moieties which increased the mechanical strength and ductility with higher silica content according to the combination of inorganic and organic moieties. OD method suggested better material stability in mechanical testing and less phase separation in SEM results.



Chapter 6
Hybrid and gyroid scaffold

6. Hybrid and gyroid scaffold for meniscus replacement

6.1. Introduction

Total knee replacement (TKR) is one of the most common musculoskeletal surgical procedures in the world which conducts over 1 million operations annually [131]. According to statistical results, the prevalence of total TKR in the total US population since 1980 to 2021. During the 30 years data suggest the prevalence grown from less than 1% to 10.4%. Although the average age of patients is about 65 years old [135], trends show that there is more and more younger patients having the procedure, with the lifetime risk of revision of approximately 35% for men and 20% for women compared with older than 65 years old patients, for whom the revision rate is less than 15% for men and 7% for women [136]. The reasons for revision surgery are very depending on the conditions of the patient, but the most comment happened on the artificial implant are implant loosening, infection, unknown pain, and instability [137]. The reasons for significant problem that can caused by implants generating subsequent migration of wear particles. These particles may consequently change implant stability and cause some biological response [138].

Although, there are several types of TKR device, Ultra-high molecular weight polyethylene (UHMWPE) is the most common used friction pair on metal-on-UHMWPE combination. Therefore, many researches have tried to modify the functions of UHMWPE to reduce the friction and improve the wear properties of UHMWPE such as nanoparticle reinforcement [139], macromolecular cross-linking [140], increasing the degree of crystallinity [141], and bearing coating [142]. These modifications have tried to lower friction to prevent wear particle formation and also for improving wear life.

This study aims to develop a new device for meniscus replacement for younger patients allowing preservation of natural tissue, delaying the need for a TKR, which removes all surrounding tissue. Key objectives are: creating a bearing surface for the opposing articular cartilage, such that the material/ cartilage coefficient is low, minimising friction and damage to the articulating surface; development of a fixation method for the synthetic meniscus through AM of porous Ti scaffolds that can be integrated with the hybrid. In order to prepare the hybrid and gyroid scaffold with good integrity, different compositions and preparation methods were discussed in this chapter. A titanium gyroid scaffold is made by selective laser melting (SLM) technique which is acting as bone anchors for mechanical fixation of hybrid on the implant site and the gyroid scaffold is acting as biological fixation simultaneously.

6.2. Materials and Methods

6.2.1. Fabrication of Ti gyroids

The gyroid structures used in this study were designed in Rhinoceros 6.0 (Robert McNeel & Associates), with a cylindrical shape (16 mm diameter, 10 mm height) according to the equation: $\cos(x)\sin(y) + \cos(y)\sin(z) + \cos(z)\sin(x) = 0$, with a 4 mm unit cell and nominal porosity of 80%. These were sliced into build layers every 50 μm using Rhinoceros, and these layers were converted to a laser scan path using the custom-built Imperial College Lattice Slicer. Gyroid samples were fabricated using an AM250 metal powder bed fusion system (Renishaw plc., UK) using commercial titanium (CP-Ti) powder supplied by Carpenter Additive (Widnes, UK). Laser power of 50 W was used, with 50 μm point distance and 110 μs exposure time. Samples were built onto a CP-Ti build plate and were removed after manufacturing by wire-cut electrical

discharge machining, resulting in a final height of 8.5-9.0 mm. Before further processing Ti gyroids were cleaned ultrasonically in ethanol to remove loose powder. The Rhinoceros designed gyroid scaffold and the manufacturing technique also the structural observation method have been shown in Figure 6.1.

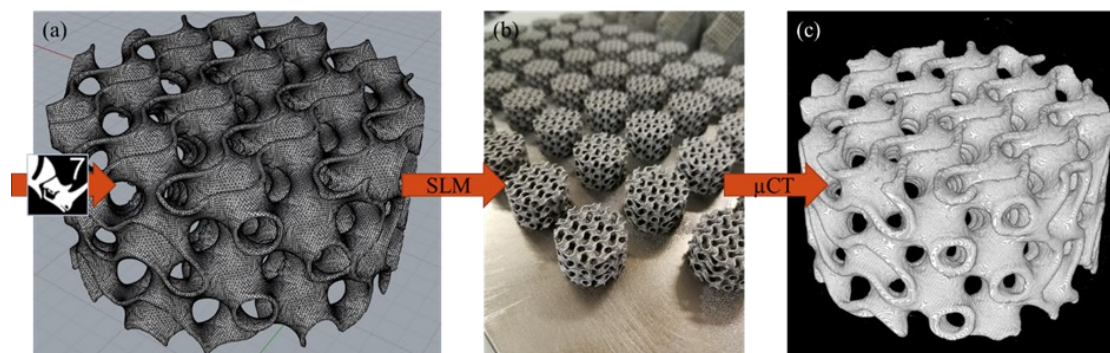


Figure 6.1 (a) Rhinoceros-designed gyroid scaffold; (b) Ti scaffolds printed using SLM (c) child volume of a SLM printed gyroid scaffold imaged using μ CT. (Gyroid scaffold is 16 mm)

6.2.2. Hybrid and gyroid scaffold preparation

SiO_2 -PolyTHF hybrid was prepared using two-pot synthesis and detail synthesis method mentioned in chapter 5.2.2 [106]. Following optimisation of the process in Chapter 5, the ratio of GTPMS was set as 1 for each composition. The molar ratios of THF, $\text{BF}_3 \cdot \text{OEt}_2$, TEOS, and deionised water are 50, 0.25, 2.5, and 13, respectively. The inorganic pot was hydrolysed TEOS using deionised water and 1 M of HCl 1:3 vol% ratio in a sealed beaker stirring at 400 rpm for at least 1 hour. The organic pot was mixed THF with GPTMS at 400 rpm for at least 15 minutes and the polymerisation was initiated by adding $\text{BF}_3 \cdot \text{OEt}_2$ catalyst for 3-6 minutes. The inorganic pot was mixed with organic pot while the organic pot observed clear bubbles for 10 minutes and left

to stand without stirring for 10 minutes.

On the other hand, the gyroid was immersed in acetone and ethanol solution for ultrasonic cleaning for 5 minutes each and dried using an air gun. The dried gyroid scaffold was placed in a 15 mm diameter and 30 mm high cylinder mould. After 10 minutes stabilisation, hybrid solution was directly added into mould along the mould wall which allow solution wicking into scaffold. The moulds were sealed in poly(methyl pentene) (PMP) pots and double sealed by parafilm and were placed in an oven at 40 °C for aging 7 days. At day 7, samples were moved to -80 °C freezer for at least 4 hours to freeze samples and opened the lid then moved to freeze-dry (FD) at -93 °C overnight. Samples were then moved to oven drying for another 7 days and ready for further experiments. Oven-dry (OD) samples were directly dried in the oven without FD steps after 7days aging.

6.2.3. *Micro computed tomography for inner gyroid scaffold measurement*

SLM technique is an AM method to build up 3D scaffold based on software designed file. The gyroid structure is designed using Rhinoceros. In order to observe the inner structure of gyroid scaffold after manufacturing. A laboratory-based micro computed tomography (μ CT) system (ZEISS Xradia 510 Versa) was used for imaging the structure. The X-ray source was operated at 80 kV and 10 A during the imaging. 800 captured projections were reconstructed using filtered back projection algorithm resulting in an 3D image matrix of $250 \times 256 \times 252$ with isotropic voxel size of 193 μ m. Samples within the 3D images were segmented using random forest voxel classifier (a machine learning algorithm) implemented using Ilastik software [108]. 800 segmented images were reconstructed using ImageJ software to build up a 3D image.

The porosity was calculated using 3D ImageJ suite plugin to compare with design file and strut size is measured using ImageJ to measure 300 pore sizes from μ CT images.

6.2.4. Scanning electron microscopy (SEM)

A Zeiss Auriga FIB-SEM equipped with an EDS detector was used at 5 kV in inlens mode, with working distance of 5-7 mm. Hybrid/ gyroid constructs were cut using an IsoMet® 5000 Linear Precision Saw (BUEHLER USA) with 3500 rpm blade speed and 1.2 mm/min feed rate as shown in Figure 6.2. Figure 6.2 (a) and (b) demonstrated sample clamped on the sample stage and applied water cooling and ready for cutting. Figure 6.2 (c and d) demonstrated cutting and the final cut sample. The sectioned piece was for SEM. Samples mounted on aluminium stubs stucked on carbon tape followed by coating with 10 nm of gold twice (Q150T sputter coated, Quorum Technologies, UK) to prevent charging of the sample. SEM was used to observe the inner and cross-section of the hybrid and gyroid and trying to observe the interaction and wicking performance of hybrid and gyroid interface.

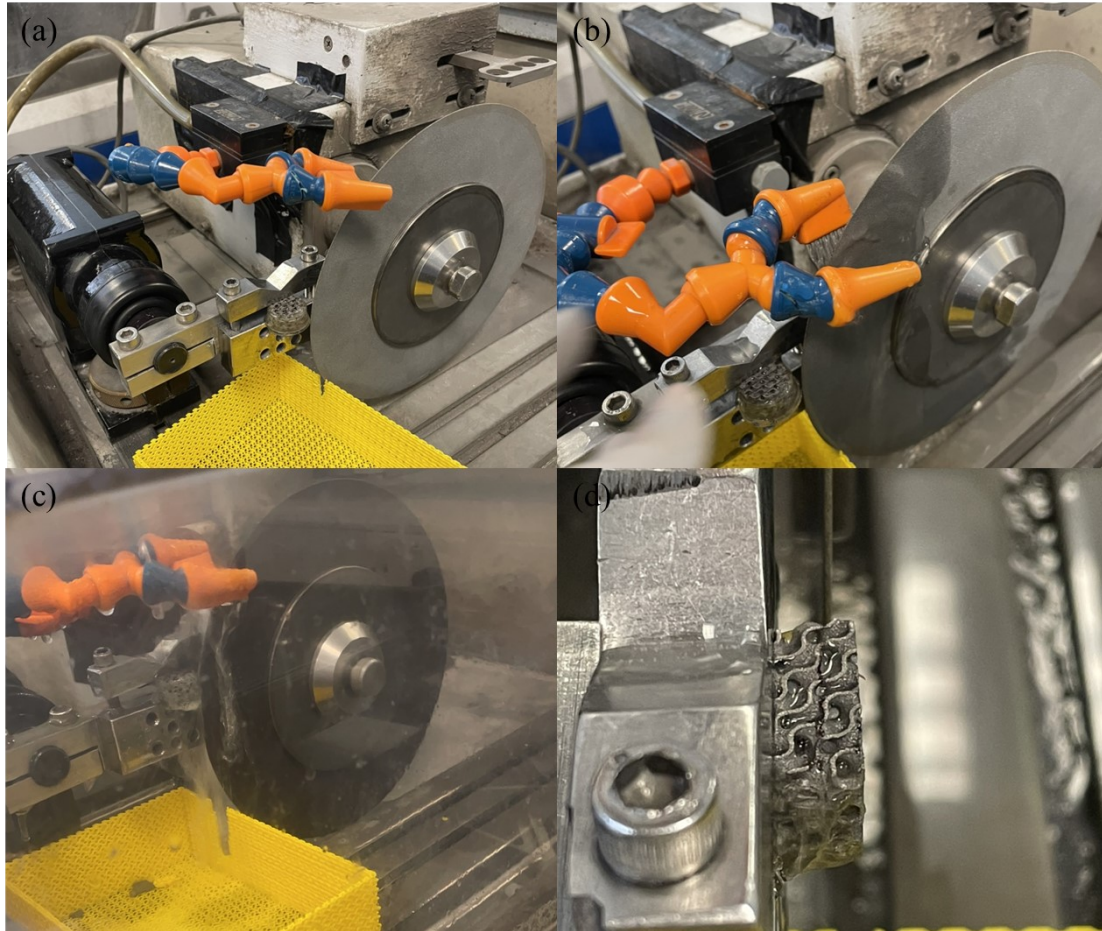


Figure 6.2 Hybrid and gyroid constructs were sectioned using an IsoMet® 5000 Linear Precision Saw. (a) sample clamped on the sample stage and (b) applied cooling water, (c) cutting, and (d) cut sample with flat sample.

6.2.5. *Mechanical properties*

Uniaxial compression was performed using Zwick/Roell testing machine 10 kN load cell at 0.1 mm/ min compression rate under 9 N of preload to failure for compression testing. The compression testing is to evaluate deformation tolerance ability while normal force applied.

Shear testing was performed by Zwick/Roell testing machine 10 kN load cell at 0.1

mm/ min shear rate under 9 N of preload to failure. A bespoke universal shear testing rig was designed using Solidworks (Appendix S1) that is suitable for 10-18 mm diameter of cylinder sample and the screw size is M4*20mm as shown in Figure 6.3. Shear force was applied by a one-sided cutting blade which has 1 mm of blade width to the base of the bracket and parallel to the hybrid and titanium gyroid scaffold interface [149]. This test is to understand the shear ability of hybrid and gyroid interface.

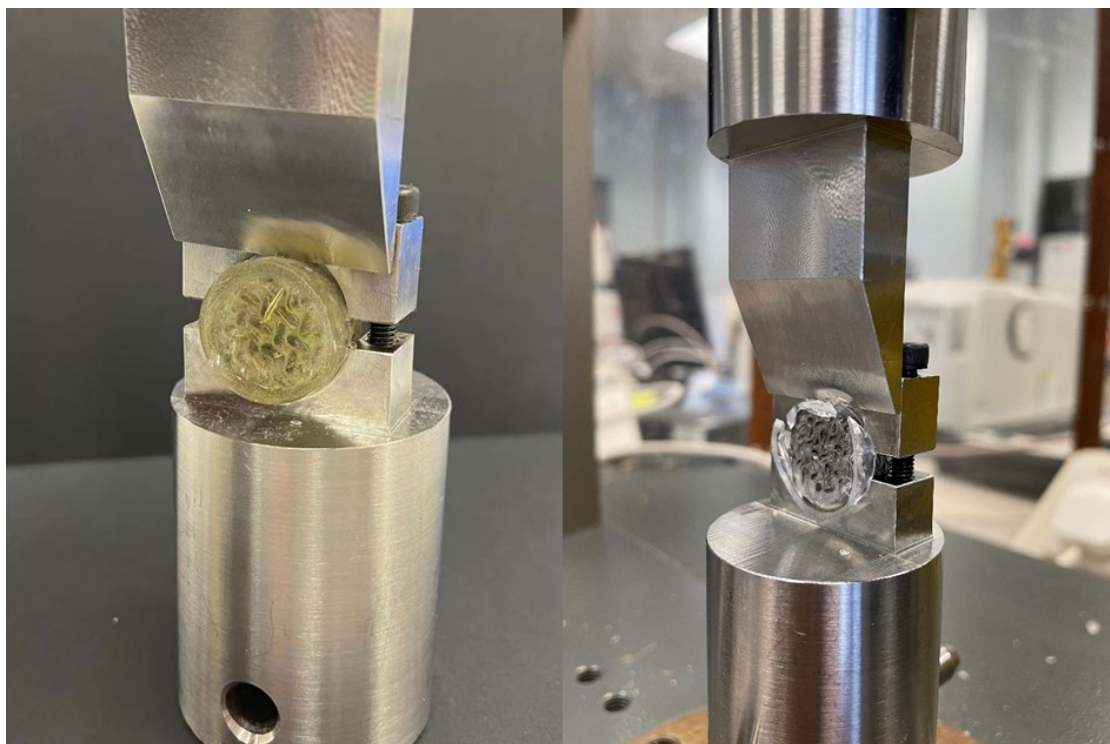


Figure 6.3 Shear test apparatus using our bespoke universal shear test rig: (a) before shear test and (b) after shear test.

Cyclic loading tests was performed using the same cyclic uniaxial compression mode by Zwick/Roell testing machine 10 kN load cell. The samples were preloaded under 9 N and compression path was dependent on the 20% of failure strain obtained from compression testing and the cyclic rate was calculated as one compressive cycle per second. The cyclic testing was performed as received hybrid cylinder for 10^4 cycles.

In order to understand the sample reliability in wet conditions, the hybrid cylinders were soaked in PBS for 1, 14, 30, 60, and 90 days and samples were placed in an incubating orbital shaker held at 37°C, agitated at 120 rpm. Cyclic testing was performed at each time point on soaked sample directly with PBS without other treatments.

6.2.6. Tribology test

In order to understand the friction behaviours of samples against knee cartilage as potential knee replacement device, knee cartilage was harvested from stifle joints of bovine calves obtained from a local abattoir within 6 h of slaughter and kept at 4°C until dissection. The bovine knee is shown in Figure 6.4 (a). Cartilages were removed from the medial and lateral femoral condyles as shown in Figure 6.4 (b). 8 mm biopsy punch was used for shaping cartilage as shown in Figure 6.4 (c). Removed cartilage (Figure 6.4 (d)) was stored in sterile PBS with 100 µg/mL penicillin and kept in 4°C until tribology test.

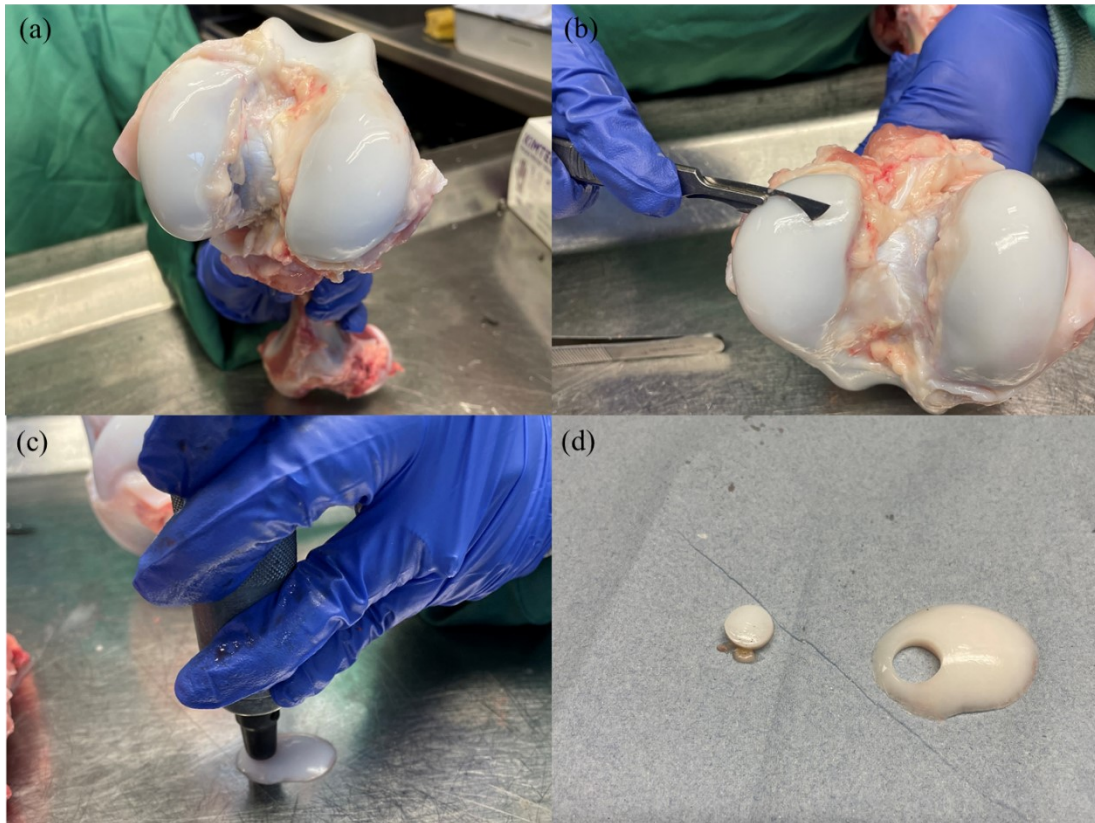


Figure 6.4 Cartilage dissection: (a) the bovine cartilage was removed surrounding tissues; (b) cutting cartilage from the femoral condyle; (c) using biopsy punch to remove 8 mm of cartilage disc; and (d) harvested knee cartilage and ready for tribology test.

The schematic diagram of tribology test setup has been shown in Figure 6.5. Self-design tribology rigs were designed using Solidworks (Appendix S2) on top and bottom rigs. The top rig was used to clamp hybrid and gyroid scaffold with two screws from x and y direction which hybrid faces down to contact with knee cartilage. The bottom specimen tray had an 8 mm diameter and 1 mm depth hole in the central site for cartilage positioning, fixed using super glue. This bottom tray had a 2 mm high wall which can apply small amount of lubrication. The tribology test was conducted under linear reciprocating motion along Y-axis with a stroke length of 5 mm at 1 Hz and giving an average speed of 10 mm/s for 600 cycles test using the Bio-Tribology Machine

(BTM) (PCS Instruments, UK). All tests were conducted under a deadweight load of 1 N and PBS was applied as lubrication. The significant difference between the samples was validated using a one-way Analysis of Variance (ANOVA) at 95% confidence interval with a p -value < 0.05 . The surface roughness of cartilages and samples were investigated using olympus OLS 5000 LEXT confocal microscope (Olympus corporation, UK) with a magnification of 10x.

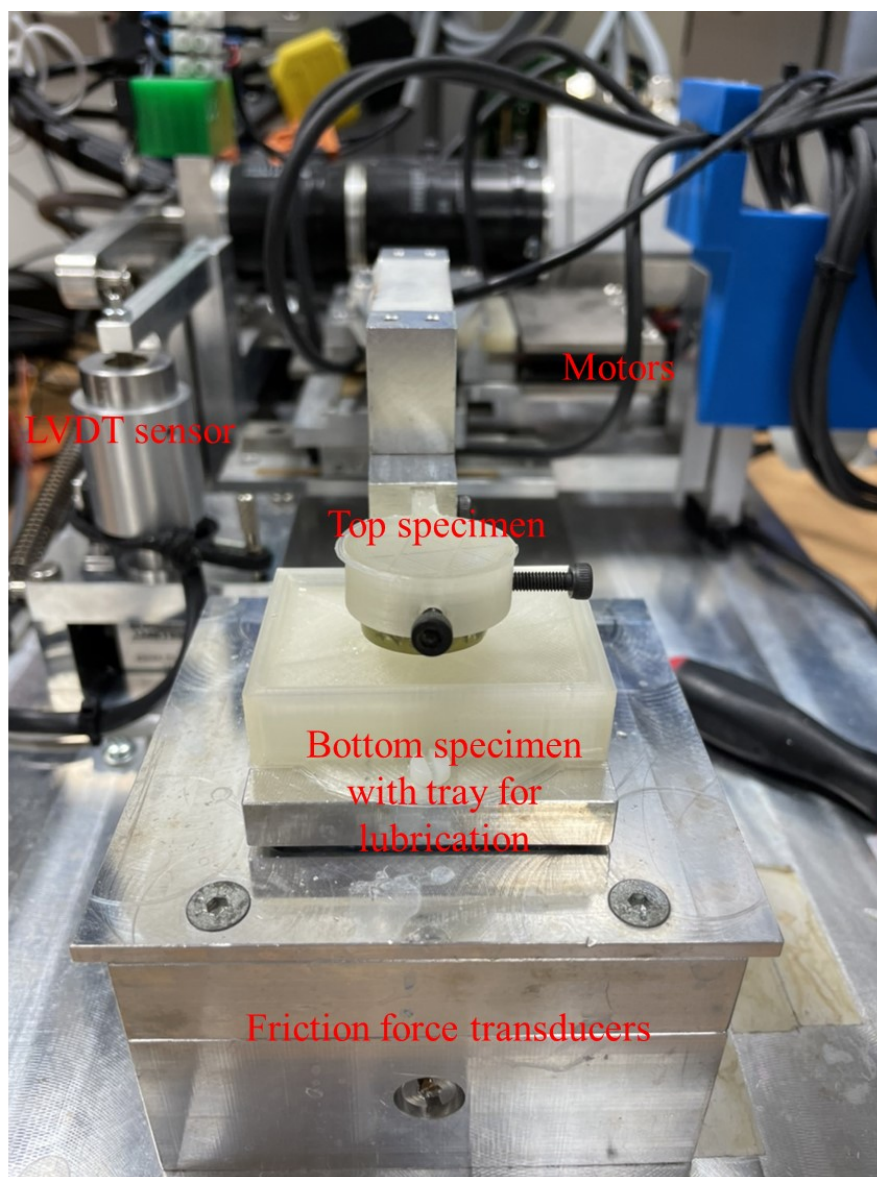


Figure 6.5 The purpose built Bio-Tribology Machine (BTM) was used to conduct tribology test for hybrid to against bovine cartilage, the linear motion was controlled by

linear variable displacement transducers (LVDT) and motor. The friction force was recorded and the friction coefficient calculated.

6.2.7. Cell studies

The cytotoxicity test was performed using 3-[4,5-dimethylthiazol-2-yl]-2,5-diphenyl tetrazolium bromide (MTT) cell viability assays and detail steps mentioned in pervious study [150], which evaluated the activity of mitochondrial enzymes, in accordance to the ISO 10993-5 standard - Biological evaluation of medical devices. The Saos-2 human osteosarcoma cells display several human osteoblastic features which were chosen for all studies at a concentration of 5×10^4 cells/mL. The dissolution product of hybrids or hybrid and titanium gyroid constructs were prepared in basal media. B/C is blank and control for only α -minimum essential medium (α -MEM), non-toxic negative control was medical grade polyethylene (PE), toxic positive control was polyurethane (PU) containing 0.1% zinc diethyldithiocarbamate (ZDEC), titanium gyroid scaffold is labelled as Ti, hybrid is labelled as Hyb, and Hybrid and gyroid construct is labelled as Ti-Hyb in the MTT study.

In order to observe the cell attachment behaviour on the samples. Samples were cut into 1 cm square size and washed using deionised water for 10 seconds three times. Hybrids and hybrid and gyroid scaffolds were placed in 70% of ethanol for 30 minutes for sterilisation and washed several times using culture media to prevent ethanol contamination. The sterilised samples were washed in fresh α -MEM with 100 U/mL penicillin and 100 mg/mL streptomycin three times. As prepared samples were placed into a 24-well plate (Corning, Thermoscience, UK) and concentrated Saos-2 cells were seeded to grow and attach directly on the surface of sample in incubator for 30 minutes

at 37°C, 5% CO₂ and 21% O₂ for 30 minutes initial stabilisation. After 30 minutes stabilisation, culture media was added to dilute the cell concentration to 5 x 10⁴ cells/mL then moved to incubator for 3 days. SEM was used to do surface observation. Cells were fixed on the surface of samples using gradient ethanol drying method. Samples were soaked into 50, 70, 90, and 98% of ethanol for 10 minutes and left in fume hood for air dry, respectively. The dried samples were observed the surface morphology using SEM and the rest of steps were mentioned in Chapter 3.4.2.

Alkaline phosphatase assay (ALP) was used to evaluate osteoblast activity by testing expression of ALP, a by-product of osteoblast, an indicator of osteoblastic activity. Saos-2 cells were cultured on titanium gyroid scaffolds and hybrids for 3, 7, 10, 14 and 21 days, supernatant was collected and alkaline phosphatase (ALP) activity was measured using a colourimetric p-nitrophenyl phosphate (pNPP) assay kit (Abcam, ab83369) following manufacturer instructions. Samples were reacted with 5 mM pNPP solution for 60 min at 25 °C. The reaction was stopped with Stop Solution provided in the kit and output was determined using a microplate reader at optical density 405 nm. pNPP standard curve was determined by reacting assay buffer containing 0, 4, 8, 12, 16 and 20 nmol with 5mM pNPP and ALP enzyme.

6.3. Results and discussion

6.3.1. The hybrid and gyroid scaffold optimisation

. The hybrid and gyroid scaffold optimisations are based on the drying methods and the composition of hybrid which is demonstrated in Figure 6.6.

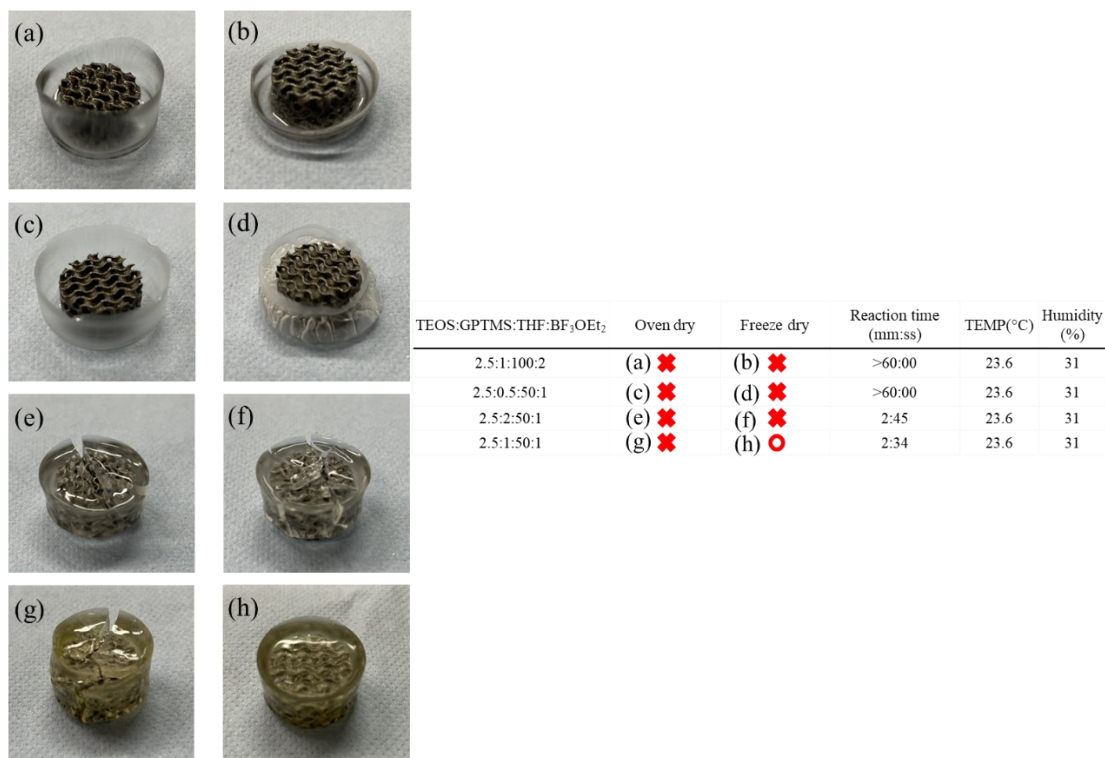


Figure 6.6 The optimisation of hybrid and gyroid scaffold integration. The (a-h) in left are the synthesis results and the (a-h) in right table are corresponding to the left image results. Red X means failure synthesis and red O is success synthesis. (Gyroid scaffold diameter is 16 mm)

Hybrid is a bouncy material compared with titanium gyroid scaffold also hybrid has significant shrinkage as mentioned in Chapter 4.3.1. The shrinkage was about 80% in volume which brings huge challenge for their integration, especially, since the titanium gyroid scaffold has no shrinkage. This significant shrinkage difference produced internal stresses for crack propagation. Figure 6.6 (a-d) demonstrate incomplete shapes and uneven shrinkage and the table lists the synthesis conditions. Figure 6.6 (e-g) demonstrates crack formation. Figure 6.6 (h) is the optimised composition for hybrid and gyroid scaffold synthesis. Further optimisation is shown in Figure 6.7 is based on hybrid thickness and the THF:GPTMS ratio. The ratio of TEOS:GPTMS:THF: BF₃ · OEt₂ was 2.5:1:50:1. Further synthesis optimisation was

needed. The left images suggested the optimised hybrid thickness was about 4 mm. However, thickness less than 4 mm was insufficient for further mechanical tests. If the thickness was higher than 4 mm risk of cracking was high on the edge of hybrid. The right images suggested the optimised hybrid THF:GPTMS ratio was 50:1. If the ratio was higher than 50:1, polymerisation may not complete. If the ratio was lower than 50:1, the polymerisation was too fast to let bubbles escape from the hybrid. If they remain, they will significantly reduce the mechanical properties of hybrid. Thus, the best hybrid condition in this study is based on the ratio of TEOS:GPTMS:THF: $\text{BF}_3 \cdot \text{OEt}_2$ is 2.5:1:50:1 with 4 mm thickness.

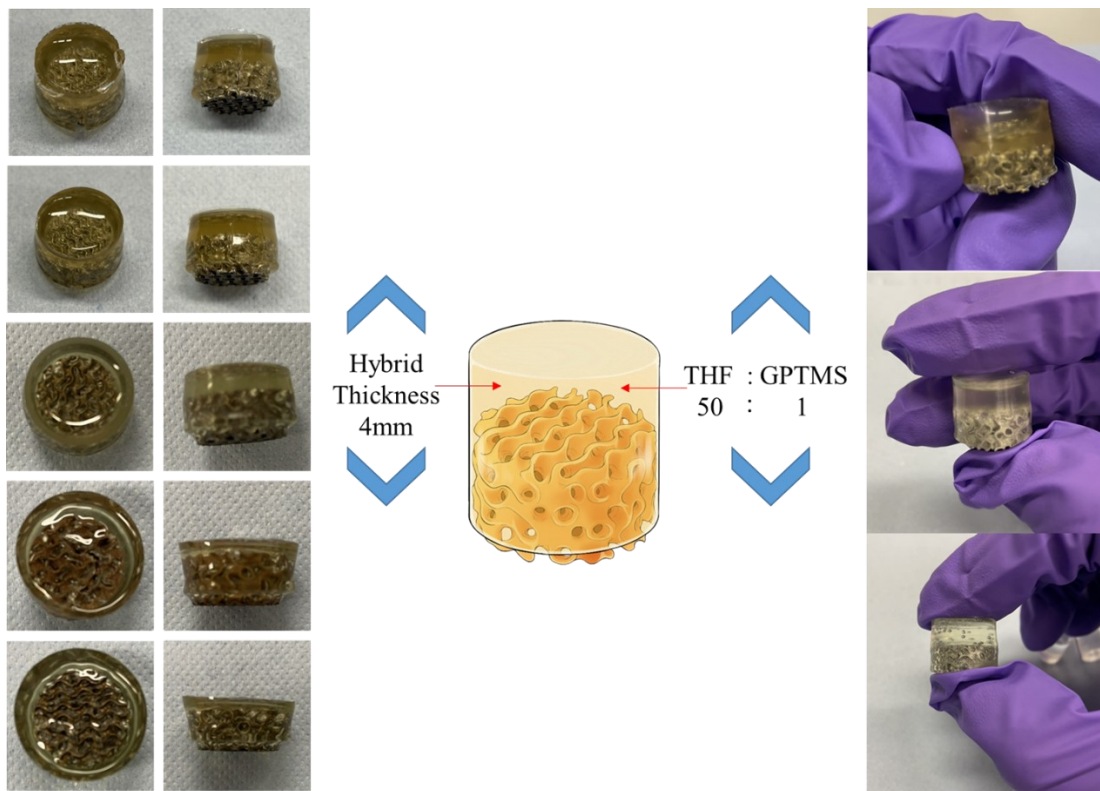


Figure 6.7 The optimisation of hybrid and gyroid scaffold based on the thickness and THF:GPTMS ratio.

6.3.2. μCT for hybrid and gyroid structure observation

The μ CT images of hybrid and gyroid scaffold internal structure were analysed using Ilastik software shown in Figure 6.8. Figure 6.8 (a-c) shows 2D slices in the Z, Y, and X directions, with hybrid in pink, gyroid in blue, and empty space in yellow. The light grey colour is hybrid and white colour is gyroid. Due to difference in attenuation of the materials (Figure 6.8 (d)), there is still some black line pattern artefacts, as shown in Figure 6.8 (a-c) [151, 152]. Ilastik software was used to distinguish hybrid, gyroid, and empty spaces from the images to minimise interferences as shown in Figure 6.9 (a). The porosity of gyroid scaffold was calculated using ImageJ script plugin as shown in Figure 6.9 (b). The porosity was 72.26% compared with Rhinoceros designed porosity of about 79.81% which has about 7.55% difference between designed and manufacturing object. This difference commonly caused while the SLM manufacturing. The SLM manufacturing uses high power laser to melt CP-Ti powder and fuse Ti powder together. Thus, laser focus change can affect final printing object by changing plate height, spot size, energy density at melt pool [153]. Overall printing quality is good and there is no obvious discontinuous parts or damage in the scaffold. The pore size distribution is shown in Figure 6.9 (c) and the average channel width was about 1.35 ± 0.21 mm.

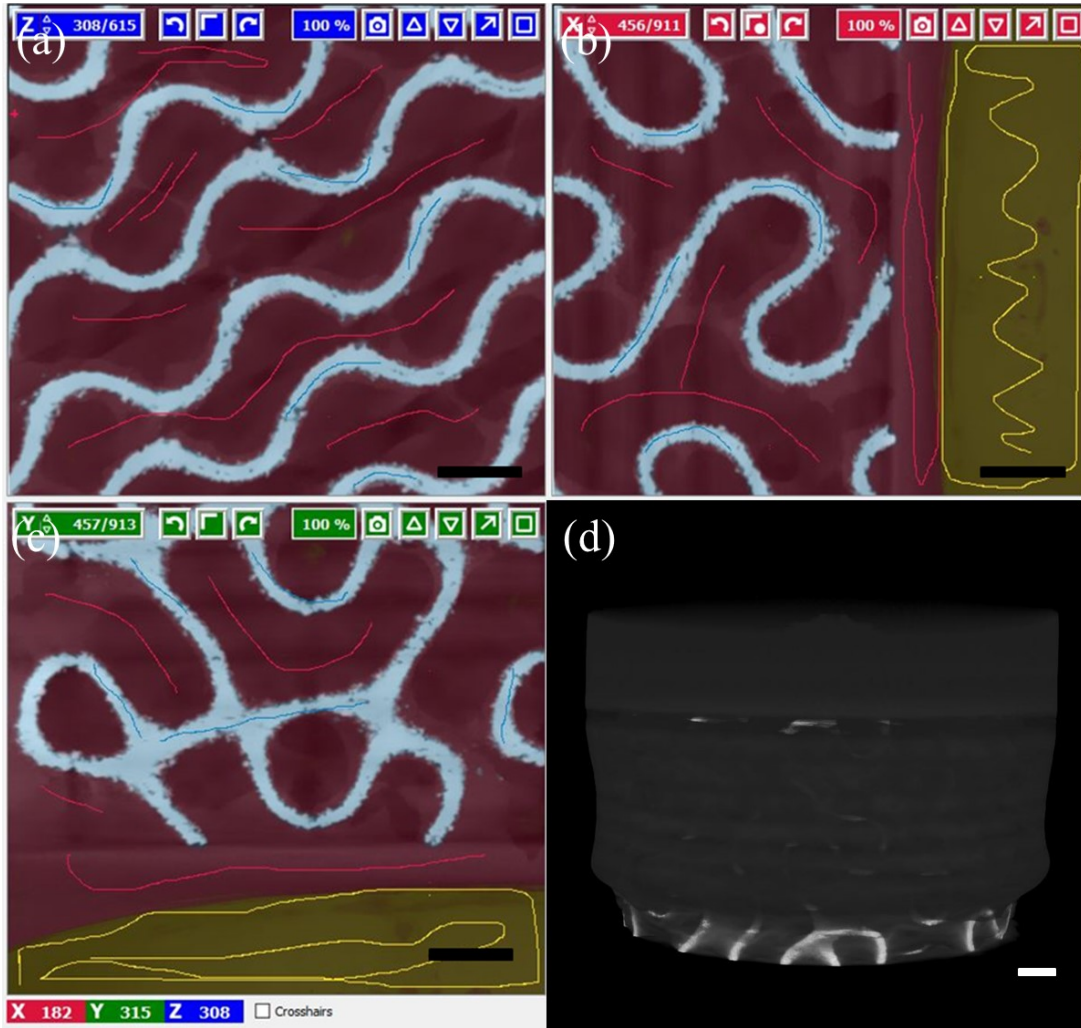


Figure 6.8 μ CT images of hybrid and gyroid scaffold using Ilastik software to distinguish hybrid, gyroid, and empty spaces which are (a) Z, (b) Y, (c) X views of μ CT images, and (d) 3D reconstructed hybrid and gyroid scaffold. (Pink area is defined as hybrid, blue area as gyroid, and yellow area is empty space) (Scale bar is 1.5 mm)

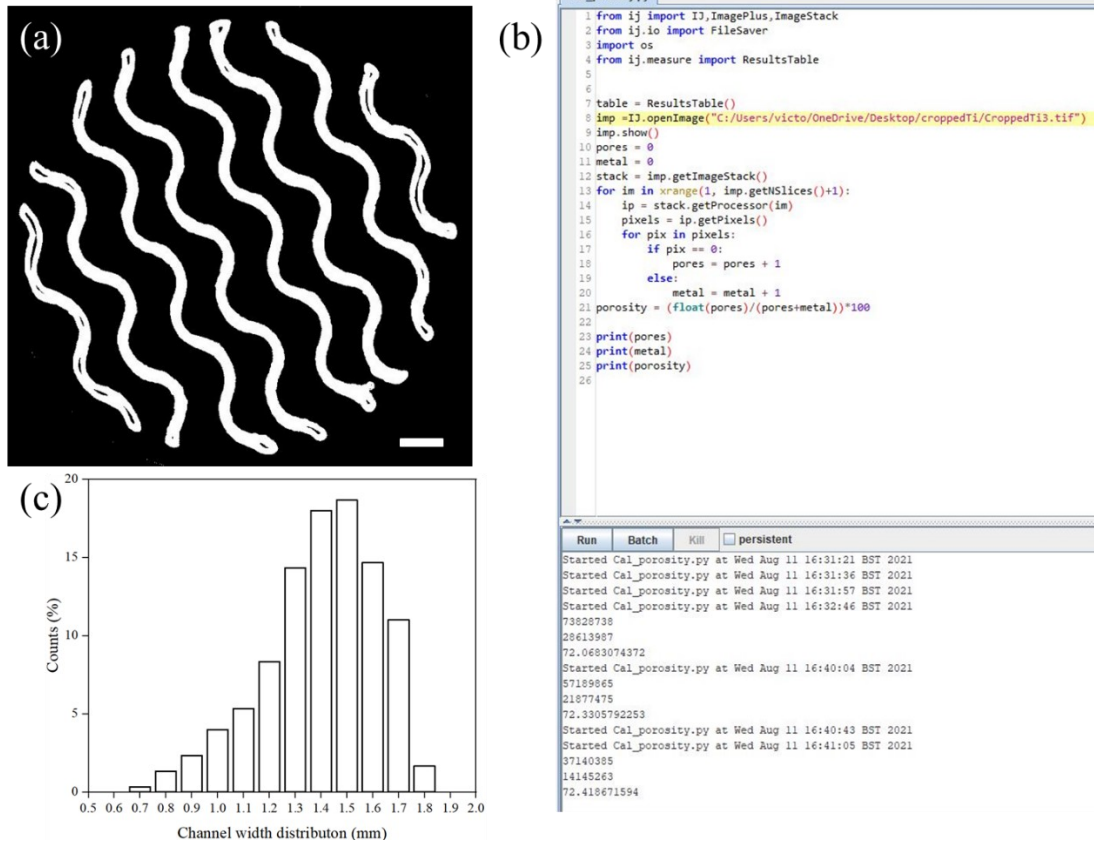


Figure 6.9 μ CT image analysis: (a) optimised scaffold thresholding using Ilastik software, (b) using ImageJ script to calculate porosity of scaffold based on the μ CT images, and (c) channel width distribution calculated using ImageJ to calculate 300 pores. (Scale bar is 1.5 mm)

6.3.3. SEM for hybrid and gyroid scaffold interface observation

μ CT is a non-destructive visualisation method for internal structure observation. However, the resolution is not high enough for the interface observation. SEM technique is used to determine how well the hybrid has penetrated and integrated into the porous Ti, particularly interface observation at micrometre scale. Figure 6.10 (a) shows the edge of hybrid and gyroid scaffold which has only gyroid scaffold. Individual Ti particles have been fused together in SLM manufacturing. The line pattern is shown

on the titanium surface which is caused by saw while cutting process. Figure 6.10 (b) shows the location of the hybrid and gyroid scaffold of the SEM images which are including titanium only, internal hybrid and gyroid interface, and outer interface. Figure 6.10 (c) has hybrid and gyroid central area. The cracks around the titanium are caused by cutting as shown in every area. The hybrid did not fully fill the gyroid pores, leaving many irregular cavities. However, there are some good interconnected interfaces displayed in some areas. The synthesis process used capillary action to make hybrid solution fill into the scaffold autonomously instead of applying any other external pressures to force the hybrid solution wicking in the gyroid scaffold. On the contrary, the peripheral area suggested good hybrid and gyroid scaffold interface. The two materials blended very well even though some small pores were incompletely filled. It is still demonstrated good interaction between interfaces, such as wetting.

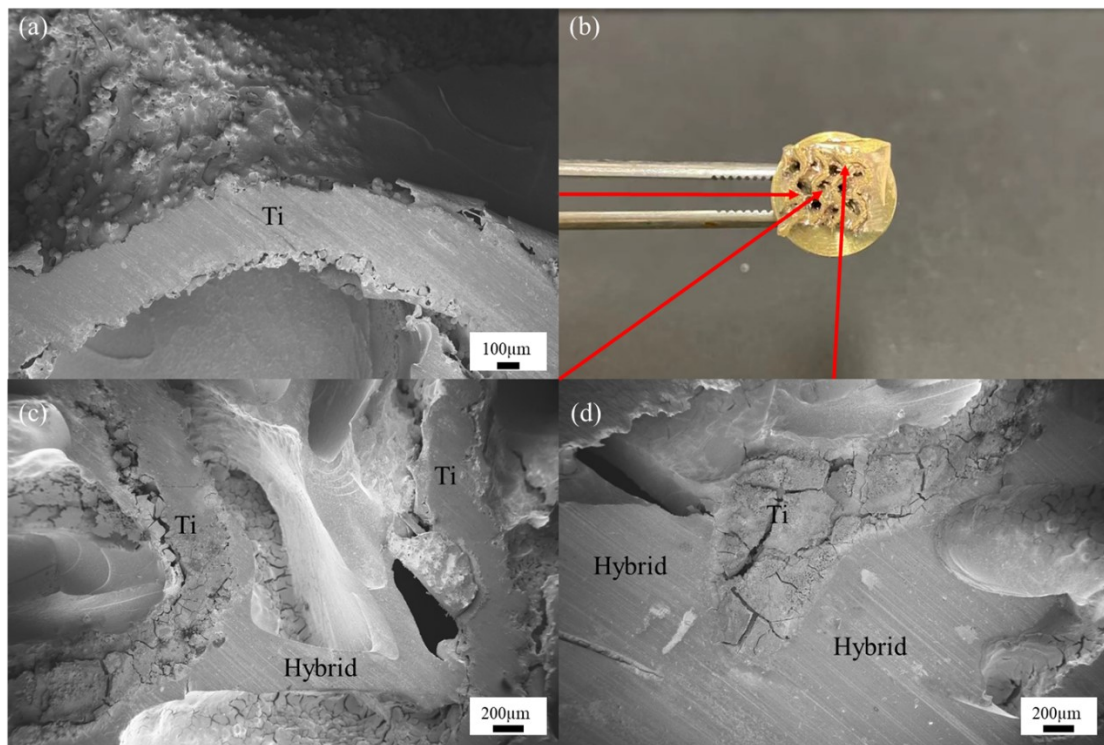


Figure 6.10 SEM images of hybrid and gyroid scaffold join surfaces (a) gyroid Ti scaffold only; (b) location of SEM images (SEM specimen stub with 12.5 mm

diameter.); (c) inner region of hybrid integration into the Ti scaffold; (d) outer region of hybrid integration into the Ti scaffold.

6.3.4. *Mechanical properties of hybrid and gyroid scaffold*

Knee meniscus is responsible for very complex biomechanical properties in the knee joints, including distribution of the force across the knee, withstand different forces in different directions, protection of the underlying cartilage, lubrication of the cartilage surfaces, and joint stability [154]. Unconfined compression test is a common test method for meniscus. According to Joshi et al., compressive biomechanical testing results from human menisci, showed the aggregate modulus of human menisci to be about 0.22 MPa [155]. There are many reports focused on the human meniscus compressive testing which are 0.01 to 1.7 MPa with 3 to 20% of strain in compressive modulus by many different conditions [156-159]. The hybrid and gyroid scaffold demonstrated higher compressive strength than previous reports in compression test as shown in Figure 6.11. The average compressive stress was 5.21 ± 1.67 MPa and the minimum strain tolerance is about 20% of strain as shown in the compression pattern. This result suggests hybrid and gyroid scaffold has sufficient compressive strength for meniscus replacement.

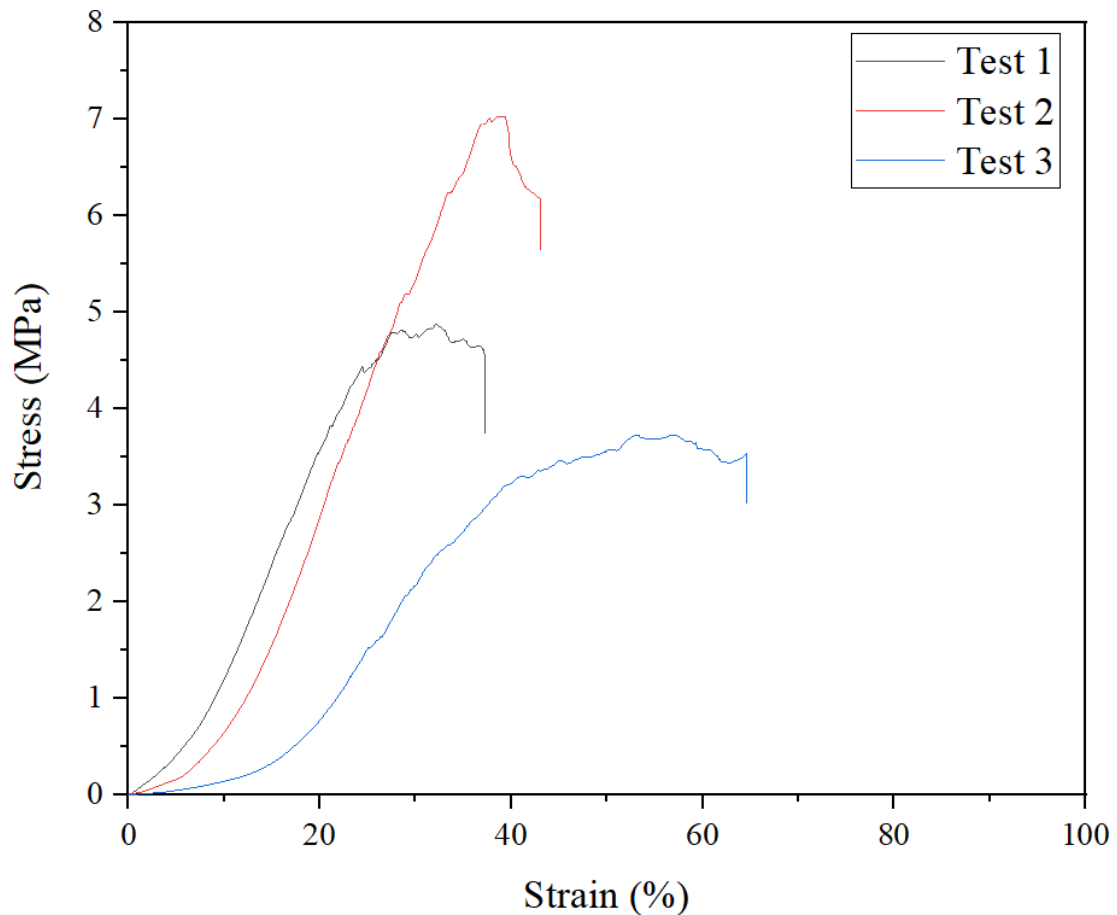


Figure 6.11 Compression tests of hybrid and gyroid scaffold with 9 N preload and 1 mm/min compressive rate.

Another important biomechanical property is shear stress of meniscus. Tuijthof et al.'s previous studies reported human meniscal shear stress in total 31 measurements. The measurements were performed using hollow tubes with a 0.125 and 0.15 mm cutting edge also 33 and 37 N as starting force. The minimum and maximum shear stresses are 4.7 to 9.3 MPa [160]. The shear testing results are shown in Figure 6.12. The shear strength of hybrid and gyroid scaffold interface was 6.39 ± 0.96 MPa and the minimum strain tolerance was about 9% of strain as shown in the shear pattern.

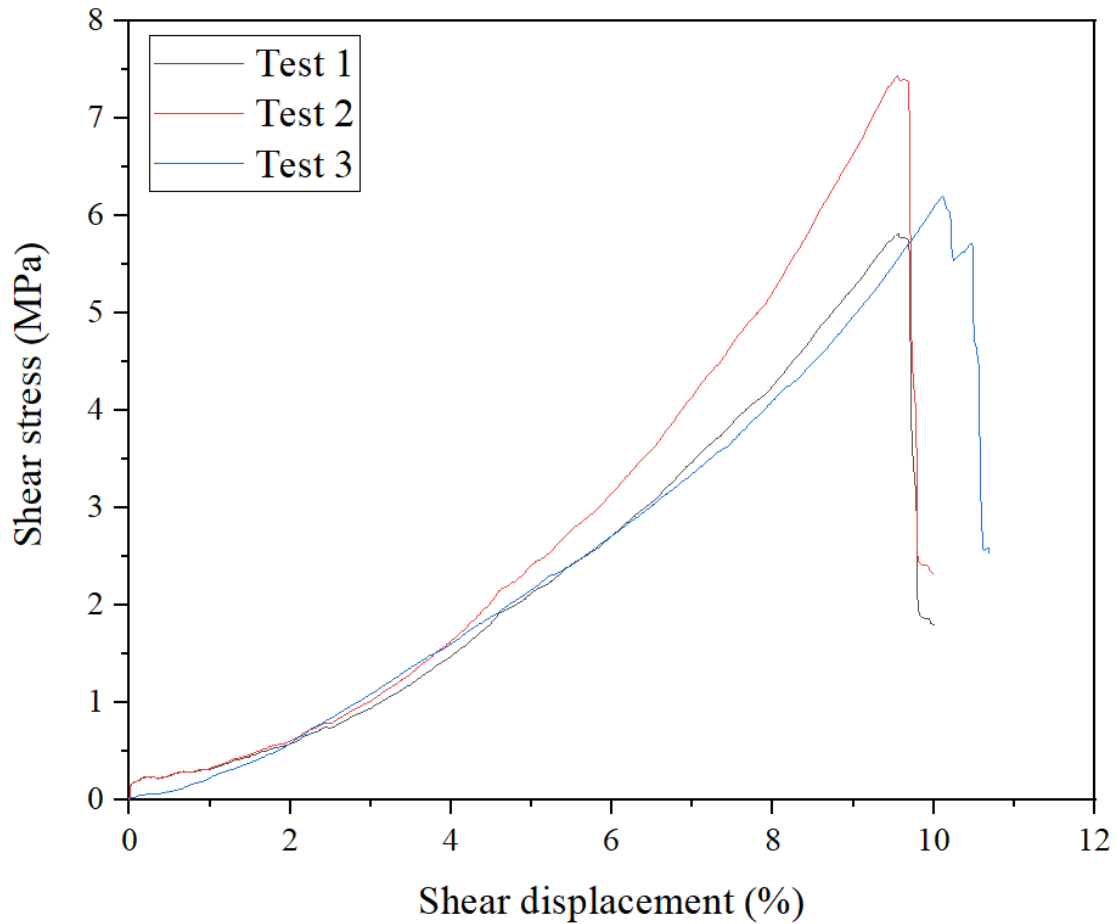


Figure 6.12 Shear test of hybrid and gyroid scaffold interface with 9 N preload and 1 mm/min shear rate.

In order to understand the reliability for the hybrid and gyroid scaffold *in-vitro* in the wet condition which is conducted cyclic loading tests on the same scaffold for soaking in PBS and performed 10^4 cycles cyclic test for day 0, 1, 7, 14, 30, 60, and 90, respectively. The cyclic test results have been shown in Figure 6.13. The cyclic loading patterns demonstrated similar response and no effect under PBS condition for 90 days test. This result indicates that hybrid and gyroid has good mechanical stability *in-vitro* over 10^4 cycles cyclic test.

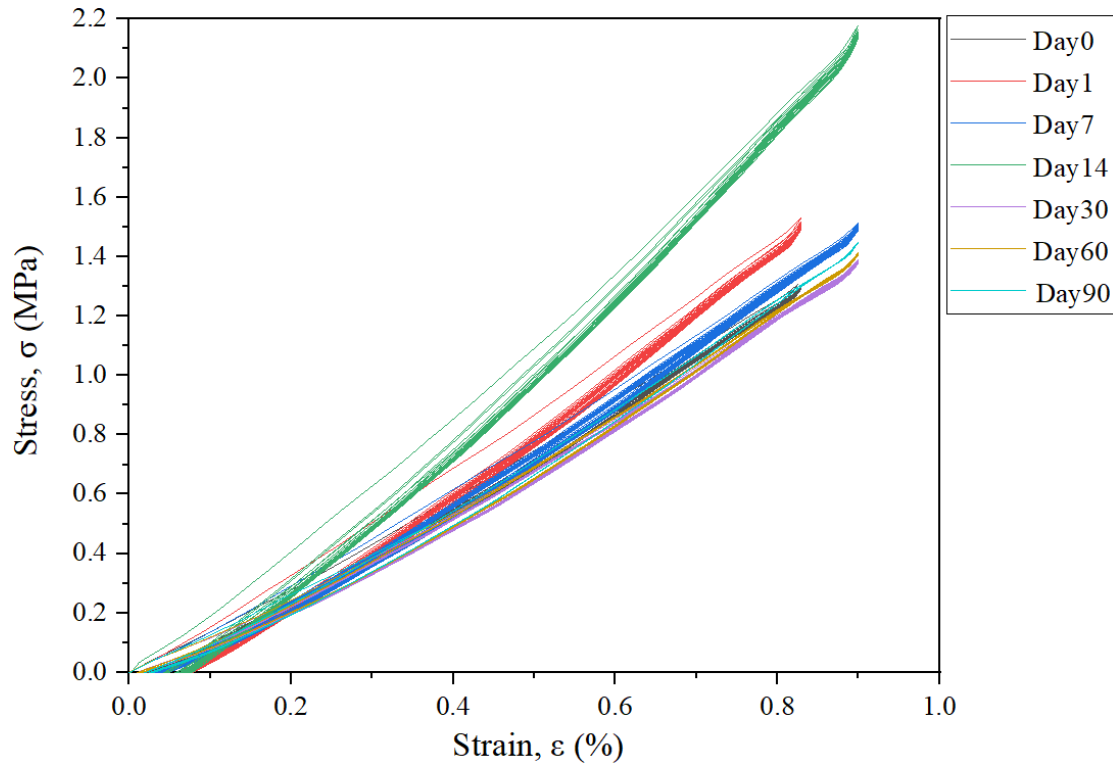


Figure 6.13 Cyclic test of hybrid scaffold for 90 days in-vitro stability evaluation. Every 100 cycles of 10^4 are shown.

6.3.5. Tribology test of hybrid and gyroid scaffold against cartilage

Wear debris cause significant problems for joint replacements, such as inflammation, osteolysis, and implant loosening [162]. Lower friction coefficient can minimise the generation of wear particles and improving bearing surface life [163]. The friction coefficient patterns of different materials against knee cartilage have been shown in Figure 6.14. And the average friction coefficients of sample sliding on cartilages at 5 cycle and 600 cycle have been shown in Figure 6.15. Figure 6.14 (a) demonstrated cartilage against cartilage which is has consistent friction pattern and the average friction coefficients at 5 and 600 cycle are 0.106 ± 0.066 and 0.101 ± 0.067 . Figure 6.15 (b) shows hybrid against cartilage friction pattern. The pattern suggests the friction coefficient increased at initial stage and stabilise after 100 cycles. Thus, the

average friction coefficients at 5 and 600 cycle were 0.133 ± 0.062 and 0.109 ± 0.006 . Figure 6.15 (c) demonstrated UHMWPE against cartilage friction pattern. The pattern suggests the average friction coefficient increased at initial stage and stabilise after 400 cycles. The average friction coefficients at 5 and 600 cycle are 0.473 ± 0.019 and 0.776 ± 0.017 . According to Maksimkin et al. the coefficients of friction for UHMWPE based samples are higher than adult dog cartilage of Bullmastiff breed in distilled water medium at all times [143]. The friction coefficient of knee cartilage ranged from 0.055 to 0.026 compared with UHMWPE which was 0.12 to 0.087. UHMWPE has about 218% to 334% higher friction coefficient than dog knee cartilage before and after 4 km run test [143]. According to Chan et al., UHMWPE friction coefficient against bovine knee cartilages in PBS for 60 minutes test were 0.391 ± 0.012 and the steady-state friction coefficients of near 60 minutes was about 0.46 [144]. In the natural joint, the friction coefficient of articular cartilage with synovial fluid is 0.01. However, the synovial fluid is not fully regenerated. The friction coefficient 0.1 is relatively low in the articular cartilage material [145]. In terms of hybrid and gyroid scaffold, the average friction coefficient at 5 and 600 cycle were about 0.133 ± 0.062 and 0.109 ± 0.006 , about 125% to 107% higher than bovine knee cartilage. As patients undergoing knee arthroplasties tend to be younger and high-mobility [146], for artificial knee cartilage replacement, lower friction is not only reduced wear particle formation also decreased unwanted stress generation to damage peripheral tissues and cartilage to preserve natural cartilage [164, 165].

An ideal meniscus replacement should not damage intact surrounding natural knee cartilage. Tribology test is interacting surface measurement to reveal the effect of contact motion to the surfaces. Hybrid and gyroid scaffold demonstrated a similar average friction coefficient with bovine knee cartilage. It is crucial for the hybrid and gyroid scaffolds to have the potential to be a meniscus replacement implant.

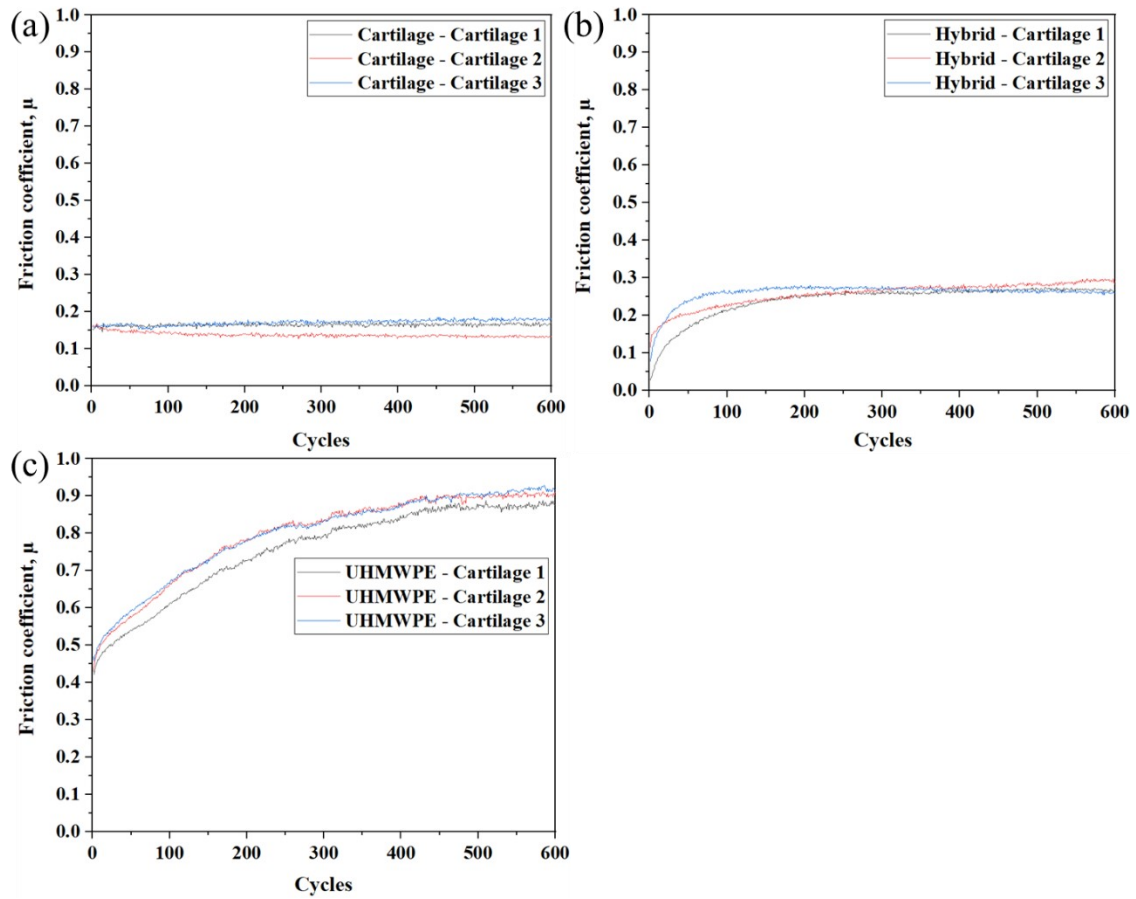


Figure 6.14 Friction coefficients of different materials sliding against knee cartilage versus time of sliding (a) cartilage against cartilage, (b) hybrid against cartilage, and (c) UHMWPE against cartilage using PBS as lubrication.

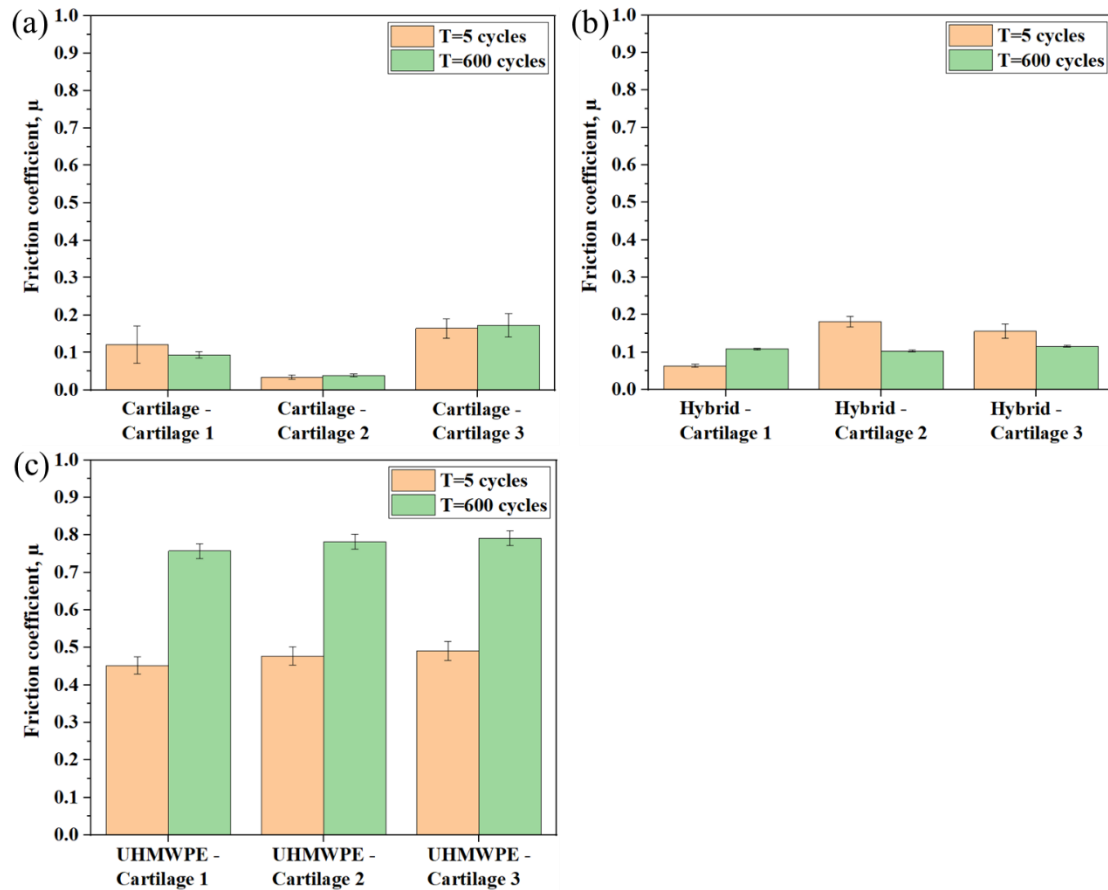


Figure 6.15 Average friction coefficients of tribology test results at 5 cycles and 600 cycles using PBS as lubrication: (a) cartilage against cartilage, (b) hybrid against cartilage, and (c) UHMWPE against cartilage.

6.3.6. Surface morphologies and roughness of samples

Surface conditions are important for the surface mechanical property evaluations. The surface morphologies of cartilage, hybrid, UHMWPE before and after tribology test are shown in Figure 6.16. Images suggested no significant difference before and after tribology test for all samples. The obvious hill-like surface features can be seen in the bovine knee cartilage as shown in Figure 6.16 (a) and (b). The hybrid surfaces were flat without obvious different in Figure 6.16 (c) and (d). The UHMWPE were flat

surfaces but there are some line patterns present in Figure 6.16 (e) and (f). Knee cartilage has different levels of surface feature such as higher curvature compared with hybrid and UHMWPE. Therefore, the hybrid and UHMWPE samples can be considered as non-migrating contact during tribology test. This non-migrating contact caused insufficient lubrication replenishment while the sliding test. This is the reason for increasing in the friction coefficient during tribology test [9, 144].

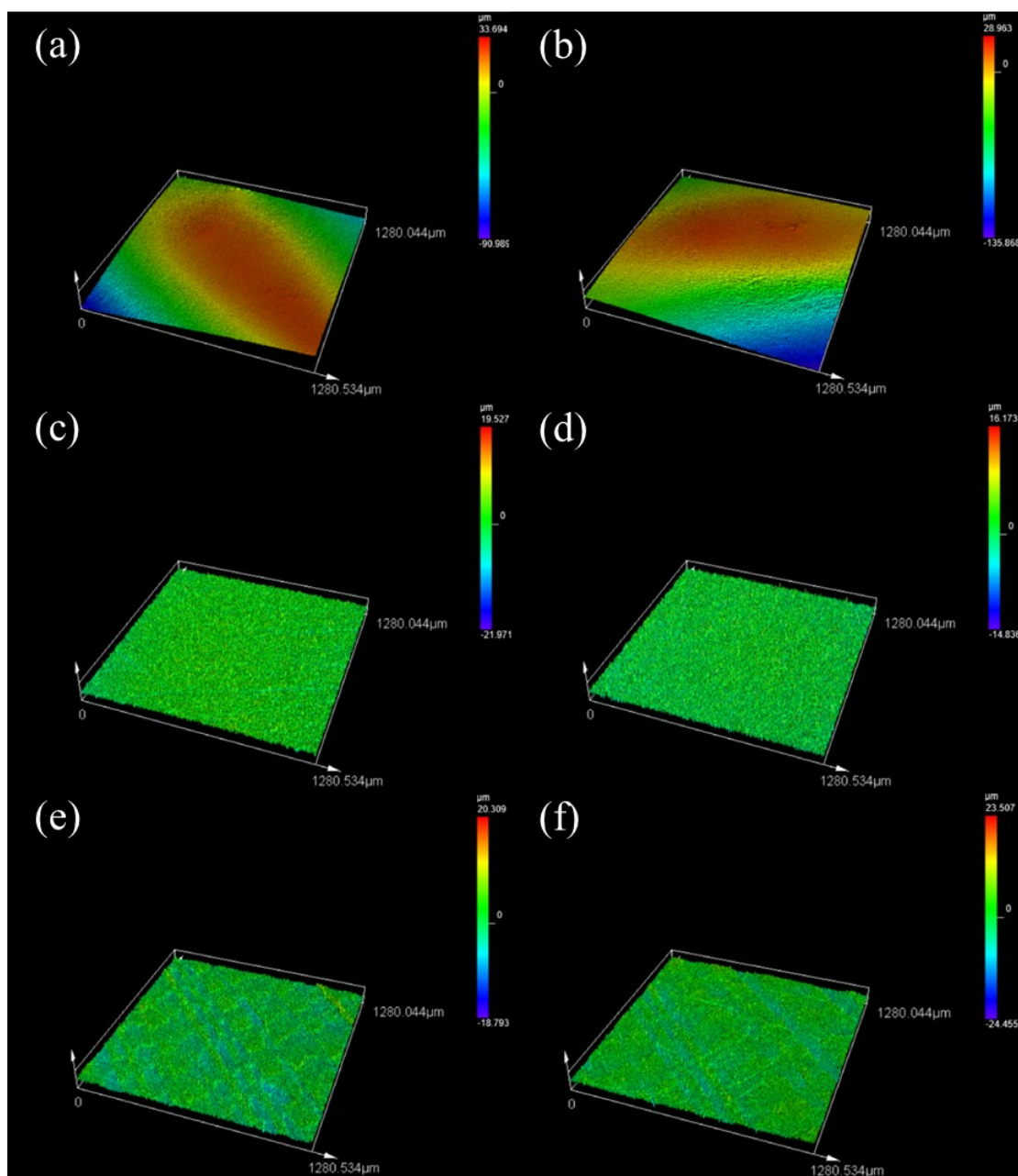


Figure 6.16 Surface roughness observations performed using confocal microscope. (a)

cartilage surface before testing; (b) cartilage surface after tribology testing cartilage against cartilage; (c) hybrid surface before testing; (d) hybrid surfaces after tribology test hybrid against cartilage; (e) UHMWPE surface before testing; (f) UHMWPE surface after tribology test by UHMWPE against cartilage.

The surface roughness of cartilage, hybrid, and UHMWPE are shown in Figure 6.17 before and after the tribology test. The knee cartilages were harvested from different places, angles, stress-bearing parts at the same knee. Therefore, the surface roughness distributions of bovine knee cartilage are relatively large compared with artificial materials as shown in Figure 6.17 (a). There are not significantly different in the surface roughness changed shown in the roughness results in Figure 6.17 (b) and (c).

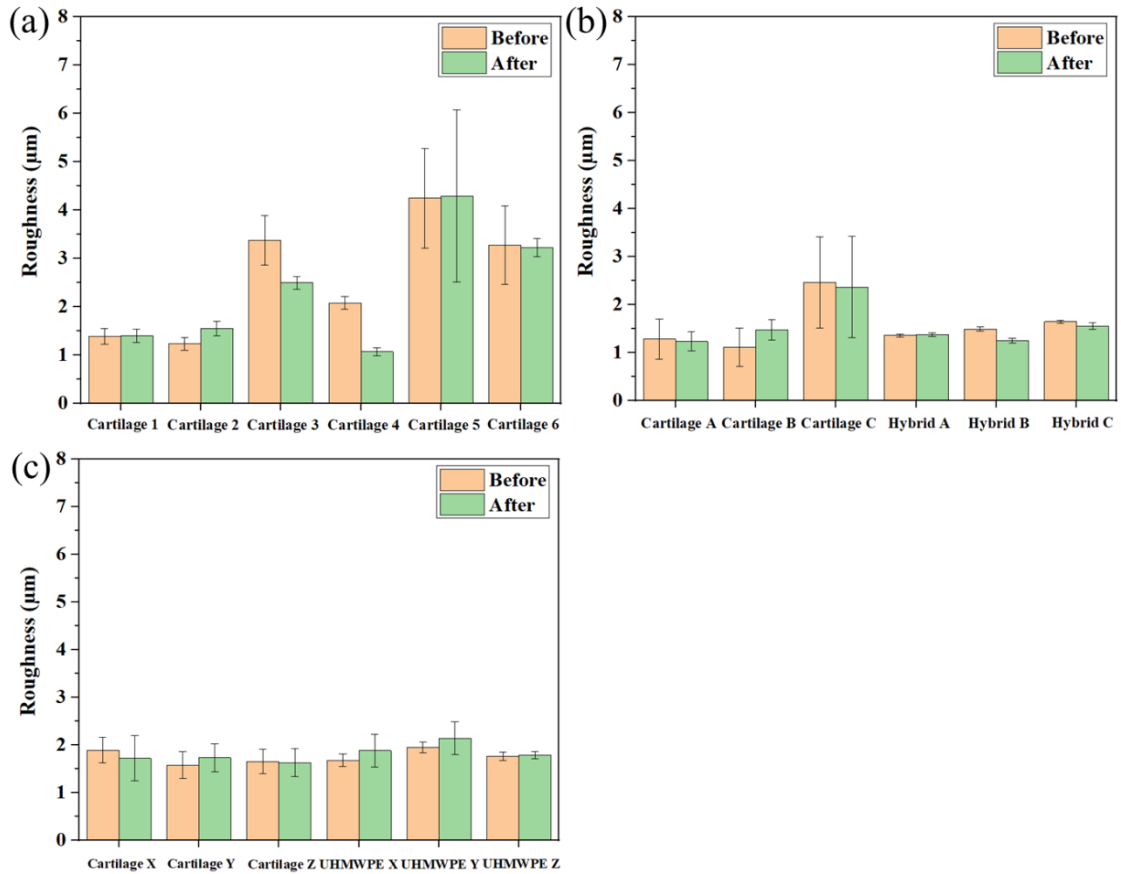


Figure 6.17 Surface roughness of tribology samples (a) before and after cartilage against cartilage in tribology test, (b) surface roughness changed by hybrids against cartilages, and (c) surface roughness changed by UHMWPE against cartilage in tribology test.

6.3.7. Cytotoxicity of hybrid and gyroid scaffold

The cell viability results are shown in Figure 6.18. The B/C is set as 100% of cell viability; PE is positive control also PU is negative control. Samples demonstrated high cell viabilities which are higher than 92.25% in the lowest sample as shown in 100% of Ti-Hyb sample. The extract solution passes the MTT test for non-cytotoxicity according to the ISO standard which cell viability greater than 70%. Thus, the hybrid and gyroid scaffolds have non-cytotoxicity that is potential to be used as implant

material.

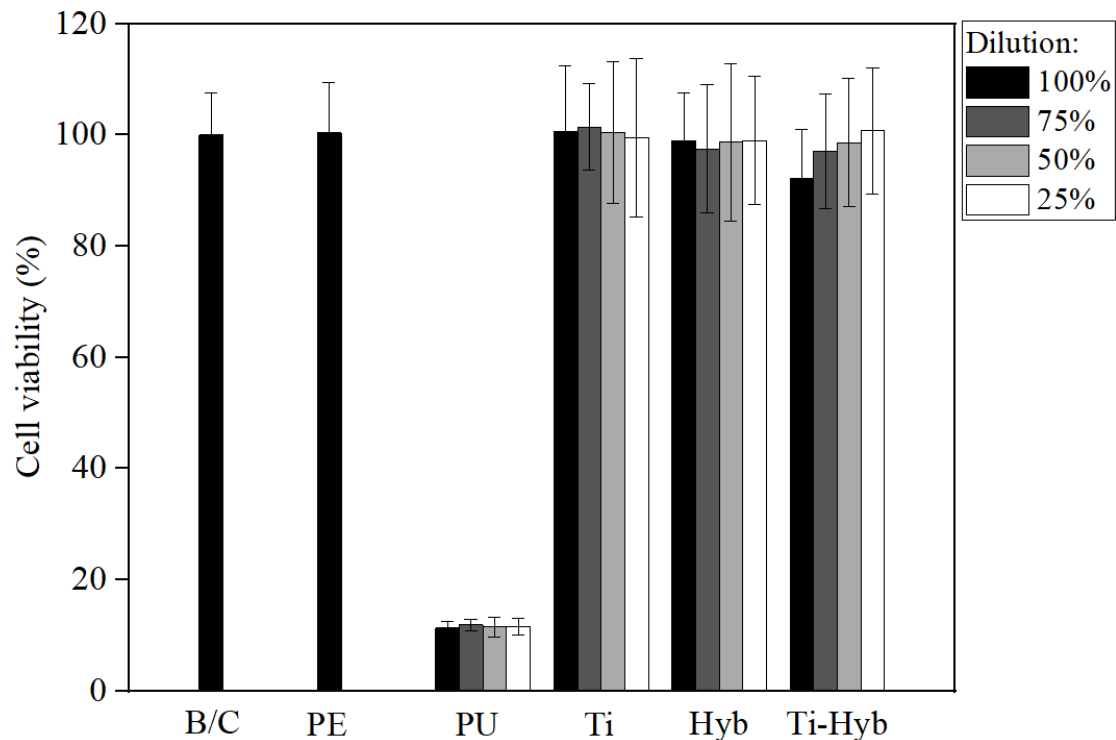


Figure 6.18 Cell viability test for all samples were performed using MTT cell viability assay. Saos-2 human osteosarcoma cells were co-cultured with sample media for 24 hours and measured cell viability. (B/C is blank and control, PU is used for non-toxic negative control, PU is used for toxic positive control, Ti is used titanium gyroid scaffold, Hyb is used hybrid scaffold, and Ti-Hyb is used hybrid and gyroid scaffold).

6.3.8. Cell attachment of hybrid and gyroid scaffold

Hybrid and gyroid scaffolds are designed to be the meniscus replacement implant. The hybrid surface has comparable mechanical properties to against cartilage with minimise damage in order to preserve natural cartilage as much as possible. On the other hand, the gyroid scaffold is designed as fixation mechanism at initial mechanical fixation also secondary biological fixation. Inner meniscus is bearing high compression

stress and shear strains which can lead to chondrocyte death and not suitable for cell survival [166]. On the contrary, the gyroid scaffold should allow cell attachment which can improve potential biological fixation. The SEM images demonstrated cell attachment behaviours on hybrid and gyroid surface as shown in Figure 6.19. Figure 6.19 (a) and (b) show Saos-2 cells attached on the titanium without any treatment. It is clear to observe filopodia and lamellipodia on the surface of titanium [167]. Filopodia act anchor cells to the surrounding materials which can promote lamellipodia formation and extension while cell migration on the materials [168]. The lamellipodia can wrap surrounding material materials and to robust cell adhesion on the material surface that is an key evident for the cell attachment and beginning of biological responses [169]. In the case of hybrid surface as shown in Figure 6.19 (c) and (d), the cell filopodia and lamellipodia are not clear to observe, and the cell tend to be flat indicating lower activity for cell spreading compared with titanium gyroid scaffold.

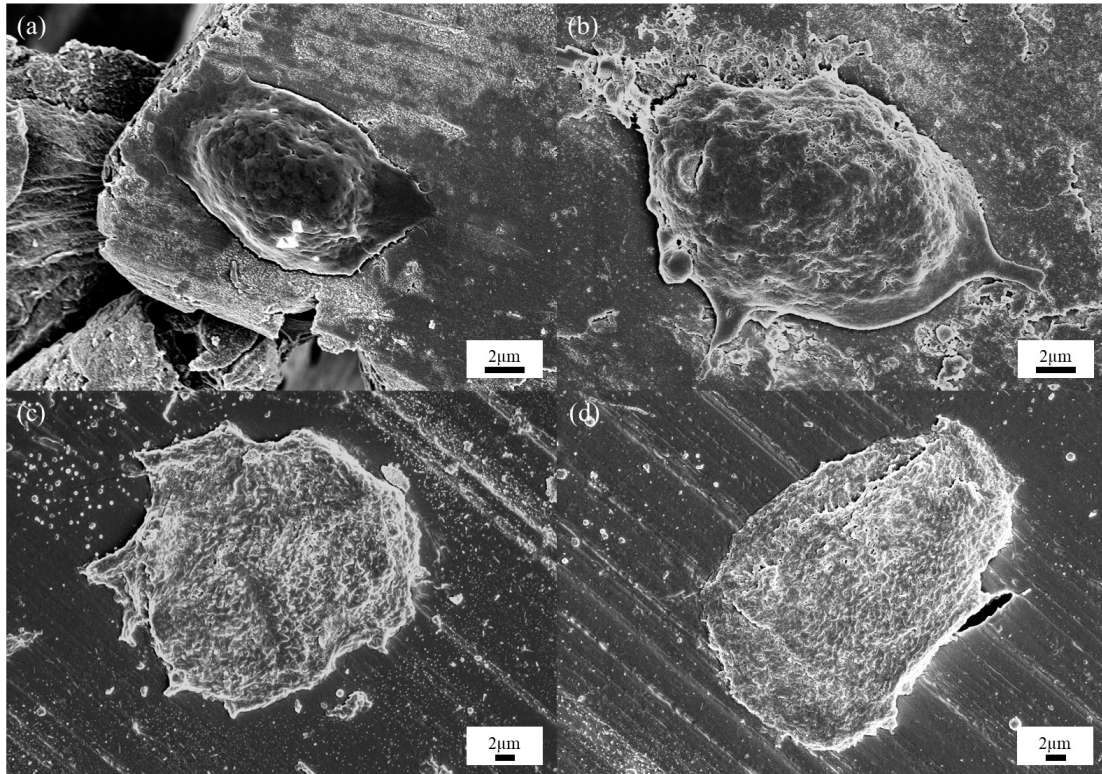


Figure 6.19 SEM images of Saos-2 cell attachment (a) and (b) are cell attached on the titanium surface and (c) and (d) are cell attached on the hybrid surface.

6.3.9. *ALP activity of hybrid and gyroid scaffold*

ALP activity assay was performed to determine osteogenic differentiation after 21 days of culture with samples. Enhanced ALP activity may lead to faster bone maturation around the implant, probably inducing better osseointegration [170]. The titanium gyroid scaffold is designed not only initial mechanical fixation also secondary biological fixation. Therefore, the ALP activity results delivered information for the gyroid scaffold as knee anchor application. The ALP results are shown in Figure 6.20. ALP activity of cells on the gyroid scaffold increased after 3 days culture and reached a maximum at day 10 and decreased after that. This occurred due to the Saos-2 cell migration and differentiation increased expression of ALP activity and decreased

because Saos-2 differentiated into mature osteoblasts [171]. On the contrary, ALP activity of cells cultured on hybrids suggested a slow increase, remaining low ALP activity for 21 days. The SEM images suggested clear filopodia and lamellipodia of cell spreading and migration on the surface of titanium. Furthermore, the 3D gyroid scaffold also supplied multiscale topographies. These factors potentially supported cell migration and stimulate cell differentiation to increase ALP activity [172, 173]. ALP activity results indicated that gyroid scaffold is suitable for Saos-2 cell to differentiate into mature osteoblasts that is potential to use for secondary biological fixation applications.

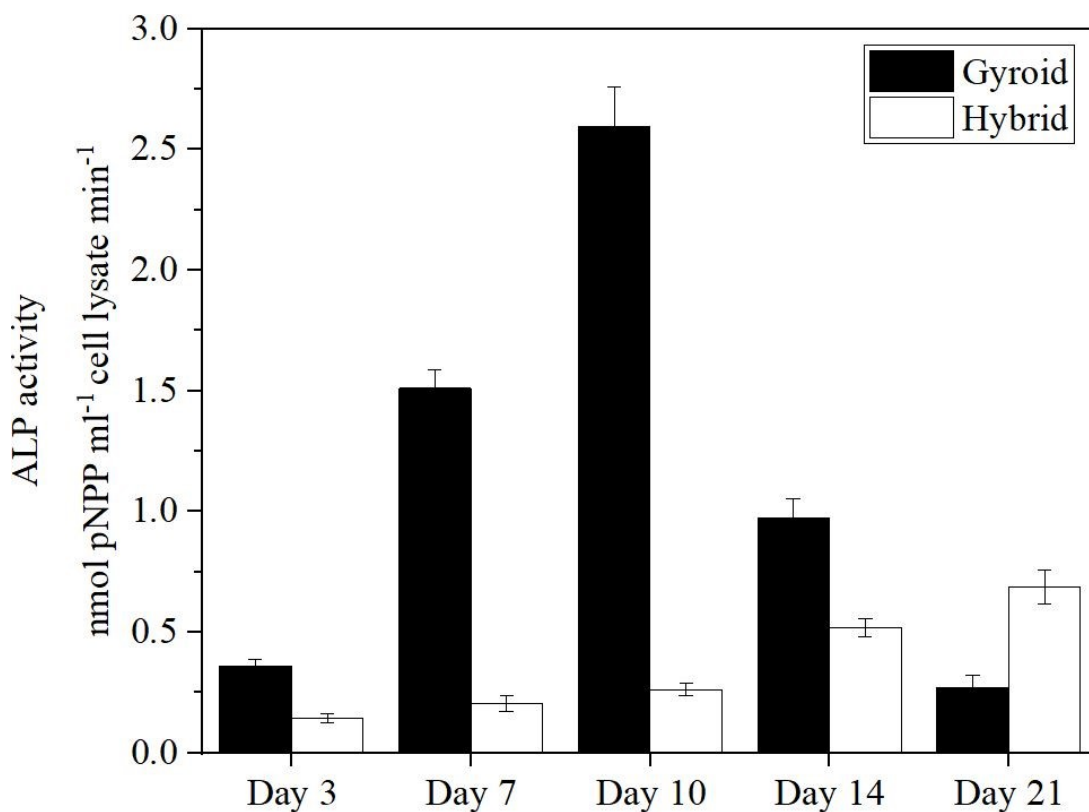


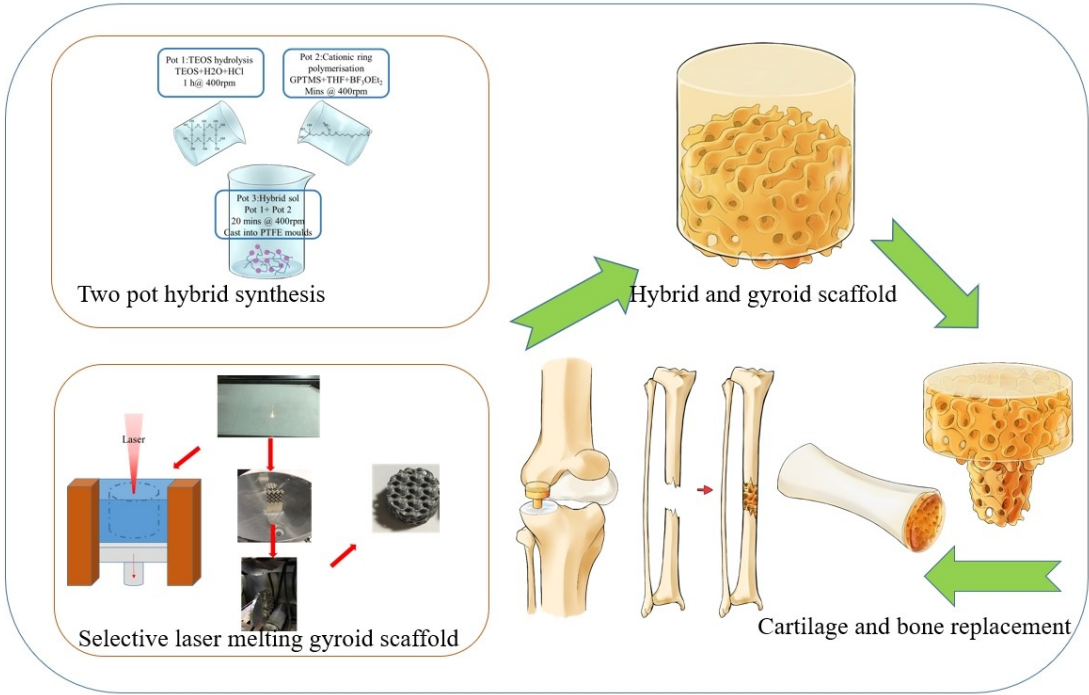
Figure 6.20 ALP activity test of titanium gyroid scaffold and hybrid for 21 days.

6.4. Conclusions

Hybrid and gyroid scaffolds have been successfully designed and manufactured. The scaffold optimisation was focused on the hybrid composition, manufacturing parameters, and synthesis conditions. μ CT was used to observe the inner structure of gyroid scaffold. Although, there are small scale differences between designed porosity and manufactured scaffold. The structural integration of the hybrid and the Ti was high without visible defects and broken pieces in the internal scaffold. However, the SEM images shown a low interaction between hybrid and gyroid in internal structure. The outer interface illustrated better interaction due to wicking of the hybrid sol. The scaffold demonstrated comparable mechanical properties to human meniscus and the tribology results indicated similar friction coefficient with bovine knee cartilage. Furthermore, the friction coefficient of hybrid and gyroid scaffold was significantly lower than UHMWPE. In terms of cell studies, higher than 90% cell viability was shown in each sample condition. The cell attachment and ALP expression was enhanced on the Ti gyroid scaffold, indicating it is suitable for secondary biological fixation of a hybrid meniscus implant. Based on research results, hybrid and gyroid scaffold can be potentially used for meniscus replacement application.

Chapter 7

Thesis conclusions and future work



7. Thesis conclusions and future work

7.1. Thesis conclusions

The objective of this thesis was to design and prepare a meniscus replacement device using SiO₂-PolyTHF hybrid. The hybrid has unique mechanical properties which can minimise the damage to opposing articular cartilage surfaces. The research started based on the biomimetic structural hybrid meniscus. But there were some problems such as high shrinkage during hybrid synthesis and fixation mechanism for the hybrid meniscus on the testing rig and further application. In order to solve these problems, μ CT and SLM techniques were used to conduct shrinkage factors measurement and providing new solution of 3D printed anchor for fixation mechanism and biological fixation.

The mould optimisation and titanium gyroid scaffold design and SLM technique were used for scaffold preparation. The next step was comprehensive study of the process variables to enable optimised hybrid synthesis. The hybrid was designed to combine with gyroid scaffold, therefore the hybrid optimisation was needed in terms of synthesis, performance in different environment and more understanding on the reliability and reproducibility in material preparation and the potential joint parameters with hybrid and gyroid scaffold. Multiple syntheses were done based on controlling compositions, drying methods and other environmental conditions. The solution state NMR was used to determine the chemical reaction and material characterisation techniques were used to evaluate composition, chemical bonding, mechanical properties, material morphologies and long term used reliability.

The final objective was to combine hybrid and gyroid to produce a prototype

meniscus. More than 50 times syntheses were performed during the hybrid and gyroid scaffold optimisation. Finally, the hybrid and gyroid scaffolds were made and conducted with series of material testing. The μ CT and SEM were used to observe the internal structure and surface morphology of scaffold. The compression, cyclic, and shear test were provided the information of scaffold strength for meniscus replacement application. The tribology test was used to evaluate the friction coefficient compared with bovine knee cartilage which suggested a similar friction coefficient of hybrid to bovine knee cartilage. Furthermore, cell viability, cell attachment and ALP test demonstrated high cell viability, cell attached on gyroid scaffold better than hybrid surface, and higher ALP activity on gyroid scaffold. The proof of concept about our original design that hybrid for acting as meniscus replacement with low friction coefficient to prevent damaging knee cartilage and gyroid acting as anchor for biological fixation due to good biological responses. Hybrid and gyroid scaffold has potential that can be used for meniscus replacement.

7.2. Future work

SiO₂-PolyTHF hybrid is a relatively new material, so different material combinations and compositions can be tested. The CP-Ti scaffold could be optimised with different porosity and architecture and chemical functionalisation to further suitable for hybrid and gyroid integration, manufacturing parameter optimisation, and biological responses.

For the hybrid, a further functionalisation is needed for more complex biological tissue replacement. The two-pot synthesis is combined organic and inorganic material as hybrid which brings more possibility for the functionalisation. More studies are

needed for the hybrid synthesis and optimisation for hybrid and gyroid scaffold manufacturing in order to prepare better scaffolds for meniscus replacement such as adding some bioactive component at the edge of hybrid meniscus to biomimetic the peripheral area of the meniscus. For the hybrid and gyroid scaffold, further treatment for material mismatch is needed for instant applying vacuum environment in the hybrid solution wicking to force the solution enter hybrid scaffold with higher density to improve material joining properties. The gyroid scaffold should be designed in multifunctional application to provide better join surface to hybrid and biological fixation anchor also fit the mould for whole device manufacturing.

8. References

- [1] E.A. Arendt, OKU Orthopaedic Knowledge Update: Sports Medicine 2, Amer Academy of Orthopaedic (1999).
- [2] J.L. Cook, The current status of treatment for large meniscal defects, *Clinical Orthopaedics and Related Research*® 435 (2005) 88-95.
- [3] M. Majewski, H. Susanne, S. Klaus, Epidemiology of athletic knee injuries: a 10-year study, *The knee* 13(3) (2006) 184-188.
- [4] L.S. Lohmander, P.M. Englund, L.L. Dahl, E.M. Roos, The long-term consequence of anterior cruciate ligament and meniscus injuries: osteoarthritis, *The American journal of sports medicine* 35(10) (2007) 1756-1769.
- [5] M. Englund, E.M. Roos, H. Roos, L. Lohmander, Patient-relevant outcomes fourteen years after meniscectomy: influence of type of meniscal tear and size of resection, *Rheumatology* 40(6) (2001) 631-639.
- [6] B.S. Lee, J.W. Chung, J.M. Kim, W.J. Cho, K.A. Kim, S.I. Bin, Morphologic changes in fresh-frozen meniscus allografts over 1 year: a prospective magnetic resonance imaging study on the width and thickness of transplants, *The American journal of sports medicine* 40(6) (2012) 1384-1391.
- [7] C.J. Wirth, G. Peters, K.A. Milachowski, K.G. Weismeier, D. Kohn, Long-term results of meniscal allograft transplantation, *The American journal of sports medicine* 30(2) (2002) 174-181.
- [8] F. Tallia, L. Russo, S. Li, A.L. Orrin, X. Shi, S. Chen, J.A. Steele, S. Meille, J. Chevalier, P.D. Lee, M.M. Stevens, L. Cipolla, J.R. Jones, Bouncing and 3D Printable Hybrids with Self-healing Properties, *Materials Horizons* 5 (2018) 849-860.
- [9] M. Parkes, F. Tallia, G.R. Young, P. Cann, J.R. Jones, J.R.T. Jeffers, Tribological evaluation of a novel hybrid for repair of articular cartilage defects, *Materials Science and Engineering: C*, 119 (2021) 111495.

- [10] A.J. Fox, F. Wanivenhaus, A.J. Burge, R.F. Warren, S.A. Rodeo, The human meniscus: a review of anatomy, function, injury, and advances in treatment, *J Clinical Anatomy* 28(2) (2015) 269-287.
- [11] K. Vadodaria, A. Kulkarni, E. Santhini, P. Vasudevan, Materials and structures used in meniscus repair and regeneration: a review, *BioMedicine*, 9(1) (2019).
- [12] E.A. Makris, P. Hadidi, K.A. Athanasiou, The knee meniscus: structure–function, pathophysiology, current repair techniques, and prospects for regeneration, *Biomaterials* 32(30) (2011) 7411-7431.
- [13] P.S. Walker, M.J. Erkman, The role of the menisci in force transmission across the knee, *Clinical orthopaedics and related research* (109) (1975) 184-192.
- [14] W. Thompson, F. Fu, The meniscus in the cruciate-deficient knee, *Clinics in sports medicine* 12(4) (1993) 771-796.
- [15] J.P. Smith III, G.R. Barrett, Medial and lateral meniscal tear patterns in anterior cruciate ligament-deficient knees: a prospective analysis of 575 tears, *The American journal of sports medicine* 29(4) (2001) 415-419.
- [16] J.H. Koenig, A.S. Ranawat, H.R. Umans, G.S. DiFelice, Meniscal root tears: diagnosis and treatment, *Arthroscopy: The Journal of Arthroscopic & Related Surgery* 25(9) (2009) 1025-1032.
- [17] B.T. Kelly, W. Robertson, H.G. Potter, X.-H. Deng, A.S. Turner, S. Lyman, R.F. Warren, S.A. Rodeo, Hydrogel meniscal replacement in the sheep knee: preliminary evaluation of chondroprotective effects, *The American journal of sports medicine* 35(1) (2007) 43-52.
- [18] E. Kon, C. Chiari, M. Marcacci, M. Delcogliano, D.M. Salter, I. Martin, L. Ambrosio, M. Fini, M. Tschon, E. Tognana, Tissue engineering for total meniscal substitution: animal study in sheep model, *Tissue Engineering Part A* 14(6) (2008) 1067-1080.

- [19] G.A. Paletta Jr, T. Manning, E. Snell, R. Parker, J. Bergfeld, The effect of allograft meniscal replacement on intraarticular contact area and pressures in the human knee: a biomechanical study, *The American journal of sports medicine* 25(5) (1997) 692-698.
- [20] J. Herwig, E. Egner, E. Buddecke, Chemical changes of human knee joint menisci in various stages of degeneration, *Annals of the rheumatic diseases* 43(4) (1984) 635.
- [21] M.A. Sweigart, K.A. Athanasiou, Toward tissue engineering of the knee meniscus, *Tissue engineering* 7(2) (2001) 111-129.
- [22] A.C. AufderHeide, K.A. Athanasiou, Mechanical stimulation toward tissue engineering of the knee meniscus, *Annals of biomedical engineering* 32(8) (2004) 1163-1176.
- [23] C.A. McDevitt, S. Mukherjee, H. Kambic, R. Parker, Emerging concepts of the cell biology of the meniscus, *Current Opinion in Orthopaedics* 13(5) (2002) 345-350.
- [24] J. Melrose, S. Smith, M. Cake, R. Read, J. Whitelock, Comparative spatial and temporal localisation of perlecan, aggrecan and type I, II and IV collagen in the ovine meniscus: an ageing study, *Histochemistry and cell biology* 124(3-4) (2005) 225-235.
- [25] H. V. D. Brachy, R. Verdonk, A. Verbruggen, D. Elewaut, P. Verdonk, Cell-based meniscus tissue engineering, *Topics in tissue engineering, Biomaterials and Tissue Engineering Group (BTE)2007*, pp. ch2_1-ch2_13.
- [26] W. Petersen, B. Tillmann, Collagenous fibril texture of the human knee joint menisci, *Anatomy and embryology* 197(4) (1998) 317-324.
- [27] T. Brindle, J. Nyland, D.L. Johnson, The meniscus: review of basic principles with application to surgery and rehabilitation, *Journal of athletic training* 36(2) (2001) 160.
- [28] E. Balint, C.J. Gatt Jr, M.G. Dunn, Design and mechanical evaluation of a novel fiber-reinforced scaffold for meniscus replacement, *Journal of Biomedical Materials Research Part A* 100(1) (2012) 195-202.
- [29] M. Chen, S. Gao, P. Wang, Y. Li, W. Guo, Y. Zhang, M. Wang, T. Xiao, Z. Zhang,

- X. Zhang, The application of electrospinning used in meniscus tissue engineering, *Journal of Biomaterials Science, Polymer Edition* 29(5) (2018) 461-475.
- [30] D.C. Fithian, M.A. Kelly, V.C. Mow, Material properties and structure-function relationships in the menisci, *Clinical orthopaedics and related research* (252) (1990) 19-31.
- [31] K. Lechner, M. Hull, S. Howell, Is the circumferential tensile modulus within a human medial meniscus affected by the test sample location and cross-sectional area?, *Journal of orthopaedic research* 18(6) (2000) 945-951.
- [32] M. Tissakht, A. Ahmed, Tensile stress-strain characteristics of the human meniscal material, *Journal of biomechanics* 28(4) (1995) 411-422.
- [33] M.Á. Ruiz-Ibán, J. Diaz-Heredia, E. Elías-Martín, S. Moros-Marco, I. Cebreiro Martinez del Val, Repair of meniscal tears associated with tibial plateau fractures: a review of 15 cases, *The American journal of sports medicine*, 40(10) (2012) 2289-2295.
- [34] M. Englund, A. Guermazi, D. Gale, D.J. Hunter, P. Aliabadi, M. Clancy, D. Felson, Incidental meniscal findings on knee MRI in middle-aged and elderly persons, *New England Journal of Medicine*, 359(11) (2008) 1108-1115.
- [35] A. Getgood, R.F. LaPrade, P. Verdonk, W. Gersoff, B. Cole, T. Spalding, International Meniscus Reconstruction Experts Forum (IMREF) 2015 consensus statement on the practice of meniscal allograft transplantation, *The American journal of sports medicine*, 45(5) (2017) 1195-1205.
- [36] R. Howell, N.S. Kumar, N. Patel, J. Tom, Degenerative meniscus: Pathogenesis, diagnosis, and treatment options, *World journal of orthopedics*, 5(5) (2014) 597.
- [37] I.F. Cengiz, H. Pereira, J. Espregueira-Mendes, J.M. Oliveira, R. Reis, T. Medicine, Treatments of meniscus lesions of the knee: current concepts and future perspectives, *Regenerative Engineering and Translational Medicine*, 3(1) (2017) 32-50.
- [38] J.H. Yim, J.K. Seon, E.K. Song, J.I. Choi, M.C. Kim, K.B. Lee, H.Y. Seo, A

comparative study of meniscectomy and nonoperative treatment for degenerative horizontal tears of the medial meniscus, *The American journal of sports medicine*, 41(7) (2013) 1565-1570.

[39] C.M. LaPrade, A. Foad, S.D. Smith, T.L. Turnbull, G.J. Dornan, L. Engebretsen, C.A. Wijdicks, R. LaPrade, Biomechanical consequences of a nonanatomic posterior medial meniscal root repair, *The American journal of sports medicine*, 43(4) (2015) 912-920.

[40] A.J. Krych, P.J. Reardon, N.R. Johnson, R. Mohan, L. Peter, B.A. Levy, M. Stuart, Sports Traumatology, Arthroscopy, Non-operative management of medial meniscus posterior horn root tears is associated with worsening arthritis and poor clinical outcome at 5-year follow-up, *Knee Surgery, Sports Traumatology, Arthroscopy*, 25(2) (2017) 383-389.

[41] A.F. Anderson, J.J. Irrgang, W. Dunn, P. Beaufils, M. Cohen, B.J. Cole, M. Coolican, M. Ferretti, R.E. Glenn Jr, R. Johnson, Interobserver reliability of the International Society of Arthroscopy, Knee Surgery and Orthopaedic Sports Medicine (ISAKOS) classification of meniscal tears, *The American journal of sports medicine*, 39(5) (2011) 926-932.

[42] M. Ochi, Y. Uchio, K. Okuda, N. Shu, H. Yamaguchi, Y. Sakai, R. Surgery, Expression of cytokines after meniscal rasping to promote meniscal healing, *Arthroscopy: The Journal of Arthroscopic & Related Surgery*, 17(7) (2001) 724-731.

[43] C.S. Dean, J. Chahla, L.M. Matheny, J.J. Mitchell, R. LaPrade, Outcomes after biologically augmented isolated meniscal repair with marrow venting are comparable with those after meniscal repair with concomitant anterior cruciate ligament reconstruction, *The American journal of sports medicine*, 45(6) (2017) 1341-1348.

[44] J.W. Griffin, M.M. Hadeed, B.C. Werner, D.R. Diduch, E.W. Carson, M. Miller, R. Research®, Platelet-rich plasma in meniscal repair: does augmentation improve

surgical outcomes?, *Clinical Orthopaedics and Related Research*®, 473(5) (2015) 1665-1672.

[45] J.M. Woodmass, R.F. LaPrade, N.A. Sgaglione, N. Nakamura, A. Krych, Meniscal repair: reconsidering indications, techniques, and biologic augmentation, *Journal of Bone and Joint Surgery*, 99(14) (2017) 1222-1231.

[46] J.Cho, r. research, A modified outside-in suture technique for repair of the middle segment of the meniscus using a spinal needle, *Knee surgery & related research*, 26(1) (2014) 43.

[47] Y.A. Fillingham, J.C. Riboh, B.J. Erickson, B.R. Bach Jr, A. Yanke, Inside-out versus all-inside repair of isolated meniscal tears: an updated systematic review, *The American journal of sports medicine*, 45(1) (2017) 234-242.

[48] E. Uzun, A. Misir, T.B. Kizkapan, M. Ozcamdalli, S. Akkurt, A. Guney, Factors affecting the outcomes of arthroscopically repaired traumatic vertical longitudinal medial meniscal tears, *Orthopaedic journal of sports medicine*, 5(6) (2017) 2325967117712448.

[49] A.J. Krych, P. Reardon, P. Sousa, B.A. Levy, D.L. Dahm, M. Stuart, R. Surgery, Clinical outcomes after revision meniscus repair, *The Journal of Arthroscopic & Related Surgery*, 32(9) (2016) 1831-1837.

[50] R.K. Martin, D. Leland, A.J. Krych, *Current Concepts in Meniscus Pathology and Repair*, *Lower Extremity Joint Preservation*, Springer (2021), pp. 119-132.

[51] A.B. Anderson, J. Gaston, L.E. LeClere, J. Dickens, Meniscal Salvage: Where We Are Today, *Journal of the American Academy of Orthopaedic Surgeons*, (2021) 10.5435.

[52] K.R. Stone, W.G. Rodkey, R. Webber, L. McKinney, J.R. Steadman, Meniscal regeneration with copolymeric collagen scaffolds: In vitro and in vivo studies evaluated clinically, histologically, and biochemically, *The American journal of sports medicine* 20(2) (1992) 104-111.

- [53] J. De Groot, *Actifit, Polyurethane meniscus implant: basic science, The meniscus*, Springer (2010), pp. 383-387.
- [54] V. Condello, L. Dei Giudici, F. Perdisa, D.U. Screpis, M. Guerriero, G. Filardo, C. Zorzi, *Sports Traumatology, Arthroscopy, Polyurethane scaffold implants for partial meniscus lesions: delayed intervention leads to an inferior outcome, Knee Surgery, Sports Traumatology, Arthroscopy*, 29(1) (2021) 109-116.
- [55] G. Zur, E. Linder-Ganz, J.J. Elsner, J. Shani, O. Brenner, G. Agar, E.B. Hershman, S.P. Arnoczky, F. Guilak, A. Shterling, *Chondroprotective effects of a polycarbonate-urethane meniscal implant: histopathological results in a sheep model, Knee Surgery, Sports Traumatology, Arthroscopy, Knee Surgery, Sports Traumatology, Arthroscopy*, 19(2) (2011) 255-263.
- [56] A.C.T. Vrancken, P. Buma, T.G. van Tienen, *Synthetic meniscus replacement: a review, International orthopaedics* 37(2) (2013) 291-299.
- [57] S.A. Naghavi, *Bouncy Bioglass for Cartilage Replacement Application*, Department of materials, Imperial College London, (2018).
- [58] M. Gon, K. Tanaka, Y. Chujo, *Creative synthesis of organic–inorganic molecular hybrid materials, Bulletin of the Chemical Society of Japan* 90(5) (2017) 463-474.
- [59] G. Kickelbick, *Introduction to hybrid materials, Hybrid materials: Synthesis, characterization, and applications*, John Wiley & Sons, (2007) 1-46.
- [60] B.M. Novak, *Hybrid nanocomposite materials—between inorganic glasses and organic polymers, Advanced Materials* 5(6) (1993) 422-433.
- [61] S. Pandey, S.B. Mishra, *Sol–gel derived organic–inorganic hybrid materials: synthesis, characterizations and applications, Journal of sol-gel science and technology* 59(1) (2011) 73-94.
- [62] J.R. Jones, *Reprint of: Review of bioactive glass: From Hench to hybrids, Acta biomaterialia* 23 (2015) S53-S82.

- [63] E.M. Valliant, J.R. Jones, Softening bioactive glass for bone regeneration: sol–gel hybrid materials, *Soft Matter* 7(11) (2011) 5083-5095.
- [64] K. Tsuru, S. Hayakawa, A. Osaka, Synthesis of bioactive and porous organic-inorganic hybrids for biomedical applications, *Journal of sol-gel science and technology* 32(1-3) (2004) 201-205.
- [65] L. Ren, K. Tsuru, S. Hayakawa, A. Osaka, Novel approach to fabricate porous gelatin–siloxane hybrids for bone tissue engineering, *Biomaterials* 23(24) (2002) 4765-4773.
- [66] O. Mahony, O. Tsigkou, C. Ionescu, C. Minelli, L. Ling, R. Hanly, M.E. Smith, M.M. Stevens, J.R. Jones, Silica-gelatin hybrids with tailorable degradation and mechanical properties for tissue regeneration, *Advanced Functional Materials* 20(22) (2010) 3835-3845.
- [67] R. Ravarian, H. Wei, A. Rawal, J. Hook, W. Chrzanowski, F. Dehghani, Molecular interactions in coupled PMMA–bioglass hybrid networks, *Journal of Materials Chemistry B* 1(13) (2013) 1835-1845.
- [68] A. Rekondo, R. Martin, A.R. de Luzuriaga, G. Cabañero, H.J. Grande, I. Odriozola, Catalyst-free room-temperature self-healing elastomers based on aromatic disulfide metathesis, *Materials Horizons* 1(2) (2014) 237-240.
- [69] N. Ahmad, H. Sereshti, M. Mousazadeh, H.R. Nodeh, M.A. Kamboh, S. Mohamad, Physics, New magnetic silica-based hybrid organic-inorganic nanocomposite for the removal of lead (II) and nickel (II) ions from aqueous solutions, *Materials Chemistry and Physics* 226 (2019) 73-81.
- [70] F. Koç, N. Gizli, Synergistic Effect Of Ionic Liquid And Organo-Functional Silane On The Preparation Of Silica Based Hybrid Ionogels As Solid-State Electrolyte For Li-Ion Batteries, *Ceramics International*, (2021).
- [71] R. Suleiman, H. Dafalla, B. El Ali, Novel hybrid epoxy silicone materials as

efficient anticorrosive coatings for mild steel, Royal Society of Chemistry Advances 5(49) (2015) 39155-39167.

[72] M. Selvi, M. Vengatesan, S. Devaraju, M. Kumar, M. Alagar, In situ sol–gel synthesis of silica reinforced polybenzoxazine hybrid materials with low surface free energy, Royal Society of Chemistry Advances 4(17) (2014) 8446-8452.

[73] T.S. Hamidon, M. Hussin, Susceptibility of hybrid sol-gel (TEOS-APTES) doped with caffeine as potent corrosion protective coatings for mild steel in 3.5 wt.% NaCl, Progress in Organic Coatings 140 (2020) 105478.

[74] J. Chi, M. Chen, L. Deng, X. Lin, Z. Xie, A facile AuNPs@ aptamer-modified mercaptosiloxane-based hybrid affinity monolith with an unusually high coverage density of aptamer for on-column selective extraction of ochratoxin A, Analyst. 143(21) (2018) 5210-5217.

[75] U. Tiringer, I. Milošev, A. Durán, Y. Castro. Hybrid sol–gel coatings based on GPTMS/TEOS containing colloidal SiO₂ and cerium nitrate for increasing corrosion protection of aluminium alloy 7075-T6, Journal of Sol-Gel Science and Technology 85(3) (2018) 546-557.

[76] E. Bagheri, L. Ansari, K. Abnous, S.M. Taghdisi, F. Charbgo, M. Ramezani, M. Alibolandi, Silica based hybrid materials for drug delivery and bioimaging, Journal of Controlled Release, 277 (2018) 57-76.

[77] F. Tallia, 3-D printed flexible hybrids for tissue regeneration, Department of Materials, Imperial College London (2016).

[78] W. Fan, R.E. Youngman, X. Ren, D. Yu, and M.M. Smedskjaer, Structural control of self-healing silica–poly (tetrahydropyran)–poly (ε-caprolactone) hybrids, Journal of Materials Chemistry B, 9(21) (2021) 4400-4410.

[79] A. Fidalgo, L.M. Ilharco, The defect structure of sol–gel-derived silica/polytetrahydrofuran hybrid films by FTIR, Journal of Non-Crystalline Solids,

283(1-3) (2001) 144-154.

[80] A. Fidalgo, L. Ilharco, technology, Hybrid Silica Gel-Polytetrahydrofuran Thin Films, *Journal of sol-gel science and technology*, 13(1) (1998) 433-437.

[81] J. Beaman, D.L. Bourell, C. Seepersad, D. Kovar, Engineering, Additive manufacturing review: Early past to current practice, *Journal of Manufacturing Science and Engineering* 142(11) (2020) 110812.

[82] G. Miao, W. Du, M. Moghadasi, Z. Pei, C. Ma, Ceramic binder jetting additive manufacturing: Effects of granulation on properties of feedstock powder and printed and sintered parts, *Additive Manufacturing* 36 (2020) 101542.

[83] L. Yang, H. Miyanaji, Ceramic additive manufacturing: a review of current status and challenges, *Solid Freeform Fabrication Symposium*, 2017, pp. 652-679.

[84] S. Chang, L. Li, L. Lu, J.Y.H.J.M. Fuh, Selective laser sintering of porous silica enabled by carbon additive, *Materials* 10(11) (2017) 1313.

[85] A.H. Schoen, Infinite periodic minimal surfaces without self-intersections, *National Aeronautics and Space Administration* (1970).

[86] K. Große-Brauckmann, W.J.C.o.V. Meinhard, P.D. Equations, The gyroid is embedded and has constant mean curvature companions, *Calculus of Variations and Partial Differential Equations* 4(6) (1996) 499-523.

[87] L. Wu, W. Zhang, D.J.S. Zhang, Engineering gyroid-structured functional materials via templates discovered in nature and in the lab, *Small* 11(38) (2015) 5004-5022.

[88] X. Peng, Q. Huang, Y. Zhang, X. Zhang, T. Shen, H. Shu, Z.J.M. Jin, Design, Elastic response of anisotropic Gyroid cellular structures under compression: Parametric analysis, Parametric analysis." *Materials & Design* 205 (2021) 109706.

[89] F.T. Omigbodun, D.S. Engstrom, E.J.C. Mele, S.A. Physicochemical, E. Aspects, Improving Mechanical strength of bone-implant with primitive and gyroid lattice of

PLA/cHAP and rGO composites, *Colloids and Surfaces A: Physicochemical and Engineering Aspects* (2021) 127151.

[90] A.R. Torun, A.S. Dike, E.C. Yıldız, İ. Sağlam, N. Choupani, Fracture characterization and modeling of Gyroid filled 3D printed PLA structures, *Materials Testing* 63(5) (2021) 397-401.

[91] F. Caiazzo, V. Alfieri, B.D. Bujazha, Additive manufacturing of biomorphic scaffolds for bone tissue engineering, *The International Journal of Advanced Manufacturing Technology* 113(9) (2021) 2909-2923.

[92] N. Singh, P. Hameed, R. Ummethala, G. Manivasagam, K. G. Prashanth, J. Eckert, Selective laser manufacturing of Ti-based alloys and composites: Impact of process parameters, application trends, and future prospects, *Materials Today Advances* 8 (2020) 100097.

[93] S. Bose, D. Ke, H. Sahasrabudhe, A. Bandyopadhyay, Additive manufacturing of biomaterials, *Progress in materials science* 93 (2018) 45-111.

[94] O. Al-Ketan, R.K.A. Al-Rub, R. Rowshan, Mechanical properties of a new type of architected interpenetrating phase composite materials, *Advanced Materials Technologies* 2(2) (2017) 1600235.

[95] C. Yan, L. Hao, A. Hussein, P. Young, Ti-6Al-4V triply periodic minimal surface structures for bone implants fabricated via selective laser melting, *Journal of the mechanical behavior of biomedical materials* 51 (2015) 61-73.

[96] W. Prananingrum, Y. Naito, S. Galli, J. Bae, K. Sekine, K. Hamada, Y. Tomotake, A. Wennerberg, R. Jimbo, T. Ichikawa, Bone ingrowth of various porous titanium scaffolds produced by a moldless and space holder technique: an in vivo study in rabbits, *Biomedical Materials* 11(1) (2016) 015012.

[97] P. Hameed, C.-F. Liu, R. Ummethala, N. Singh, H.-H. Huang, G. Manivasagam, K. Prashanth, Biomorphic porous Ti6Al4V gyroid scaffolds for bone implant

applications fabricated by selective laser melting, *Progress in Additive Manufacturing* (2021) 1-15.

[98] H.A. Zaharin, A.M. Abdul Rani, F.I. Azam, T.L. Ginta, N. Sallih, A. Ahmad, N.A. Yunus, T. Zulkifli, Effect of unit cell type and pore size on porosity and mechanical behavior of additively manufactured Ti6Al4V scaffolds, *Materials* 11(12) (2018) 2402.

[99] A. Yáñez, A. Cuadrado, O. Martel, H. Afonso, D. Monopoli, Design, Gyroid porous titanium structures: a versatile solution to be used as scaffolds in bone defect reconstruction, *Materials & Design* 140 (2018) 21-29.

[100] A. Atae, Y. Li, C. Wen, A comparative study on the nanoindentation behavior, wear resistance and in vitro biocompatibility of SLM manufactured CP-Ti and EBM manufactured Ti64 gyroid scaffolds, *Acta biomaterialia* 97 (2019) 587-596.

[101] A. Atae, Y. Li, M. Brandt, C. Wen, Ultrahigh-strength titanium gyroid scaffolds manufactured by selective laser melting (SLM) for bone implant applications, *Acta Materialia* 158 (2018) 354-368.

[102] D. Barba, E. Alabort, R. Reed, Synthetic bone: design by additive manufacturing, *Acta biomaterialia* 97 (2019) 637-656.

[103] P. Naruphontjirakul, A.E. Porter, J. R. Jones, In vitro osteogenesis by intracellular uptake of strontium containing bioactive glass nanoparticles, *Acta biomaterialia* 66 (2018) 67-80.

[104] P. Naruphontjirakul, O. Tsigkou, S. Li, A.E. Porter, J.R. Jones, Human mesenchymal stem cells differentiate into an osteogenic lineage in presence of strontium containing bioactive glass nanoparticles, *Acta biomaterialia* 90 (2019) 373-392.

[105] F. Tallia, L. Russo, S. Li, A.L.H. Orrin, X. Shi, S. Chen, J.A.M. Steele, S. Meille, J. Chevalier, P. Lee, M.M. Stevens, L. Cipolla, J.R. Jones, Bouncing and 3D printable hybrids with self-healing properties, *Materials Horizons* 5(5) (2018) 849-860.

- [106] G. Young, Hybrid biomaterials with tuneable mechanical property gradients, Imperial College London (2019).
- [107] S.A. Naghavi, Bouncy Bioglass for Cartilage Replacement Application, Imperial College London (2018).
- [108] S. Berg, D. Kutra, T. Kroeger, C.N. Straehle, B.X. Kausler, C. Haubold, M. Schiegg, J. Ales, T. Beier, M. Rudy, Ilastik: interactive machine learning for (bio) image analysis, *Nature Methods* 16(12) (2019) 1226-1232.
- [109] J. Schindelin, I. Arganda-Carreras, E. Frise, V. Kaynig, M. Longair, T. Pietzsch, S. Preibisch, C. Rueden, S. Saalfeld, B. Schmid, Fiji: an open-source platform for biological-image analysis, *Nature methods* 9(7) (2012) 676-682.
- [110] J. Ollion, J. Cochenec, F. Loll, C. Escudé, T. Boudier, TANGO: a generic tool for high-throughput 3D image analysis for studying nuclear organization, *Bioinformatics* 29(14) (2013) 1840-1841.
- [111] G. Kickelbick, Hybrid materials: synthesis, characterization, and applications, John Wiley & Sons (2007).
- [112] B.M. Novak, Hybrid nanocomposite materials—between inorganic glasses and organic polymers, *Advanced Materials* 5(6) (1993) 422-433.
- [113] M. Gon, K. Tanaka, Y. Chujo, Creative synthesis of organic–inorganic molecular hybrid materials, *Bulletin of the Chemical Society of Japan* 90(5) (2017) 463-474.
- [114] S. Ahmad, F. Zafar, E. Sharmin, N. Garg, M. Kashif, Synthesis and characterization of corrosion protective polyurethanefattyamide/silica hybrid coating material, *Progress in Organic Coatings* 73(1) (2012) 112-117.
- [115] M. Pagliaro, R. Ciriminna, G.J.J.o.M.C. Palmisano, Silica-based hybrid coatings, *Journal of Materials Chemistry* 19(20) (2009) 3116-3126.
- [116] N.R. Mojarrad, B. Iskandarani, A. Taşdemir, A. Yürüm, S.A. Gürsel, B. Kaplan, Nanofiber based hybrid sulfonated silica/P (VDF-TrFE) membranes for PEM fuel cells,

International Journal of Hydrogen Energy 46(25) (2021) 13583-13593.

[117] H. Maleki, N. Huesing, Technology, Silica-silk fibroin hybrid (bio) aerogels: two-step versus one-step hybridization, Journal of Sol-Gel Science and Technology 98(2) (2021) 430-438.

[118] V.S. Gonçalves, P. Gurikov, J. Poejo, A.A. Matias, S. Heinrich, C.M. Duarte, I. Smirnova, Biopharmaceutics, Alginate-based hybrid aerogel microparticles for mucosal drug delivery, European Journal of Pharmaceutics and Biopharmaceutics 107 (2016) 160-170.

[119] L. Xu, H. Lee, Preparation, characterization and analytical application of a hybrid organic–inorganic silica-based monolith, Journal of Chromatography A 1195(1-2) (2008) 78-84.

[120] K.R. Phillips, T. Shirman, M. Aizenberg, G.T. England, N. Vogel, J. Aizenberg, Silica–titania hybrids for structurally robust inverse opals with controllable refractive index, Journal of Materials Chemistry C 8(1) (2020) 109-116.

[121] T.S. Hamidon, N.A. Ishak, M. Hussin, Technology, Enhanced corrosion inhibition of low carbon steel in aqueous sodium chloride employing sol–gel-based hybrid silanol coatings, Journal of Sol-Gel Science and Technology 97(3) (2021) 556-571.

[122] T.T. Thai, A.T. Trinh, M. Olivier, Hybrid sol–gel coatings doped with cerium nanocontainers for active corrosion protection of AA2024, Progress in Organic Coatings 138 (2020) 105428.

[123] D. Carboni, A. Pinna, L. Malfatti, P. Innocenzi, Smart tailoring of the surface chemistry in GPTMS hybrid organic–inorganic films, New Journal of Chemistry 38(4) (2014) 1635-1640.

[124] J. Babin, J. Iapichella, B. Lefèvre, C. Biolley, J.-P. Bellat, F. Fajula, A. Galarneau, MCM-41 silica monoliths with independent control of meso- and macroporosity, New Journal of Chemistry 31(11) (2007) 1907-1917.

- [125] A. Erigoni, U. Diaz, Porous Silica-Based Organic-Inorganic Hybrid Catalysts: A Review, *Catalysts* 11(1) (2021) 79.
- [126] O. Mahony, O. Tsigkou, C. Ionescu, C. Minelli, L. Ling, R. Hanly, M.E. Smith, M.M. Stevens, J.R. Jones, Silica-gelatin hybrids with tailorable degradation and mechanical properties for tissue regeneration, *Advanced Functional Materials* 20(22) (2010) 3835-3845.
- [127] K. Paulsen, D. Frasco, Determination of polymer molecular weight and composition using picoSpin NMR spectroscopy, *Analysis of artists' pigments by far-infrared microspectroscopy* (2016).
- [128] J.U. Izunobi, C. Higginbotham, Polymer molecular weight analysis by ^1H NMR spectroscopy, *Journal of Chemical Education* 88(8) (2011) 1098-1104.
- [129] M. Weldon, K. Queeney, A. Gurevich, B. Stefanov, Y. Chabal, K. Raghavachari, Si-H bending modes as a probe of local chemical structure: Thermal and chemical routes to decomposition of H_2O on Si (100)-(2 \times 1), *The Journal of Chemical Physics* 113(6) (2000) 2440-2446.
- [130] M. Kopani, M. Mikula, D. Kosnac, J. Gregus, E. Pincik, Morphology and FT IR spectra of porous silicon, *Journal of Electrical Engineering* 68(7) (2017) 53.
- [131] R. Zdero, *Experimental methods in orthopaedic biomechanics*, Academic Press (2016).
- [132] J.T. Evans, S. Mouchti, A.W. Blom, J.M. Wilkinson, M.R. Whitehouse, A. Beswick, A. Judge, Obesity and revision surgery, mortality, and patient-reported outcomes after primary knee replacement surgery in the National Joint Registry: A UK cohort study, *PLoS medicine* 18(7) (2021) e1003704.
- [133] N. Committee, National Joint Registry for England, Wales, Northern Ireland and the Isle of Man: 15th annual report, 2017, National Joint Registry Centre (2018).
- [134] S.M. Kurtz, K.L. Ong, E. Lau, K. Bozic, Impact of the economic downturn on

total joint replacement demand in the United States: updated projections to 2021, *Journal of Bone and Joint Surgery* 96(8) (2014) 624-630.

[135] H.M. Kremers, D.R. Larson, C.S. Crowson, W.K. Kremers, R.E. Washington, C.A. Steiner, W.A. Jiranek, D. Berry, J.S.A. volume, Prevalence of total hip and knee replacement in the United States, *The Journal of bone and joint surgery. American* volume 97(17) (2015) 1386.

[136] E. Losina, T.S. Thornhill, B.N. Rome, J. Wright, J. Katz, J.S.A. volume., The dramatic increase in total knee replacement utilization rates in the United States cannot be fully explained by growth in population size and the obesity epidemic, *The Journal of Bone and Joint Surgery. American* volume 94(3) (2012) 201.

[137] A.J. Price, A. Alvand, A. Troelsen, J.N. Katz, G. Hooper, A. Gray, A. Carr, D. Beard, Knee replacement, *The Lancet* 392(10158) (2018) 1672-1682.

[138] F.A. Alnaimat, D. Shepherd, K. Dearn, The effect of synthetic polymer lubricants on the friction between common arthroplasty bearing biomaterials for encapsulated spinal implants, *Tribology International* 98 (2016) 20-25.

[139] S. Yousef, A. Visco, G. Galtieri, D. Nocita, C. Espro, E. C, Wear behaviour of UHMWPE reinforced by carbon nanofiller and paraffin oil for joint replacement, *Materials Science and Engineering: C* 73 (2017) 234-244.

[140] S.D. Reinitz, B.H. Currier, R.A. Levine, D. Van Citters, Crosslink density, oxidation and chain scission in retrieved, highly cross-linked UHMWPE tibial bearings, *Biomaterials* 35(15) (2014) 4436-4440.

[141] K.K. Karupiah, A.L. Bruck, S. Sundararajan, J. Wang, Z. Lin, Z.-H. Xu, X. Li, Friction and wear behavior of ultra-high molecular weight polyethylene as a function of polymer crystallinity, *Acta Biomaterialia* 4(5) (2008) 1401-1410.

[142] K.D. Gemmell Jr, D. Meyer, Wear of Ultra High Molecular Weight Polyethylene against Synthetic Sapphire as Bearing Coating for Total Joint Replacements, *Research*

- & Development in Material Science 6 (2018) 560-567.
- [143] A. Maksimkin, D. Chukov, F. Senatov, A. Salimon, Comparative analysis of the tribological characteristics of canine joint cartilage and UHMWPE-based biomimetic materials, *Materials Letters* 191 (2017) 105-107.
- [144] S. Chan, C. Neu, K. Komvopoulos, A.H. Reddi, P.E. Di Cesare, Friction and wear of hemiarthroplasty biomaterials in reciprocating sliding contact with articular cartilage, *Journal of Tribology* (2011).
- [145] Q.J. Wang, Y.-W. Chung, *Encyclopedia of tribology*, Springer (2013).
- [146] A. Bistolfi, F. Giustra, F. Bosco, L. Sabatini, A. Aprato, P. Bracco, A. Bellare, Ultra-high molecular weight polyethylene (UHMWPE) for hip and knee arthroplasty: The present and the future, *Journal of Orthopaedics* (2021).
- [147] A. Ibrahim, G. Yamomo, R. Willing, S. Towfighian, structures, Parametric study of a triboelectric transducer in total knee replacement application, *Journal of intelligent material systems and structures* 32(1) (2021) 16-28.
- [148] V. Tapper, A. Toom, K. Pamilo, T. Niinimäki, J. Nieminen, S. Nurmi, T. Kortekangas, J. Paloneva, T. Surgery, Primary total knee replacement for tibial plateau fractures in older patients: a systematic review of 197 patients, *Archives of Orthopaedic and Trauma Surgery* (2021) 1-8.
- [149] H. Farhadifard, L. Rezaei-Soufi, M. Farhadian, P. Shokouhi, Effect of different surface treatments on shear bond strength of ceramic brackets to old composite, *Biomaterials Research* 24(1) (2020) 1-7.
- [150] F.N. Barrak, S. Li, A.M. Muntane, J.R. Jones, Particle release from implantoplasty of dental implants and impact on cells, *International Journal of Implant Dentistry* 6(1) (2020) 1-9.
- [151] E. Baird, G. Taylor, X-ray micro computed-tomography, *Current Biology* 27(8) (2017) R289-R291.

- [152] R. Pajor, A. Fleming, C. Osborne, S. Rolfe, C. Sturrock, S. Mooney, Seeing space: visualization and quantification of plant leaf structure using X-ray micro-computed tomography: View Point, *Journal of Experimental Botany* 64(2) (2013) 385-390.
- [153] G.E. Bean, D.B. Witkin, T.D. McLouth, D.N. Patel, R. Zaldivar, Effect of laser focus shift on surface quality and density of Inconel 718 parts produced via selective laser melting, *Additive Manufacturing* 22 (2018) 207-215.
- [154] P.S. Walker, S. Arno, C. Bell, G. Salvadore, I. Borukhov, C. Oh, Function of the medial meniscus in force transmission and stability, *Journal of biomechanics* 48(8) (2015) 1383-1388.
- [155] M.D. Joshi, J.K. Suh, T. Marui, S. Woo, Interspecies variation of compressive biomechanical properties of the meniscus, *Journal of biomedical materials research* 29(7) (1995) 823-828.
- [156] P. Bursac, S. Arnoczky, A. York, Dynamic compressive behavior of human meniscus correlates with its extra-cellular matrix composition, *Biorheology* 46(3) (2009) 227-237.
- [157] J. Sanchez-Adams, R.E. Wilusz, F. Guilak, Atomic force microscopy reveals regional variations in the micromechanical properties of the pericellular and extracellular matrices of the meniscus, *Journal of Orthopaedic Research* 31(8) (2013) 1218-1225.
- [158] A.M. Seitz, F. Galbusera, C. Kraus, A. Ignatius, L. Dürselen, Stress-relaxation response of human menisci under confined compression conditions, *Journal of the mechanical behavior of biomedical materials* 26 (2013) 68-80.
- [159] H. Pereira, S. Caridade, A. Frias, J. Silva-Correia, D. Pereira, I. Cengiz, J. Mano, J.M. Oliveira, J. Espregueira-Mendes, R. Reis, cartilage, Biomechanical and cellular segmental characterization of human meniscus: building the basis for Tissue Engineering therapies, *Osteoarthritis and cartilage* 22(9) (2014) 1271-1281.

- [160] G.J. Tuijthof, H.N. Meulman, J.L. Herder, C. Van Dijk, Biomechanics, Meniscal shear stress for punching, *Journal of Applied Biomaterials and Biomechanics* 7(2) (2009) 97-103.
- [161] M. Sweigart, C. Zhu, D. Burt, P. DeHoll, C. Agrawal, T. Clanton, K. Athanasiou, Intraspecies and interspecies comparison of the compressive properties of the medial meniscus, *Annals of biomedical engineering* 32(11) (2004) 1569-1579.
- [162] N. Hallab, A review of the biologic effects of spine implant debris: Fact from fiction, *SAS journal* 3(4) (2009) 143-160.
- [163] X. Dai, K. Zhang, C. Tang, Friction and wear of pivot jewel bearing in oil-bath lubrication for high rotational speed application, *Wear* 302(1-2) (2013) 1506-1513.
- [164] K. Arakaki, N. Kitamura, H. Fujiki, T. Kurokawa, M. Iwamoto, M. Ueno, F. Kanaya, Y. Osada, J.P. Gong, K. Yasuda, Artificial cartilage made from a novel double-network hydrogel: In vivo effects on the normal cartilage and ex vivo evaluation of the friction property, *Journal of Biomedical Materials Research Part A* 93(3) (2010) 1160-1168.
- [165] M. Caligaris, G. Ateshian, Cartilage, Effects of sustained interstitial fluid pressurization under migrating contact area, and boundary lubrication by synovial fluid, on cartilage friction, *Osteoarthritis and Cartilage* 16(10) (2008) 1220-1227.
- [166] C.T. Chen, M. Bhargava, P.M. Lin, P. Torzilli, Time, stress, and location dependent chondrocyte death and collagen damage in cyclically loaded articular cartilage, *Journal of Orthopaedic Research* 21(5) (2003) 888-898.
- [167] T. Shinonaga, M. Tsukamoto, T. Kawa, P. Chen, A. Nagai, T. Hanawa, Formation of periodic nanostructures using a femtosecond laser to control cell spreading on titanium, *Applied Physics B* 119(3) (2015) 493-496.
- [168] C.C. Homem, M. Peifer, Exploring the roles of diaphanous and enabled activity in shaping the balance between filopodia and lamellipodia, *Molecular biology of the*

cell 20(24) (2009) 5138-5155.

[169] R. You, X. Li, Y. Liu, G. Liu, S. Lu, M. Li, Response of filopodia and lamellipodia to surface topography on micropatterned silk fibroin films, *Journal of Biomedical Materials Research Part A* 102(12) (2014) 4206-4212.

[170] H. Xing, S. Komasa, Y. Taguchi, T. Sekino, J. Okazaki, Osteogenic Activity of Titanium Surfaces with Nanonetwork Structures, *International Journal of Nanomedicine* 16 (2021) 5037-5038.

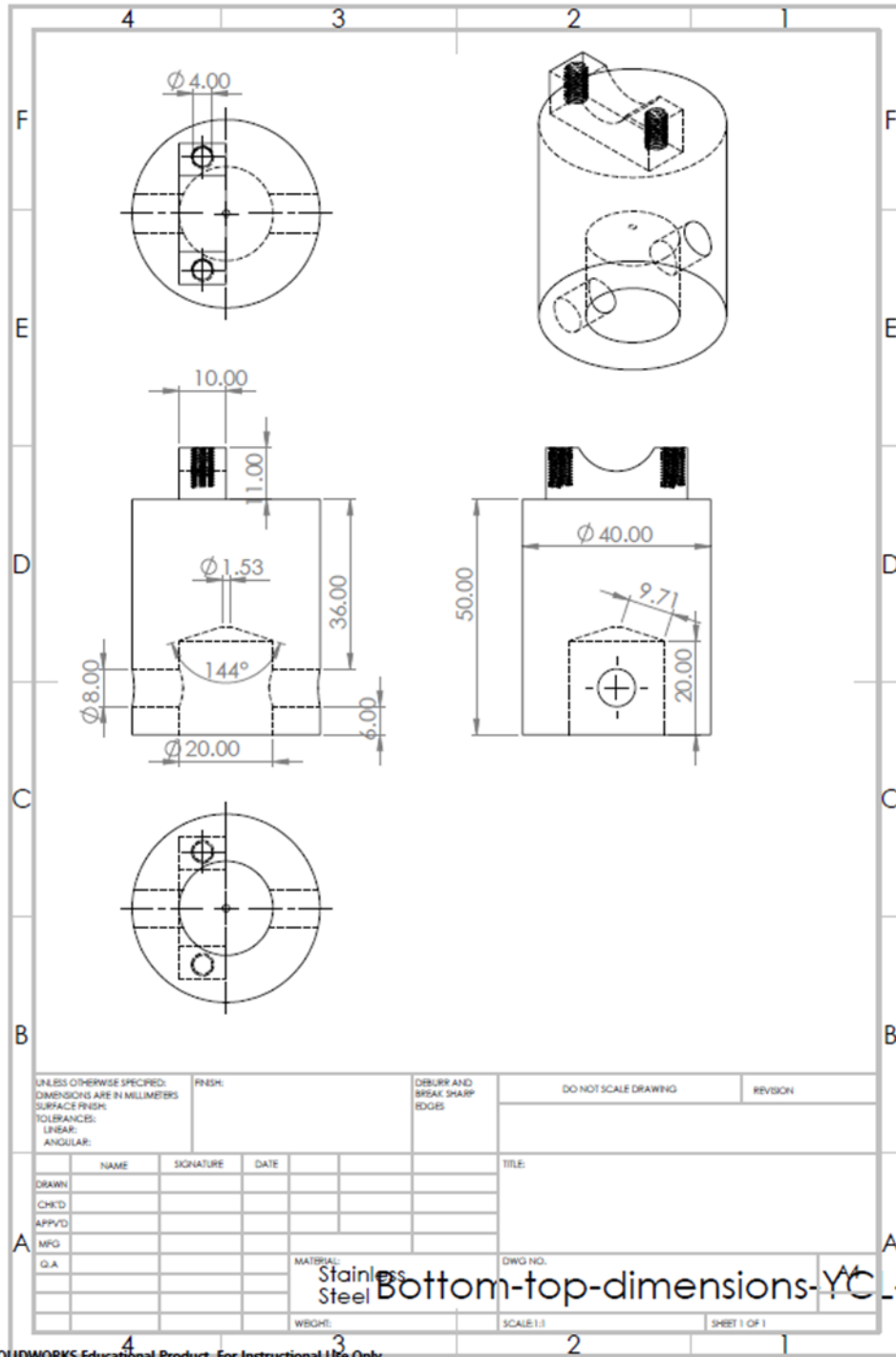
[171] H. Belabbas, M. Melizi, A. Benkhaled, N. Adili, Post hatch development of alkaline phosphatase activity in the broiler small intestine, *International Journal of Poultry Science* 14(4) (2015) 203.

[172] B. Yin, B. Xue, Z. Wu, J. Ma, K. Wang, A novel hybrid 3D-printed titanium scaffold for osteogenesis in a rabbit calvarial defect model, *American journal of translational research* 10(2) (2018) 474.

[173] S. Spriano, S. Ferraris, G. Pan, C. Cassinelli, E. Vernè, Biology, Multifunctional titanium: surface modification process and biological response, *Journal of Mechanics in Medicine and Biology* 15(02) (2015) 1540001.

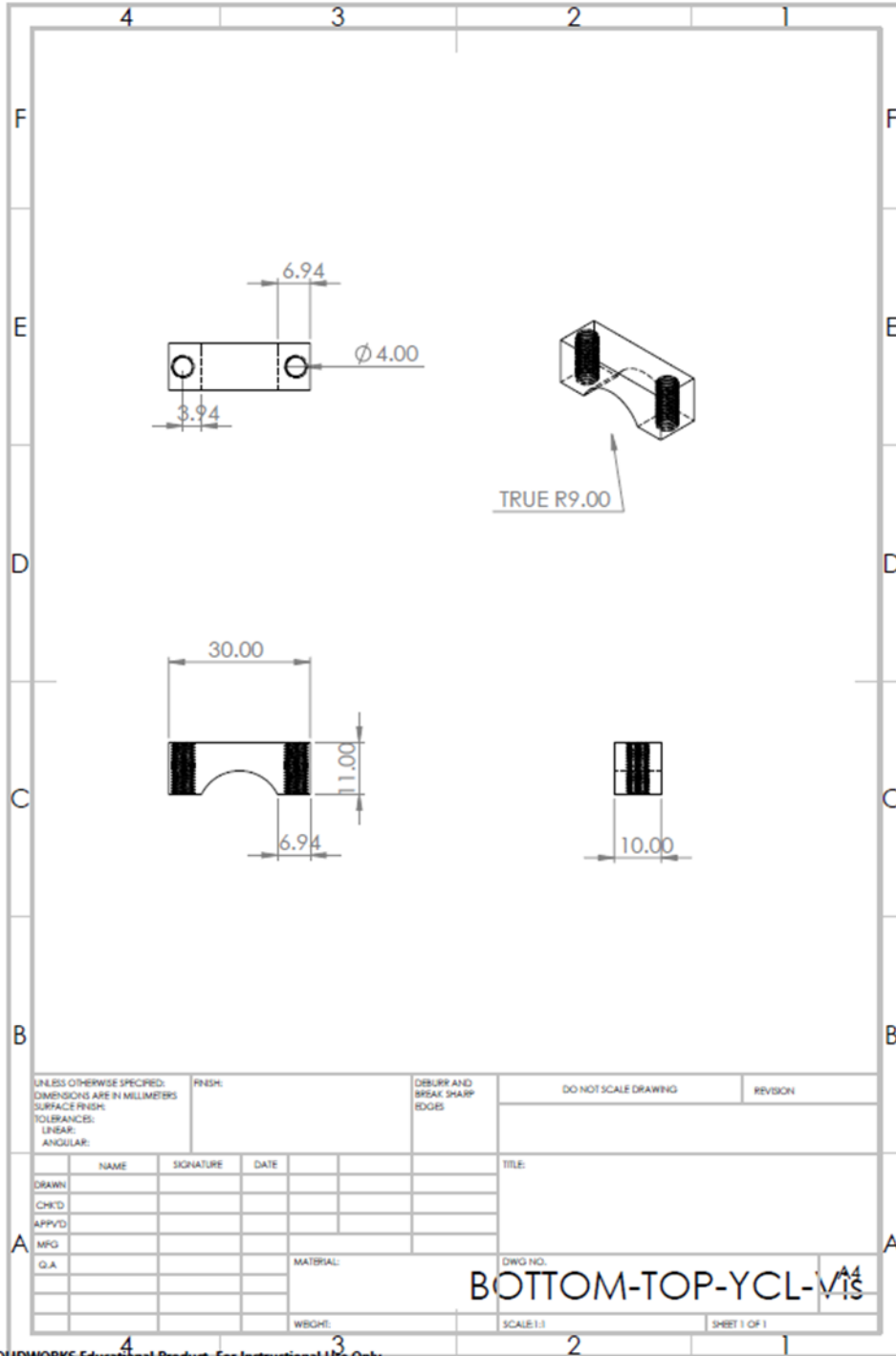
S1. Appendix

(a)



SOLIDWORKS Educational Product. For Instructional Use Only.

(b)



UNLESS OTHERWISE SPECIFIED: DIMENSIONS ARE IN MILLIMETERS				FINISH:		DEBURR AND BREAK SHARP EDGES		DO NOT SCALE DRAWING		REVISION	
SURFACE FINISH:				TOLERANCES:		LINEAR:		ANGULAR:		TITLE:	
DRAWN	NAME	SIGNATURE	DATE								
CHK'D											
APP'VD											
MFG											
Q.A											
				MATERIAL:				DRWG NO. 104		BOTTOM-TOP-YCL-VIS	
				WEIGHT:				SCALE: 1:1		SHEET 1 OF 1	

SOLIDWORKS Educational Product. For Instructional Use Only.

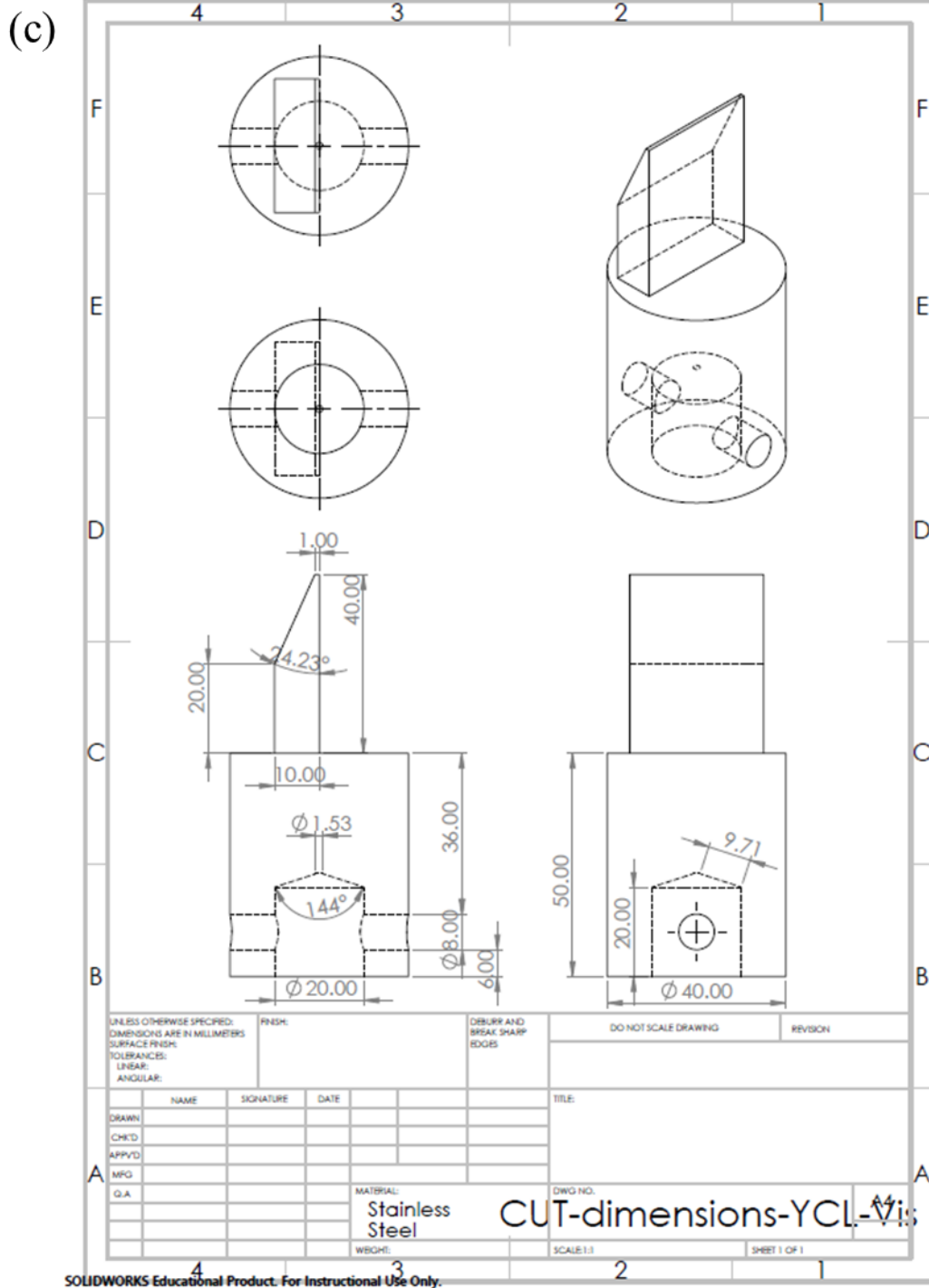


Figure S 1. Solidworks 2D drawing views of shear testing moulds (a) bottom component, (b) sample holder mechanism, and (c) top cutting component. (Unit is mm)

(b)

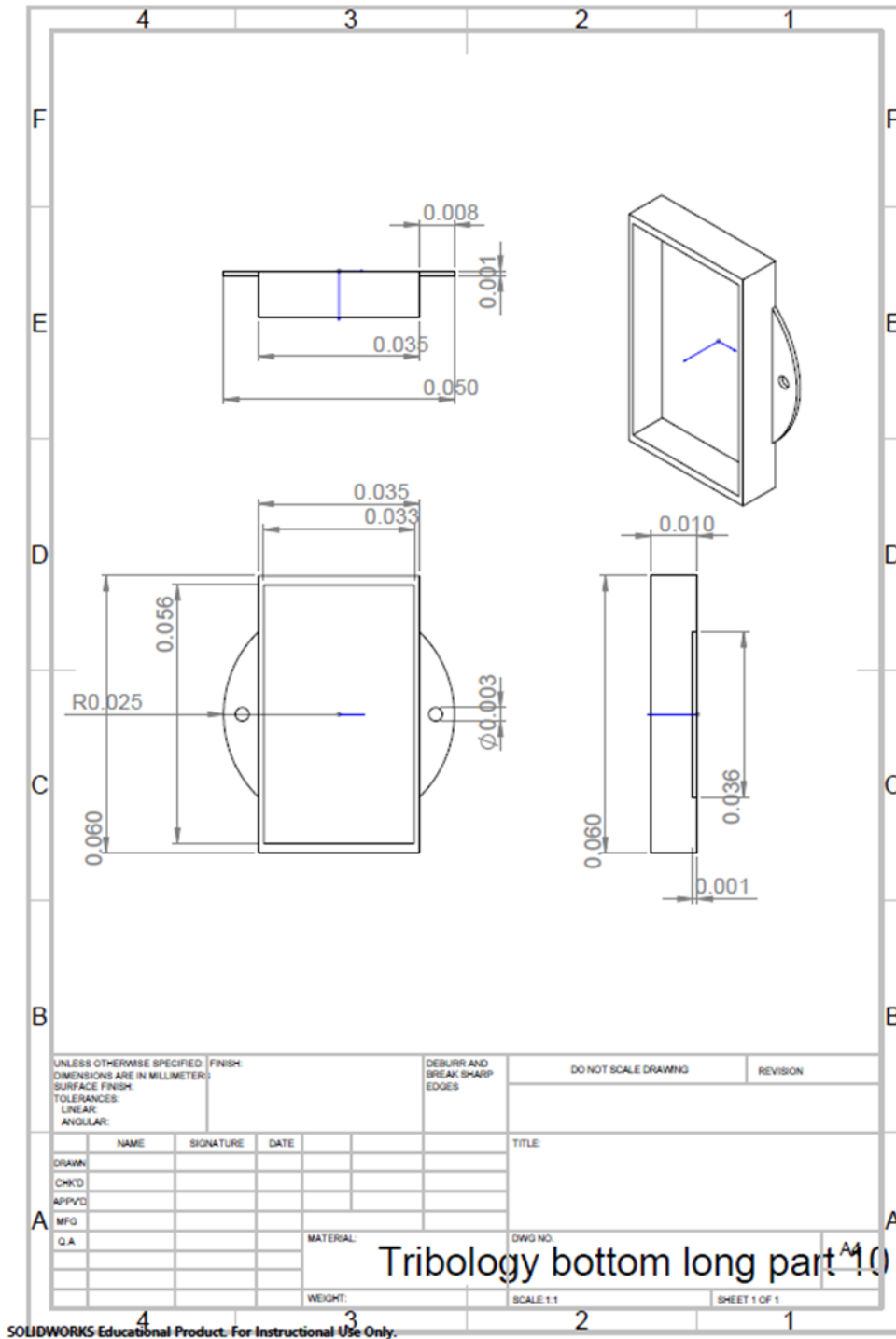


Figure S 2. Solidworks 2D drawing views of tribology testing rig design (a) top sample holder and (b) bottom cartilage holder. (Unit is mm)